manuscript accepted for publication in Geochemistry, Geophysics,Geosystems

Active tectonics, Quaternary stress regime evolution and seismotectonic faults in southern central Hispaniola: implications for the quantitative seismic hazard assessment

J. Escuder-Viruete [1], F.J. Fernández [2], F. Pérez Valera [3], F. McDermott [4]

[1]Instituto Geológico y Minero España - CSIC, C. La Calera 1, 28760 Tres Cantos, Madrid. Spain
[2]Departamento de Geología, Universidad de Oviedo. C. Jesús Arias de Velasco, 33005 Oviedo. Spain
[3]Departamento de Ciencias de la Tierra y del Medio Ambiente, Universidad de Alicante. 03080 Sant Vicent de Raspeig, Alicante. Spain
[4]School of Earth Sciences. University College Dublin, Belfield. Dublin 4. Ireland.

(*) Corresponding author: Javier Escuder-Viruete.

E-mail addresses: javier.escuder@csic.es (J. Escuder-Viruete), fjfernandez@uniovi.es (F.J. Fernández), fperez@ua.es (F. Pérez Valera), frank.mcdermott@ucd.ie (F. McDermott)

Key Points:

- Active faults in central southern Hispaniola are controlled by NE-directed shortening
- Quaternary stress regime evolution includes a compressional D1 followed by a strike-slip D2, locally coeval with an extensional D3
- Modeling establishes a very high seismic hazard zone centered in the Ocoa Bay

Abstract

Present-day convergence between Caribbean and North American plates is accommodated by subduction zones, major active thrusts and strike-slip faults, which are probably the source of the historical large earthquakes on Hispaniola. However, little is known of their geometric and kinematic characteristics, slip rates and seismic activity over time. This information is important to understand the active tectonics in Hispaniola, but it is also crucial to estimate the seismic hazard in the region.

Here we show that a relatively constant NE-directed shortening controlled the geometry and kinematics of main active faults in southern central Hispaniola, as well as the evolution of the Quaternary stress regime. This evolution included a pre-Early Pleistocene D1 event of NE-trending compression, which gave rise to the large-scale fold and thrust structure in the Cordillera Central, Peralta Belt, Sierra Martín García and San Juan-Azua basin. This was followed by a near pure strike-

slip D2 stress regime, partitioned into the N-S to NE-SW transverse Ocoa-Bonao-La Guácara and Beata Ridge fault zones, as well as subordinate structures in related sub-parallel deformation corridors. Shift to D2 strike-slip deformation was related to indentation of the Beata Ridge in southern Hispaniola from the Early to Middle Pleistocene and continues today. D2 was locally coeval by a more heterogeneous and geographically localized D3 extensional deformation. Defined seismotectonic fault zones divide the region into a set of simplified seismogenic zones as starting point for a seismic hazard modeling. Highest peak ground acceleration values computed in the Ocoa Bay establish a very high seismic hazard.

1. Introduction

The present-day convergence between the Caribbean and North American plates is partially accommodated within Hispaniola Island (Dominican Republic and Haiti). As consequence, this region contains a number of major active faults with lengths of up to several hundred kilometres that stand out as geomorphological and tectonic features (Mann et al., 1991a, 2002; Hernaiz Huerta & Pérez-Estaún, 2002; Calais et al., 2016) and have been the source of some of the larges earthquakes documented in the past 250 years (Calais et al., 2010; Prentice et al., 2010; Bakun et al., 2012; Mercier de Lépinay, 2011). For example, the strike-slip system of the Enriquillo-Plantain Garden Fault Zone (EPGFZ) produced the 12 January 2010 M_w 7.0 Leogâne and 14 August 2012 M_w 7.2 Nippes earthquakes, as well as probably other historical earthquakes in 1770 (estimated M_w 7.5; SISFRANCE Antilles, 2009) and 1860 (estimated M_w 6.3; Bakun et al. 2012).

The current tectonics in this densely populated and rapidly developing region are broadly understood (e.g., Mann et al., 1995, 2002; Hernaiz Huerta & Pérez-Estaún, 2002; Pérez-Estaún et al., 2007; Granja Bruña et al., 2014; Calais et al., 2016; Courbeau et al., 2016; Wang et al., 2018; Saint Fleur et al., 2019; Escuder-Viruete & Pérez, 2020), with subduction zones, major active thrusts and oblique strike-slip faults identified in several clearly defined zones. However, little is known of detailed

55 geometric and kinematic characteristics, Quaternary offsets and slip rates on these active fault
56 systems, and its seismic activity over time is poorly constrained by geochronological data. This
57 information is essential for understanding the present-day tectonics of Hispaniola, but it is also
58 crucial to establish an inventory of potential seismogenic sources, a seismotectonic zonation model,
59 and an estimate of the seismic hazard in the region.

60 The focus of this study is threefold: (1) to characterize the active deformation pattern and the main
61 seismotectonic faults in southern central Hispaniola, based on tectonic and geomorphologic field
62 observations, complemented with regional gravimetric, magnetic and seismic data analysis; (2) to
63 determine the Quaternary to present-day stress regime evolution by inversion of geologically
64 determined slip vectors on minor and major faults throughout the zone; and (3) to divide the region
65 into a set of simplified seismogenic zones as a starting point for a subsequent quantitative seismic
66 hazard modeling in terms of the peak ground acceleration (PGA).

67 **2. Geological setting**

68 *2.1. From intra-oceanic subduction to arc-continent collision and subduction polarity reversal in the*
69 *northern Caribbean plate*

70 Located on the northern edge of the Caribbean plate, the Hispaniola Island is a tectonic collage
71 produced by the SW-dipping Cretaceous subduction to Eocene oblique collision of the Caribbean
72 intra-oceanic arc with the southern continental margin of North America (Mann et al., 1991a; Draper
73 et al., 1994; Pérez-Estaún et al., 2007; Escuder-Viruete et al., 2011a, 2011b, 2013, 2016b). The main
74 consequence of the arc-continent collision were the blocking of the suture zone, the transfer of
75 deformation to the back-arc region in southern Hispaniola and subduction polarity reversal, with
76 renewed subduction beginning along a new NE-dipping subduction zone (e.g., Kroehler et al., 2011).

77 The geodynamic modeling software *GPlates* V2.3 (Müller et al., 2018; www.gplates.org), regional
78 bibliographic data, and observations presented in this paper allows the reconstruction of this relative

movement between the Caribbean and North American plates, distinguishing three main stages of evolution from the lower Campanian to the present-day. In the lower Campanian (80 Ma), the Lower Cretaceous Caribbean island-arc is moving to the northeast at a rate of about 4-5 cm/yr (Fig. 1a). By this time, the Caribbean arc had overridden the Galapagos hotspot, giving rise to a period of vigorous submarine oceanic plateau volcanism that began as early as 139 Ma and was widespread by 88 Ma, building the Caribbean Large Igneous Province (CLIP). In a SW-dipping subduction zone, the intra-oceanic arc consumed through subduction the large area occupied by the proto-Caribbean oceanic crust in the current central part of the Caribbean, and obliquely collided with the Maya block of the southeastern margin of the North American plate (Mann et al., 2007).

By the middle Eocene (40 Ma) the collision and suturing of the Caribbean island-arc against North America had halted the forward motion of the oceanic arc (Fig. 1b). Previous convergence and arc-continent collision caused the extinction of the arc volcanism, the emplacement of supra-subduction zone ophiolites and developed a zone of NE-directed foreland thrusting on the lower plate (Mann et al., 1991a; Pindell & Kennan, 2009; Pérez-Estaún et al., 2007; Escuder-Viruete et al., 2013, 2016b). Because the arc can no longer subduct the more continental crust of North America, convergence was accommodated by back-thrusting and the initiation of a new, NE-dipping subduction zone (Kroehler et al., 2011). In southern Hispaniola, the arc-continent collision in the middle to upper Eocene resulted in a reversal of subduction polarity in the back-arc region, as well as deformation by back-thrusting at the resulting Peralta-Muertos accretionary prism in the upper plate (Witschard & Dolan, 1990; Mann et al., 1991b; Dolan et al., 1991; Hernáiz-Huerta & Pérez-Estaún, 2002). The new subduction zone separated the Venezuela basin from the upper island-arc crust of central Hispaniola.

Since the lower Miocene, the ENE movement of the Caribbean plate gave rise to the oblique collision/accretion of the northern sector of the Caribbean oceanic plateau of transitional crust with the Peralta accretionary prism, resulting in the formation of the SW-directed Haitian-Neiba fold-and-

thrust belt and the San Juan-Azua basins in the foreland (Fig. 1c; Mercier de Lépinay, 1987; Witschard & Dolan, 1990; Dolan et al., 1991; Heubeck & Mann, 1991; Pubellier et al., 2000; Hernáiz-Huerta & Pérez-Estaún, 2002; Granja Bruña et al., 2014; Escuder-Viruete et al., 2023). During the Pliocene and until the present-day, convergence gave rise to the accretion of the central sector of the Caribbean oceanic plateau of thickened crust, causing in southern Hispaniola the uplift and folding of the Massif de la Serre-Sierra Bahoruco and the tectonic individualization of the Enriquillo-Cul de Sac basin. The blue star and line in the Fig. 1c represents the reconstructed location and path of a point of the Sierra Bahoruco as it travels with the Caribbean plate. *GPlates* reconstruction shows that the point started traveling to the NE at a rapid rate of 3-5 cm/yr and changed to a ENE direction in middle Eocene times (45 Ma) with a slow rate of 0.7-2.1 cm/yr. This change coincides with the arc-continent collision in northern Hispaniola and the start of subduction by back-thrusting in the Peralta-Muertos belts of southern Hispaniola.

2.2. Present-day geodynamic configuration of southern Hispaniola

Oblique collision has also led to the fragmentation of the northern Caribbean plate into several microplates, which are Septentrional (or North Hispaniola), Hispaniola-Puerto Rico and Gonâve (Fig. 2; Mann et al., 1995; Calais et al., 2016; Rodríguez-Zurrunero et al., 2019). Microplates are limited by major fault zones that, as reflected by the associated seismicity and modeled displacement rates, accommodate part of the relative movement between them (Mann et al., 2002; Manaker et al., 2008; Benford et al., 2012; Symithe et al., 2015; Calais et al., 2016; Corbeau et al., 2019).

In northern Hispaniola, the Septentrional microplate is a wedge-shaped tectonic forearc sliver, limited offshore to the north by the Northern Hispaniola Fault Zone (NHFZ, or western extension of the Puerto Rico Trench) and onshore to the south by the Septentrional Fault Zone (SFZ; Dolan et al., 1988; Mann et al., 2002; Escuder-Viruete & Pérez, 2020; Escuder-Viruete et al., 2020).

The Hispaniola-Puerto Rico microplate is an arc-crust block, limited to the north by the SFZ and to the south by the Muertos Trough (MT). To the west, the boundary between the Hispaniola block and Gonâve microplate is generally placed in the San Juan-Los Pozos fault zone (SJPFZ; e.g., Mann et al., 1991). From N to S (Fig. 2), the Hispaniola microplate includes the Cordillera Central domain and the Peralta-Muertos deformed belts. The Cordillera Central in the Dominican Republic and its prolongation in the Massif du Nord in Haiti is an Upper Jurassic-Upper Cretaceous basement composed mainly of Pacific-derived oceanic units, structurally limited to the northeast by the Hispaniola fault zone (HFZ) and to the southwest by the SJPFZ (Mann et al., 1991). It comprises fragments of oceanic lithosphere, plutono-volcanic complexes related to subduction, and basaltic units related to a mantle-plume magmatism (Escuder-Viruete et al., 2008). It also comprises the Quaternary intramountain basins of Cibao, Jarabacoa, Bonao, Constanza, Rancho Arriba and San José de Ocoa (Fig. 3).

The Peralta Belt (PB) is a NW-trending and SW-verging fold-and-thrust belt, structurally sandwiched between the San José-Restauración (SJRFZ) and the San Juan-Pozos fault zones (Mann et al., 1991b). The belt evolved from a back-arc basin for the Caribbean island-arc, with deposition of Campanian to Eocene turbidites (Trois Rivières and Las Palmas Formations), through a transpressive fold-and-thrust belt in the middle Eocene to early Miocene (Mercier de Lépinay, 1987; Witschard & Dolan, 1990; Dolan et al., 1991; Ramírez, 1995; Hernáiz-Huerta et al., 2007b). In the SE sector, the lithostratigraphic units of the Peralta Belt have been grouped into three thick sedimentary sequences, separated from each other by major unconformities: the Paleocene-Eocene Peralta Group; the middle Eocene-early Miocene Río Ocoa Group; and the middle Miocene-Pleistocene Ingenio Caei Group (Heubeck et al., 1991; Dolan et al., 1991; Díaz de Neira & Solé Pont, 2002; Hernaiz Huerta & Pérez-Estaún, 2002; Hernáiz-Huerta et al., 2007a; Pérez-Valera, 2010).

151 The Muertos Trough (MT) marks the boundary between the subducting floor of the Caribbean plate
152 and the overlying deformed belt south of eastern Hispaniola and Puerto Rico (Fig. 2). The thrust
153 focal mechanism of the June 24, 1984 earthquake (M_w 6.7) indicates subduction along the MT
154 (Byrne et al., 1985). Seismic reflection profiles across the MT image an N-dipping low-angle thrust
155 structure, with folded and faulted sedimentary rocks on top forming an accretionary prism (Driscoll
156 & Diebold, 1998; Dolan et al., 1998; Mauffret & Leroy, 1999; Granja Bruña et al., 2009, 2014).
157 Convergence across the Muertos Trough probably begins with the end of the arc-continent collision
158 and the onset of back-thrusting. *GPlates* reconstruction shows that the amount of oblique subduction
159 of the Caribbean plate beneath southern Hispaniola at the westernmost Muertos Trench has been
160 about 100 km (Fig. 1).

161 The Gonâve microplate is limited to the north by the Oriente Fault Zone and to the south by the
162 Enriquillo-Plantain Garden fault zone (EPGFZ). The nature of the crust of the Gonâve microplate is
163 not well established, having been proposed as a Cretaceous-Eocene remnant arc (Heubeck et al.,
164 1991), back-arc (Mann et al., 1991a) or the rifted crust of the eastern Cayman continental passive
165 margin (Corbeau et al., 2017, 2019). From the lower Miocene onwards, the oblique
166 collision/accretion processes have formed the Haitian-Neiba belt in the microplate. It consists of a
167 NW-trending and SW-verging fold-and-thrust belt, bounded to the north by the NE-dipping SJPFZ
168 (Mann et al., 1995; Ramírez, 1995; Pubellier et al., 2000; Hernáiz Huerta et al., 2007a). The thrust
169 bounding the NE Montagnes Noires-Sierra de Neiba thrust sheet was activated during the lower-
170 middle Miocene and the thrust bounding the SW Chaîne des Matheux-southern Sierra de Neiba
171 thrust sheet was developed from the middle-upper Miocene (Pubellier et al., 2000). Tilting and
172 faulting of Quaternary age deposits in the northern margin of the Enriquillo basin indicate that the
173 thrust belt is still active (Hernáiz Huerta et al. 2007), which is consistent with the seismic activity
174 recorded by Corbeau et al. (2019).

The Beata Ridge is a prominent NE-trending bathymetric high of about 450 km long built on the Caribbean plate (Fig. 2a; Mauffret & Leroy, 1999; Mauffret et al., 2001; Granja Bruña et al., 2014). It separates the Haiti basin to the west, from the Venezuelan basin to the east. The width of this structure in the zone of interaction with the Hispaniola-Puerto Rico microplate is about 120 km. The ridge comprises an unusually thick oceanic crust, essentially made up of mafic igneous rocks (gabbros, dolerites and basalts) of the Cretaceous CLIP (Sinton et al., 1998; Révillon et al., 2000; Dürkefälden et al., 2019). The Cretaceous basement of the Sierra Bahoruco and Hotte-Selle Massifs is made up of submarine volcanic rocks with similar petrological and geochemical characteristics, indicating that the Southern Peninsula of Hispaniola is an emerged fragment of the CLIP (Escuder-Viruete et al., 2016a).

Onshore/offshore seismic refraction and wide-angle reflection studies indicate a crustal thickness of 26 to 32 km in the Sierra Bahoruco, 20 to 22 km at the Beata Ridge, 10 to 15 km in the Venezuelan basin and only 5 to 10 km in the Haitian basin (Nuñez et al., 2016, 2019; Kumar et al., 2020). The crustal thickness of the Beata Ridge is controlled mainly by NNE to NE-striking faults, such as the Beata Ridge fault zone (BRFZ) that follows its axial trend (Mauffret et al., 2001). According to Granja Bruña et al. (2014), this fault acted in pre-Neogene times as a normal fault. The BRFZ continues to the NE, abruptly limiting the Sierra Bahoruco and Sierra Martín García to the southeast, until it intersects the SJPFZ in the western Ocoa Bay.

The NE-directed collision and impingement of the thickened crust of the Beata Ridge with the Hispaniola microplate in the Neogene gave rise to a recess of the Muertos accretionary prism and the clockwise rotation of fold and thrust structures of the Peralta Belt east of the Ocoa Bay (Mercier de Lépinay et al. 1988; Mann et al., 1991b; Ramírez, 1995; Hernaiz Huerta & Pérez-Estaún, 2002; Granja Bruña et al., 2014). Part of the present-day stress-field induced by the Beata Ridge collision is accommodated by the Ocoa-Bonao-La Guacara Fault Zone (OBFZ) within the Hispaniola microplate (Escuder-Viruete et al., 2023). This fault zone is an active, NNE to NE-striking large-scale fault

system that crosses the southern central sector of Hispaniola along more than 250 km (Pérez-Estaún et al., 2007). In the eastern Ocoa Bay, the OBFZ bends the fold and thrust structures of the Peralta Belt, the SJPFZ and the lower Miocene to Early Pleistocene sedimentary fill of the Azua basin (Fig. 2). This fault zone has recently been proposed as the onland transition between oceanic subduction and arc-oceanic plateau collision (Escuder-Viruete et al., 2023).

3. Methodology

3.1. Bathymetric, gravimetric and magnetic data sets

Maps shown in this study were created using several topographic and bathymetric data sets: (1) digital elevation models (DEMs) from the Shuttle Radar Topography Mission-30 Plus (https://www2.jpl.nasa.gov/srtm/) with a resolution of 30 m (Tozel et al., 2019); (2) DEMs obtained from ALOS Global Digital Surface Model with a resolution of 25 m (Takaku et al., 2020); (3) satellite images from *Google Earth Pro*® (http://earth.google.com) with a resolution from 1 km to 10 m; and (4) topographic and bathymetric profiles obtained from the GMRT data-set (available with *GeoMapApp*; www.geomapapp.org; Ryan et al., 2009).

The gravity data are from the compilation by the National Geospatial-Intelligence Agency (https://www.nga.mil). This compilation includes data from various campaigns conducted onland between 1939 and 1991 by IFREMER, Royal Astronomical Society, Cambridge University, Lamont-Doherty Geological Observatory and Woods Hole Oceanographic Institution. This compilation contains 3012 stations with a resolution of ±2 mGal and a density reduction of 2.67 g/cm^3.

The magnetic data come from the magnetic and radiometric flight carried out between 1995 and 1997 by the Compagnie Générale de Géophysique (CGG) in the onland territory of the Dominican Republic, with 500 m of separation of lines and a nominal height of 120 m, in the context of the SYSMIN Program of the EU of *Cartografía geotemática de la República Dominicana* (García

223 Lobón & Rey Moral, 2004). Data were gridded at 250 m and several procedures were followed to
224 ensure data quality, such as micro-levelling and filtering of frequencies greater than Nyquist.

225 *3.2. Regional analysis of potential field data*

226 In this work, lithological, structural, gravimetric and magnetic data were analyzed together to
227 constrain the crustal structure underlying southern central Hispaniola, to establish the distribution of
228 different crustal blocks with specific geophysical properties at the surface and to identify their
229 tectonic boundaries (even when they are hidden by a recent sedimentary cover). The analysis of the
230 potential field data was carried out with the *Geosoft Oasis Montaj*® software. Gravity data has been
231 gridded using a minimum curvature algorithm, resulting a grid cell size of 250 x 250 m.

232 Magnetic grids were calculated from raw data provided by CGG. Qualitative interpretation of the
233 magnetic data has been made using a reduction technique to the pole of the total magnetic field. This
234 reduction to the pole was calculated assuming a local inclination of 48° N and declination of 10° W.
235 This process removes the inclination effect of the total magnetic field by transforming the anomaly
236 into the vertical component of the field produced as if the source were at the North magnetic pole -
237 90° inclination. The inclination and declination used in the reduction to the pole were calculated
238 from the International Geomagnetic Reference Field subroutine in *Oasis Montaj*® based on the
239 latitude and longitude. Gravimetric and magnetic grids were interpreted on variations in amplitude,
240 wavelength character, lineament distribution, texture, and structural discontinuities. More details of
241 the methodology of acquisition and analysis of the potential field data are included in García-Lobón
242 & Rey-Moral (2004), García-Lobón & Ayala (2007) and Ayala et al., (2017).

243 *3.3. Seismicity*

244 Compilation of an earthquake catalog allowed us to determine the spatial and temporal distribution
245 of earthquakes, their relationships with the main active fault zones, and the characterization of the
246 seismotectonic structures in terms of their seismic parameters. For southern central Hispaniola, the

247 catalog was compiled by collecting and analyzing historical data (SISFRANCE-Antilles 2009; Bertil
248 et al., 2010; Flores et al. 2011; McCann et al. 2011; ten Brink et al. 2011; Bakun et al., 2012; and
249 references herein) and instrumental/experimental data (Russo & Villaseñor 1995; Alvarez et al.
250 1999; Tanner & Shepherd 1997; Terrier-Sedan & Bertil, 2021; ISC 2014; RSPR-Puerto Rico
251 catalogue, and USGC-NEIC catalogue). Access the local network, constituted by the *Instituto*
252 *Sismológico de la Universidad Autónoma de Santo Domingo* (ISU; uasd.edu.do), the *Observatorio*
253 *Sismológico Politécnico Loyola* (OSPL; ospl.ipl.edu.do) and the Projet Ayiti-Seismes performed by
254 Laboratoire Mixte International CARIBACT (ayiti.unice.fr/ayiti-seismes; BME, UEH/FDS/URGéo,
255 ENS and Géoazur partnership), enabled information on earthquakes in ghost areas of the global
256 seismic network to be obtained. Following Bertil et al. (2010, 2015), the catalogue was revised for
257 data quality, duplication, and foreshocks or aftershocks, and then homogenized the magnitudes using
258 the moment magnitude scale (*Mw*). The most contemporary sources describing the historical
259 earthquakes were investigated to establish the focal characteristics of each seismic event.

260 Due to the high uncertainty related to the magnitude and location of historical earthquakes, the
261 earthquakes in the catalogue were classified into three groups following Terrier-Sedan and Bertil
262 (2021): historical data before 1750 of unreliable magnitude and location; historical data between
263 1750 and 1960 of intermediate quality; and instrumental data after 1960 generally of high quality.
264 More than 12 epicentres of earthquakes of magnitude at least Mw 6.0 are located in the study area, or
265 the immediate surroundings, including the earthquakes of 1562 (destroyed La Vega and Santiago de
266 los Caballeros), 1615 (destroyed Santo Domingo), 1684 (affected Azua and Santo Domingo), 1691
267 (destroyed Azua, affected Santo Domingo), 1751 (destroyed Azua) and 1911 (affected San Juan).
268 The catalogue of earthquakes and focal mechanisms compiled for southern central Hispaniola is
269 included in the Supporting Information S1.

270 *3.4. U-Th geochronology*

Fossil coral reefs provide a snapshot of the ocean environment and sea level during their growth. As uranium is incorporated into the coral calcium carbonate skeleton during its growth, the U-Th geochronology method is appropriate for dating geological and oceanographic events in the Quaternary (e.g., Hibbert et al., 2016). To limit the effects of element mobility during diagenesis and/or any chemical alteration, coral samples were collected in apparently unaltered sectors on top of fossil wave-cut platforms and paleo-cliffs of the topographically lower terraces, as well as on the sides of small narrow gorges cut through the higher terraces. Fragments of corals that preserve the pristine growth structure were selected in the field. Subsequently, thin sections of these fragments were examined under the petrographic microscope to characterize the crystalline habit, the mineralogy as indicated by staining for carbonate minerals, and the degree of neomorphism. Coral fragments with an excellent preservation of the original skeleton and primary pore spaces void of cement and sediment were selected. Fragments were ground and the resulting powder analyzed by X-ray diffraction analysis at the IGME Laboratories in Madrid. Samples selected for U-Th dating yielded more than 95% aragonite during diffraction analysis. This test eliminated most samples of the topographically higher coral reef terraces.

U-series measurements were carried out using a high-resolution multi-collector inductively coupled plasma mass-spectrometer (ThermoFisher Neptune® multi-collector equipped with an Aridus® desolvation nebuliser) at the National Centre for Isotope Geochemistry, University College Dublin. Samples were spiked with a mixed ^{229}Th-^{233}U-^{236}U spike and were slowly dissolved in 7M HNO_3. Following overnight sample-spike equilibration, U and Th fractions were separated using anion ion-exchange columns using standard methods (Fankhauser et al., 2016). ^{238}U/^{236}U and ^{233}U/^{236}U isotope ratios were measured simultaneously using Faraday collectors, and the lower intensity of the ^{234}U ion beam was measured using a Faraday collector equipped with a low-noise $10^{\wedge 13}$ Ohm resistor. A mass-fractionation correction was applied to the measured uranium and thorium isotope ratios based on the certified near-unity ^{233}U/^{236}U ratio of the mixed spike (sufficient uranium carry over into the

296 thorium fraction permitted this for all thorium analyses). For thorium, $^{230}Th/^{232}Th$ and $^{230}Th/^{223}Th$
297 ratios were measured separately from the uranium runs, using the 10^{13} Ohm equipped Faraday
298 collector in the axial position for ^{223}Th. A detrital (inherited initial non-radiogenic ^{230}Th) correction
299 was applied to all U-Th analyses, assuming that the inherited component had a ($^{230}Th/^{232}Th$) ratio of
300 0.8 ± 0.4 (parentheses denote activity ratios). Whilst the choice of ($^{230}Th/^{232}Th$) for the detrital
301 component is somewhat arbitrary, the calculated ages for all are quite insensitive to this correction
302 (Supporting Information S2). All ages were calculated using the following decay constants ($\lambda^{234}U$ =
303 2.826E-6, $\lambda^{230}Th$ = 9.1577E-6, $\lambda^{238}U$ = 1.551E-10 and $\lambda^{232}Th$ = 4.9475-11; Jaffey et al., 1971;
304 Cheng et al., 2000). Laboratory blanks for ^{238}U and ^{232}Th were typically in the 1 to 10 pg range, and
305 no blank corrections were applied.

306 *3.5. Fault-slip data analysis*

307 Stress or strain can be evaluated using brittle fault-slip data inversion methods (Angelier, 1994). It
308 involves collecting faults data such as plane orientations, fault striae directions and sense of slip from
309 kinematic indicators at the outcrop scale. The methodology of fault-slip data inversion to determine
310 stress fields and to demonstrate temporal and spatial changes in the late Cenozoic stress states has
311 been used in many active tectonic areas around the world over the past three decades (Angelier,
312 1994; Twiss & Unruh, 1998; Célérier et al., 2012; and references therein). It consists of obtaining
313 from a population of fault-slip data the principal stress axes that best fit the reduced stress tensor at a
314 given measurement site. Inversion results include the orientation (azimuth and plunge) of the
315 principal stress axes ($\sigma_1 > \sigma_2 > \sigma_3$) of a reduced stress tensor as well as the stress ratio $R = (\sigma_2-\sigma_3/\sigma_1-$
316 $\sigma_3)$, a parameter describing relative stress magnitudes. The stress tensor provides information on the
317 stress regime, i.e., compressional (with σ_3 vertical), strike-slip (with σ_2 vertical), transpressional (σ_2
318 or σ_3 vertical and σ_2 close to σ_3 in magnitude), or extensional (with σ_1 vertical).

Several inversion methods have been proposed in the literature (see reviews by Célérier et al., 2012). Using multiple methods, hence different algorithms, increases the accuracy of the results by reducing the effect of systematic errors. In this study, the fault-slip data analysis and principal stress axes calculation were first performed with the kinematic right-dihedra method (RDM; Angelier, 1994), which shows the distribution of the percentage of compression or extension dihedra in stereographic projection. Next, fault-slip data were inverted with two independent methods: direct inversion (DIM) and numeric dynamic analysis (NDA). All inversion methods were performed with *TectonicsFP* v1.7.9 software of Reiter & Acs (2000) and Ortnet et al. (2002). Statistically stable stress tensors were obtained from 10 to 30 fault-slip data measured in each structural site, which have dimensions between 5 and 50 m in length and/or width. A further explanation of the fault-slip data acquisition and analysis is included in the Supporting Information S3.

The main goal of the fault-slip data analysis was to characterize the Quaternary to present-day stress regime evolution in southern central Hispaniola. Unfortunately, it is generally challenging to date the striations more precisely than by simply recording that they are younger than the rocks deformed by the faults. For this reason, we include results obtained from fault-slip data measured in igneous and sedimentary rocks of upper Cretaceous to Late Pleistocene age, which were constrained with geochronological data from faulted Middle to Late Pleistocene coral reef terraces and alluvial fan deposits.

On occasions, more than one set of striae are present on a fault plane at the same measurement site, which were formed by different stress tensors. For example, reverse dip-slip and oblique reverse striations caused by an NE-trending compression are crosscut by low-pitch angle striations resulting from a NE-trending σ_1 strike-slip stress regime. The discrimination of striae belonging to each fault set was conducted by numerical checking of compatibility with an inversion method and geological arguments. Fault crosscutting relationships, the overprinting of several striations in the same fault

343 plane and the absolute age of the faulted rocks have also been used as geological criteria to date
344 faults and thus discriminate paleostress tensors and tectonic events.

345 **4. Neotectonics of southern central Hispaniola**

346 *4.1. Large-scale structures*

347 The geology of southern central Hispaniola consists of five main elements: (1) an Upper Jurassic to
348 Upper Cretaceous igneous and metamorphic basement of the Cordillera Central domain; (2) a group
349 of latest Cretaceous-lower Eocene sedimentary rocks of the Peralta fold-and-thrust belt, that locally
350 unconformable overlie the basement; (3) an unconformable cover of folded and faulted middle
351 Eocene to lower Miocene sedimentary rocks of the Rio Ocoa Group; (4) a sequence of slightly
352 faulted and tilted Neogene sediments of the San Juan-Azua and Enriquillo basins; and (5) an
353 unconformable cover of Quaternary alluvial, fluvial and shallow marine deposits. The spatial
354 distribution of these elements is included in the geological map and cross-sections of Fig. 2.

355 The neotectonic structures of southern central Hispaniola are compiled in the map of the Fig. 3,
356 which results from integrating of new field data with the geologic map obtained by the SYSMIN
357 Project in the Dominican Republic (Pérez-Estaún et al., 2007). This map covers the eastern half of
358 the Cordillera Central, the Sierra Martín García, the southeastern part of the San Juan basin and the
359 whole Azua basin including the Baní pediment. This fieldwork area was selected because contains
360 the main active structures of the arc-plateau collision in the southern Dominican Republic.

361 The neotectonic structures of this area show three main trends: NW to WNW-striking folds and
362 thrusts; N to NE-striking right-lateral strike-slip faults; and ENE to E-striking left-lateral strike-slip
363 faults. Combined detailed structural analysis, fault-slip data inversion, and geochronology show that
364 these structures were generated during three main tectonic events (Table 1). The NW to WNW-
365 trending D1 structures are parallel to the structural grain of the Cordillera Central, as the folds and
366 thrusts of the Peralta belt. Located in the southern and eastern parts of the study area, the N-S to NE-

SW transverse D2 structures are the strike-slip fault segments of the Ocoa-Bonao-La Guácara and Beata Ridge fault zones, as well as second-order structural elements of the related sub-parallel deformation corridors. The ENE to E-striking faults are also transverse D2 structures concentrated in the northwestern sector of the studied area, which also deform the boundary with the Cibao basin. The previous structures appear locally cut by two families of D3 extensional faults, which have a different trend depending on their geographic location: WNW to W in the Ocoa Bay sector; and NE in the Cordillera Central sector.

The Ocoa-Bonao-La Guácara fault zone represents the structural transition between the Muertos oceanic accretionary prism and the Beata Ridge-Peralta Belt collision zone (Fig. 3; Escuder-Viruete et al., 2023). This fault runs along a N to NNE-striking band, 2 to 12 km wide and 120 km long, extending from the western termination of the Muertos Trough in the south to the Cibao basin in the north. Northward, the fault zone connects to the Hispaniola fault zone and changes its trend, curving from N-S to W-E over a distance of ~30 km. Based on discontinuities in its trace (such as step-overs, relays and bends), the fault zone comprises four major segments which are, from south to north (Fig. 3): Offshore (O-OBFZ), Southern (S-OBFZ), Central (C-OBFZ) and Western (W-OBFZ). These active segments are variably oblique with respect to the regional convergence direction and, therefore, they exhibit strike-slip, oblique reverse and thrust fault movements. Along the eastern margin of Ocoa Bay, the O-OBFZ segment produces offshore a clockwise rotation of the folded sediments of the Muertos accretionary prim, and bends and deforms onshore the fold and thrust structures of the Peralta Belt, the SJPFZ, the sedimentary fill of the Azua basin and the Late Pleistocene to Holocene alluvial fans (Escuder-Viruete et al., 2023).

The Beata Ridge fault zone (BRFZ) is part of the Beata Ridge. Mauffret & Leroy (1999) and Mauffret et al. (2001) suggested that the Beata Ridge fault zone (BRFZ) is a recent major NE-striking right-lateral strike-slip fault that limits the Beata Ridge to the west and would continue to the NE along the Beata Ridge summit and the eastern termination of the Sierra Bahoruco. On the basis

392 of swath bathymetry and offshore seismic reflection data (Granja Bruña et al., 2014), the northern
393 part of the BRFZ can be divided in two fault segments which are, from south to north (Fig. 3):
394 Central (C-BRFZ) and Northern (N-BRFZ). The N-BRFZ segment shows a constant NE-SW trend
395 along 55 km, parallel to the east coast of the Sierra Bahoruco and Martín García and extends onland
396 through the Azua Basin. The linearity of the fault segment indicates that it is a nearly vertical
397 structure that accommodates a predominantly strike-slip displacement. Field data obtained in onland
398 sub-parallel faults (see below) indicate a left-lateral strike-slip displacement characterizes the N-
399 BRFZ. This fault segment cuts the post-middle Miocene macrostructure of NW-trending folds in the
400 Sierra Bahoruco and Martín García, as well as the post-Early Pleistocene folds and thrusts that
401 deform the Arroyo Seco Formation in the Azua Basin. This segment connects at its northern end
402 with the OBFZ.

403 *4.2. Regional gravimetric data*

404 The regional pattern of the Bouguer anomaly reflects the main lithological and structural
405 characteristics of southern central Hispaniola (Fig. 4), even though the distribution of the stations of
406 gravity data is sparse and the used grid cell size is 250 x 250 m. Areas with positive anomalies
407 ranging from 40 to 134 mGal (yellow and orange tones) are present in the northern and eastern
408 sectors of the Cordillera Central, the northern sector of Sierra Bahoruco, Sierra Martín García and
409 the western Ocoa Bay, as well as the eastern Cordillera Septentrional. These anomalies have a
410 general NW-SE to WNW-ESE trend and are interpreted as areas of variably thickened island arc
411 crust of mafic to intermediate composition, with average densities around 2.95 g/cm^3 (Ayala et al.,
412 2007). Varying textures of the gravity field within these areas include smooth parallel lineaments
413 associated with bands of foliated amphibolites, elongated gabbro-dioritic batholiths and CLIP-related
414 basaltic units of the Upper Cretaceous basement. In contrast, long wavelength gravity anomalies
415 between -60 and 14 mGal (dark and light blue tones) characterize the Cibao basin, the southern
416 sector of the Cordillera Central (Peralta belt) and the San Juan-Azua basin. These areas comprise

417 silicilastic and carbonate rocks of the late Cenozoic sedimentary cover, with average densities around
418 2.55 g/cm^3 (Ayala et al., 2007). These negative anomalies present a smooth texture and are elongated
419 in the NW-SE to WNW-ESE direction, subparallel to the positive anomalies of the Cretaceous
420 basement.

421 Therefore, the regional gravity field defines an alternance of NW to WNW-striking long wavelength
422 anomalies, reflecting the contrast between the high-density Cretaceous igneous and metamorphic
423 basement of the northern Cordillera Central and the low-density Cenozoic sedimentary rocks of the
424 southern Cordillera Central, Cibao and San Juan-Azua basins (Fig. 4). The positive gravity anomaly
425 of the Cordillera Central is disturbed by intermediate anomalies between 20 and 50 mGal (light
426 green tones), along the the arcuate trace of the Ocoa-Bonao-La Guacara fault zone. This pattern
427 seems to reflect a NE-directed thick-skinned thrust structure in the basement, composed of tonalitic
428 batholiths and intermediate volcanic rocks of the Tireo Group, over the Cibao and Bonao
429 sedimentary basins.

430 The northern boundary of the Cibao Basin is linear and defined by a steep gradient in the gravity
431 field towards the positive anomaly of the eastern Cordillera Septentrional, coinciding with the
432 surface trace of the Septentrional fault zone. The southern limit of the Cibao basin with the
433 Cordillera Central is also marked by a strong gradient and coincide with the northern branch of the
434 Hispaniola fault zone. In turn, the southern boundary of the San Juan-Azua basin is marked by a
435 transition towards a NE-striking long wavelength positive gravity anomaly, which suggests the
436 existence of high-density basaltic rocks of the CLIP forming the basement of the Sierra Bahoruco,
437 the Sierra Martín García and the Ocoa Bay.

438 *4.3. Regional magnetic data*

439 The large-scale structure of southern central Hispaniola can be deduced by the orientation of the
440 regional magnetic field in NW to WNW-trending subparallel bands, which are often characterized by

441 a distinctive textural pattern (Ayala et al., 2017). In the reduced to the pole grid (Fig. 4a), short-
442 wavelength magnetic signatures generally correspond to areas where the magnetic sources in the
443 basement are located close to the surface. These areas are characterized by a pattern of NW to
444 WNW-trending sub-parallel anomalies, related to the late Cretaceous regional structure of
445 amphibolites, gabbro-tonalitic batholiths and ridges of basalts in the Cordillera Central. The strong
446 ferromagnetic character of the gabbros produces positive anomalies between 100 and 250 nT, which
447 delineate the intrusive contact of the Arroyo Caña, Jumunuco and El Río batholiths. In the eastern
448 Cordillera Central, the Hispaniola fault zone defines a strong NW-trending positive magnetic
449 anomaly between 150 and 270 nT, separating the Loma Caribe Peridotite outcrops and the mafic
450 volcanic rocks of the Los Ranchos Formation. This strong anomaly is related to the titanomagnetite
451 growth during serpentinization by tectonic exhumation and surficial alteration of the peridotites in
452 the late Cenozoic. A part of the southern Cordillera Central is characterized by scattered short-
453 wavelengths anomalies, roughly elongated along a NE-SW trend and related to the extrusion of
454 mafic to intermediate calc-alkaline to alkaline volcanic rocks during the Quaternary.

455 By contrast, long-wavelength magnetic signatures correspond to areas where the magnetic source is
456 located farther from the surface, or where the magnetic rock intensity in the basement is weak. In the
457 reduced to the pole grid (Fig. 4b), the Cibao and San Juan-Azua sedimentary basins generally display
458 long-wavelength negative magnetic anomalies between -10 and -350 nT. These negative anomalies
459 are related to the 1 to 5 km-thick overburden of paramagnetic sediments that fill these basins and
460 reduces the basement magnetic intensity. In turn, the pattern of NW-striking negative magnetic
461 anomalies that characterize the southern sector of the Cordillera Central is associated with the fold
462 and thrust structure of the Peralta belt sedimentary rocks. Nevertheless, the sedimentary carbonate
463 massifs of the Sierra Bahoruco, Sierra Martín García and coastal sectors of the Ocoa Bay shows
464 long-wavelengths of relatively high magnetic intensity between 0 and 100 nT, suggesting a magnetic
465 source that is shallower than the surrounding areas. A possible explanation for this high magnetic

intensity is that the basement in these areas comprises magnetite-rich basalts typical of the late Cretaceous CLIP.

In general, the main magnetic discontinuities in the reduced to the pole magnetic grid correlate well with the large-scale fault zones and the regional macrostructure of southern central Hispaniola (Fig. 4b). These discontinuities juxtapose areas of long and short-wavelength magnetic anomalies and define tectonic blocks bounded by the segments of the Septentrional, Hispaniola, Ocoa-Bonao-La Guácara and Beata Ridge fault zones (Fig. 4b). In detail, low magnetic values mark the surface trace of the main fault zones, suggesting that the deformed fault rocks are partially demagnetized. The reduced to the pole magnetic grid also shows the truncation and displacement of the NW to WNW-striking D1 structures in the Cordillera Central by the transverse D2 strike-slip fault system of the Ocoa-Bonao-La Guácara fault zone.

4.4. Late Neogene and Quaternary lithostratigraphy

In southern central Hispaniola, neotectonic activity is recorded by the sedimentary fill of the San Juan-Azua and Enriquillo basins, and by the growing of a system of coral reef terraces overlain by alluvial fans. The San Juan-Azua and Enriquillo basins have been defined as syn-tectonic flexural basins limited to the NE by SW-verging thrust systems, although the Enriquillo basin is also limited by opposite-vergence thrusts directed to the NE (Mann et al., 1991b, 1995; Hernáiz Huerta & Pérez-Estaún, 2002; Díaz de Neira, 2004; Hernaiz Huerta et al., 2007b). These basins form the southeastern extension of the Plateau Central and Cul-de-Sac basins in Haiti (Pubellier et al., 2000). The basins are filled by a ~4 km-thick upward shallowing and coarsening mega-sequence composed of Miocene to Early Pleistocene marine sediments (McLaughlin et al., 1991; Díaz de Neira & Solé Pont, 2002; Pérez-Valera, 2010).

The megasequence includes initial sedimentation on a regionally extensive open marine carbonate platform in the lower to middle Miocene (Sombrerito Formation). The deposition of turbiditic-type

clastic sediments in a deep marine environment occurred in the middle to upper Miocene (Trinchera Formation) and in a shallow-water platform in the lower Pliocene (Quita Coraza Formation). The regressive character of sedimentation gave rise in the Pliocene to shallow-marine clastic and coral reef deposits (Arroyo Blanco Formation) and, in the Enriquillo basin, the deposition of halite and gypsum evaporites (Angostura Formation), and fine-grained clastic sediments of a bay with excess salinity (Las Salinas Formation). The change to continental deposition took place in the late Pliocene-Early Pleistocene in the Azua basin, with the sedimentation of coarse-grained clastic sediments (Arroyo Seco Formation), and in the Early-Middle Pleistocene in the Enriquillo basin, with an upward change from reef limestones and supralittoral marls to alluvial-fan breccias and conglomerates (Jimaní Formation).

From the uppermost Pliocene, tectonic indentation of the southern margin of Hispaniola by northeastward displacement of the Beata Ridge (Heubeck & Mann, 1991; Mann et al., 1991b; Ramírez, 1995; Hernaiz Huerta & Pérez-Estaún, 2002), destroyed the foreland configuration developed in the southern margin, uplift and erosion of the Cordillera Central and emergence of the Azua and Enriquillo basins. After a sedimentary hiatus, uplift is recorded by the formation and progressive elevation of coral reef terraces in the southernmost coastal area during the Middle to Late Pleistocene. These coral terraces were probably organized in a staircase marine terrace system, which has only been partially preserved by later erosion and tectonics (see below).

Continued uplift and erosion were also accompanied by syn-tectonic sedimentation of coarse-grained alluvial fan systems directed towards Ocoa Bay (Díaz de Neira, 2000; Pérez-Valera, 2010). Recently, three alluvial fans systems developed at different topographic levels have been distinguished on the southern slope of the Cordillera Central during the Late Pleistocene to the Holocene (Fig. 3; Escuder-Viruete et al., 2023). The upper alluvial fan system forms small relict plateaus inclined towards the S and SE, over the surface of the intermediate alluvial fan system. The intermediate alluvial fan system forms a more extensive and better-preserved deposit, which connects the foot of the Cordillera

515 Central relief with the southern coast. The current lower alluvial fan system is spatially restricted to
516 the Sabana Buey valley and small coastal plains of southwestern Baní (Fig. 3). Its incision in the
517 intermediate alluvial fans implies a change in the geometry of the drainage network, which has been
518 attributed to fluvial capture processes (Díaz de Neira, 2000; Pérez-Valera, 2010), triggered by the
519 activity of the OBFZ (Escuder-Viruete et al., 2023).

520 **5. Fault-slip data inversion and late Cenozoic stress regimes**

521 This work calculated stress tensors from a population of 562 fault-slip data, measured in 32 sites
522 covering an area of approximately 100 × 50 km^2 in southern central Hispaniola. Geological
523 characteristics of these sites are reported in the Supporting Information S4. Stress inversion of the
524 fault-slip data yields 44 stress tensors and their respective plots are shown in the Figs. 5 to 14. The
525 orientation of their maximum horizontal stress, stress regime, kinematic type of faults and the
526 immersion method used in each site, which are generally consistent with each other, are included in
527 the Supporting Information S5.

528 *5.1. Fault-slip data inversion in the Peralta Belt*

529 Sites 21JE94, 21JE95 and 21JE96 are located along the highway between San José de Ocoa and
530 Nizao, within the Peralta Belt (Fig. 5). Both the mudstone-rich siliciclastic rocks of the lower Eocene
531 Peralta Group and the turbiditic sediments and conglomerates of the late Eocene Ocoa Group exhibit
532 1 to 100 m-thick zones of intense stratal disruption, which were interpreted by Witschard & Dolan
533 (1990) as thrust surfaces formed during the late Eocene in the Peralta accretionary prism. Disrupted
534 zones are mesoscopically characterized by boudinaged sandstone beds and pich-and-swell structures
535 defining lozenged blocks. Mudstone interbeds and argillaceous cataclastic bands have a WNW to
536 NW-striking pervasive scaly clay fabric (Sp) and occasionally contain tight to isoclinal folds with
537 rootless limbs (Fig. 5). The planar fabric (Sp) often contains a N to NE-trending calcite stretching
538 lineation (Lp) subparallel to the fold axes. In this Sp-Lp fabric, kinematic indicators such as the

asymmetry of the boudins or the S-C structures establish a general top-to-the W and SW shear sense. All these structures are typical of a block-in-matrix fabric of a mélange, essentially produced by syn-sedimentary deformation during the Late Eocene (see below). Stratally disrupted zones in the Ocoa Group rocks are cut by WNW-striking D1 thrust surfaces that typically dip 5° to 30° more deeply than the Sp fabric, when they are restored to the original horizontal position. Both the block-in-matrix fabric and the thrusts are cut by NNW to NE-striking strike-slip faults D2 and by high-dip angle normal faults D3 (Fig. 6).

The inversion of fault-slip data collected in several localidades throughout the Peralta Belt enables the separation of populations related to three distinct stress regimes (Fig. 6). The first population is represented by variably oblique reverse slip vectors in NW-striking and NE-dipping faults (sites 20JE09, 21JE94, 22JE12 in Yayas de Viajama, and 22JE13 in Tabera Arriba). It corresponds to a compressional stress regime D1 characterized by a NE-SW to ENE-WSW trending σ_1. The second population contains strike-slip to oblique reverse left-lateral slip vectors in NE-striking subvertical faults (sites 22JE13 and 21JE93). It is related to a near pure strike-slip stress regime D2 characterized by a NNE to NE-trending σ_1. The third population includes normal vectors along dip-slip and oblique normal striae in NE-striking high-angle faults (site 21JE96), and corresponds to an extensional stress regime D3 with a N136°E trending σ_3 (Fig. 13).

Sites 21JE123 and 21JE125 are located in the southernmost outcrops of the Peralta Belt, on the road Azua-Baní in the northern sector of the Ocoa Bay (Fig. 7). In this sector, the macrostructure in the Peralta Belt consists of a fold system of the lower to middle Eocene limestones of the Peralta Group and the upper Eocene turbidites with olistoliths of the Ocoa Group, related to a D1 deformation in a fold-and-thrust belt of NW-SE trend and SW-directed vergence. Towards the SE, the NW-trending D1 folds and thrusts of the Peralta Belt turn progressively towards a N-S trend and are cut and displaced by the O-OBFZ right-lateral D2 strike-slip fault. In the geological cross-section of Fig. 7, the Eocene rocks of the Peralta Belt overthrust through the SJPFZ the lower to middle Miocene

564 limestones of the Sobrerito Formation, and the assemblage overthrust in turn the conglomerates of
565 the upper Pliocene to Early Pleistocene Arroyo Seco Formation. Therefore, D1 thrusting continued
566 in this sector until the Early Pleistocene times.

567 Site 21JE123 is located along the Loma Vieja frontal thrust, which corresponds to the thrust ramp
568 associated with the NNW to NW-trending D1 Loma Vieja anticline (Fig. 7). The related D1
569 structures in the limestones of the Sobrerito Formation consist of SW-verging asymmetric folds,
570 associated with mid-dip angle faults inclined to the NE and SW, subparallel to the Loma Vieja thrust.
571 The mesoscopic S-C structures and other kinematic indicators imprinted on the fault planes establish
572 a top-to-the-SW reverse movement. Predominant dip-slip striae in reverse fault planes define a
573 population compatible with a thrust faulting stress regime and a N204°E trending compressional axis
574 (Fig. 7). On the other hand, the orientation of calcite veins and T-planes in clasts of the
575 conglomerates of the Arroyo Seco Fm establish a consistent NNE trend of D3 subhorizontal
576 extension.

577 Site 21JE125 is located at the northwest end of the Ocoa Bay, 3.5 km southeast of the town of Azua,
578 on the southern flank of a W-trending D1 anticline build-up in the limestones of the Sombrerito
579 Formation (Fig. 7). The anticline is affected by a system of high-dip angle (> 60°) strike-slip faults
580 D2 composed by NE-striking left-lateral strike-slip faults and antithetic N-striking right-lateral
581 strike-slip faults. The assemblage is truncated by E to WNW-trending D3 normal faults, exhibiting a
582 high-dip angle towards the N and S. Fault-slip measurements define two contrasting subsets (Fig. 7).
583 The first subset includes striations with a low-pitch angle in NE-striking strike-slip faults. Normal
584 and oblique normal dip-slip vectors in WNW-striking and NE and SW-dipping conjugate faults
585 represent the second subset. The first population corresponds to a purely strike-slip stress regime D2
586 with a N200°E trending σ_1 and the second population to an extensional stress regime D3
587 characterized by a N020°E trending σ_3.

588 *5.2. Fault-slip data inversion in the Ocoa Bay*

589 The limestone outcrops of the Sombrerito Fm located on the eastern coast of Loma Vigía, about 6
590 km southeast of Azua (Fig. 7) exhibit folds, reverse faults and thrusts related to D1 deformation. In
591 the 21JE112 site, these D1 structures consist of NW to WNW-trending and SW-verging asymmetric
592 folds, associated with low to mid-dip angle reverse faults inclined to the NE, subparallel to the
593 SJPFZ. The mesoscopic S-C structures and other kinematic indicators imprinted on these fault planes
594 establish a top-to-the-SW reverse movement. Striae on the fault planes define a reverse slip
595 consistent with a thrust faulting stress regime and a N222°E trending compressional axis (Fig. 8). In
596 the 21JE120 site, several WNW-striking and NE-verging asymmetric anticlines correspond to the
597 folds associated with a D1 back-thrust (Fig. 8). Slip measurements on the limbs of a decameter-scale
598 anticline define a population of WNW-striking and SW-dipping reverse faults. This population
599 corresponds to a purely compressional stress regime with a N026°E trending σ_1.

600 Throughout the Loma Vigia sector, D1 structures appear truncated by NW to W-trending D3 normal
601 faults, which exhibit mid to high-dip angles towards the NE and SW (Fig. 8). For instance, the SW
602 limb of a D1 anticline is cut by a D3 normal fault, causing the dragging of the limestone layers in the
603 hanging-wall block (site 21JE120), or the stratification appears displaced by a system of ENE to E-
604 striking normal faults with associated intrusion of mafic magmas (site 21JE113). In general, dip-slip
605 striae in these fault planes define normal faults populations compatible with extensional stress
606 regimes D3, characterized by a SSW to SW trending σ_3 (Fig. 8).

607 *5.3. Fault-slip data inversion in the eastern Sierra Martín García*

608 In the limestone outcrops of the Sombrerito Formation located on the southeast coast of the Sierra
609 Martín García, the D1 structures are strongly obliterated by the D2 deformation. This deformation
610 has given rise to fault zones with a general NE-SW direction and several kilometres in length,
611 parallel to the trace of the Beata Ridge fault zone, which runs offshore about 1.5 km to the SE. Fault

612 zones are marked by the development of bands of fault-gouge and fine crush breccia several tens of
613 meters thick (Fig. 9). Individual fault planes are very steep (dip > 70°) and have low-pitch angle (<
614 20°) striations that indicate a dominant strike-slip displacement.

615 At the Playa Caobita (site 21JE126), the Miocene limestones appear to be unconformably overlain
616 by a ~50 m-thick Quaternary sequence composed from bottom to top of (Fig. 9): reef limestones of a
617 basal fossil coral terrace; poorly consolidated conglomerates of an intermediate alluvial fan, that
618 includes reworked corals and cobbles at the base; and gravels and sands rich in limestone cobbles of
619 a younger alluvial fan. A gastropod *Strombus* sp. collected at the highest stratigraphic levels of the
620 coral terrace has provided a U-Th age of 118.47 ± 0.52 ka (21JE126C), so its growth took place in
621 the interglacial marine oxygen isotope stage (MIS) 5e, in the Middle to Late Pleistocene boundary.
622 Two specimens of coral *Diploria* sp. collected towards the basal and intermediate levels of the
623 terrace have provided U-Th ages of 476.99 ± 23.6 ka (21JE126B) and 331.92 ± 4.51 ka (21JE126A),
624 respectively. These ages indicate growth of the coral terrace during MIS 9c and 11 stages in the
625 Middle Pleistocene, although a reworking of the corals is not ruled out because the terrace
626 intercalates clastic levels.

627 Observations made in outcrops along the coast indicate that D2 strike-slip faults cut both reef terrace
628 limestones and intermediate alluvial fan conglomerates. These relationships establish a Late
629 Pleistocene age at least for the D2 deformation. On the other hand, the whole sequence of the coral
630 terrace and the overlying alluvial fans is tilted 10-18° towards the SE and appear deformed by a
631 system of E to ENE-striking D3 normal faults, which exhibits a high-dip angle (>60°) towards the N
632 and S (Fig. 9). Therefore, the D3 deformation has taken place in the Late Pleistocene to Holocene.
633 Fault-slip data measurements allow discrimination of a first population characterized by striations
634 with a low-pitch angle in subvertical fault planes and a second population of normal dip-slip vectors
635 in high-dipping faults. These populations represent two successive stress regimes: the first
636 corresponds to a near strike-slip stress regime D2 with a N020°E trending σ_1 (21JE127); and the

second matches with a near purely extensional regime D3 with a N008°E trending σ_3 (22JE15; Fig. 9).

5.4. Fault-slip data inversion in the northeast Sierra Bahoruco

The northwestern end of the Sierra Bahoruco shows a very sharp NE-SW trending coastline, subparallel to the trace of the central segment of the Beata Ridge fault zone, which runs offshore about 2.5 km to the SE (Fig. 3). Swath bathymetry and seismic reflection data suggest that fault segment constitutes the active boundary between the 1500 m elevated mountains of the Sierra Bahoruco to the NW and the -2500 m submerged slope of the Dominican sub-basin to the SE (Mauffret & Leroy, 1999; Granja Bruña et al., 2014).

Sites 21JE137 and 22JE26 are located in Playa Azul, about 6 km southeast of Barahona (Fig. 10). Along the coast, the limestone outcrops of the Sombrerito Formation define the northern limb of a D1 thrusting anticline of WNW trend and kilometric scale, which constitutes the internal structure of the Sierra Bahoruco in this sector. Limestones are strongly karstified and are unconformably overlain by a fossil coral reef 6 to 10 m-thick that defines a discontinuous morphological terrace along the coast. A *Diploria* sp. collected in the stratigraphically highest levels of the coral terrace has provided a U-Th age of 123.23 ± 0.70 ka (22JE26B), so its growth took place in the MIS 5e. The assemblage is also unconformably overlain by the poorly consolidated conglomerates and red clays of a >20 m-thick alluvial fan (Fig. 10).

Both the karstified limestones and the overlying coral terrace and clastic deposits are faulted and tilted by a system of N to NE-striking D2 strike-slip faults, subparallel to the trace of the Beata Ridge fault zone (see cross section in Fig. 10). Fault planes are generally very steep (dip > 65°) and the striae show left- and right-lateral conjugate motion with a low reverse component (pitch < 25°). Fault-slip data inversion reveals a strike-slip D2 stress-field with a N046°E trending σ_1 stress axis (Fig. 10). Therefore, the central Beata Ridge fault segment has been active for at least the Late

661 Pleistocene. In turn, the internal structure in the alluvial fan deposit defines a system of open
662 anticlines and synclines of WNW-ESE trend and decametric to hectometric wavelength, which
663 appears faulted on the flanks by WNW to W-trending D3 normal faults. These folds are interpreted
664 as roll-over structures related to the D3 extensional faulting. Striations measured in decametric-scale
665 fault planes and T-planes open in clasts are compatible with an extensional D3 regime, characterized
666 by a N010°E trending σ_3 (Fig. 10).

667 *5.5. Fault-slip data inversion in the southwestern Sierra Martín García*

668 In the southwestern sector of the Sierra Martín García, the limestones of the Miocene Sombrerito
669 Formation overthrust the sandstones, marls and gypsum of the upper Pliocene La Salina Formation,
670 and the ensemble regionally overthrusts the continental conglomerates and mundstones of the upper
671 Pliocene to Early Pleistocene Arroyo Seco Formation. These WNW-trending structures constitute the
672 SW-directed D1 frontal thrust, which juxtaposes the anticline macrostructure of the Sierra Martín
673 García to the poorly consolidated alluvial, floodplain and deltaic Quaternary deposits of the
674 Enriquillo basin (Fig. 3).

675 Site 21JE130 is located in the hanging-wall block, about 300 m northward of the frontal thrust,
676 where the gypsum and marl beds of the La Salina Formation exhibit structures related to D1
677 deformation (Fig. 11). These structures consist of WNW-trending and SW-verging asymmetric folds,
678 associated with mid-dip angle reverse faults inclined to the NE, subparallel to the basal thrust. The
679 asymmetry of D1 folds and mesoscopic S-C structures establish a top-to-the-SW reverse movement.
680 Oblique reverse striae measured in the reverse fault planes define a fault population compatible with
681 a D1 thrust faulting stress regime and a N047°E trending compressional axis (Fig. 11). In the site
682 21JE129, the D1 frontal thrust is locally fossilized by a coral reef terrace, where a *Strombus* sp.
683 collected near its stratigraphic base has provided a U-Th age of 124.65 ± 0.85 ka. A *Diploria* sp also

684 collected in the same basal levels has given a similar U-Th age of 128.89 ka (Fig. 11), thus the coral
685 terrace grew in the MIS 5e stage.

686 Both the D1 thrust-related folds and the coral terrace are affected by a system of high-dip (> 60°)
687 strike-slip faults D2. This fault system comprises NE to ENE-striking left-lateral strike-slip faults
688 filled by subvertical calcite veins and antithetical N to NNE-striking right-lateral strike-slip faults,
689 establishing a strike-slip stress D2 regime characterized by a NE-trending σ_1 axis (Fig. 11).
690 Therefore, the thrust-related D1 deformation reaches the Middle Pleistocene and the strike-slip-
691 related D2 deformation continues after the Middle to Late Pleistocene boundary. Finally, a set of E to
692 ENE-trending and high-dip angle D3 normal faults locally truncate the assemblage. Normal dip-slip
693 striae measured in these fault planes cutting the gypsum beds are compatible to an extensional
694 regime with a N355°E trending σ_3 axis (Fig. 11).

695 *5.6. Fault-slip data inversion in the San José de Ocoa basin*

696 The southern segment of the Ocoa-Bonao-La Guácara fault zone is a roughly 50 km-long, N-striking
697 right-lateral strike-slip fault system, that cuts at a high-angle and clockwise rotate the NW-SE
698 trending folds and thrusts of the Peralta Belt and the structure of the late Cretaceous basement of the
699 Cordillera Central (Figs. 3, 5). The segment is geometrically characterized by separating the fault
700 trace into two branches south of San José de Ocoa town, giving rise to a right-hand releasing-bend
701 and the San José de Ocoa pull-apart sedimentary basin (Escuder-Viruete et al., 2023). Both branches
702 rejoin about 35 km northward into the C-OBFZ segment in the Bonao basin.

703 Site 21JE102 is located near the eastern branch of the S-OBFZ segment, in the town of Naranjal, 2.5
704 km east of San José de Ocoa (Fig. 5). At outcrop scale, N to NNE-striking right-lateral D2 strike-slip
705 faults cut D1 thrust surfaces inclined to the NE, defined by sheared bands of mudstones in the upper
706 Eocene Ocoa Formation, characterized by a SW-directed penetrative S-C fabric. Fault-slip
707 measurements define two contrasting subsets (Fig. 12): the first subset is reverse to oblique reverse

and is associated to striations with a high-pitch angle in NW-striking fault planes; the second subset has oblique reverse and strike-slip vectors in conjugate right- and left-lateral faults. The first population corresponds to a compressional stress regime D1 with a N243°E trending σ_1 and the second population establishes a purely strike-slip stress regime D2 characterized by a N047°E trending σ_1.

Site 21JE100 is also located along the eastern strand of the S-OBFZ segment, 2 km north of San José de Ocoa, on the road to Constanza (Fig. 5). The fault segment tectonically juxtaposes the folded and faulted volcanic rocks of the Tireo Group and the gravels and sands of the Quaternary fill of the San José de Ocoa basin. Volcanic rocks have developed hectometer-scale subvertical fault planes sub-parallel to the S-OBFZ, characterized by a 5 m-wide brecciated damage zone and striations with a low-pitch angle (Fig. 12). These striae define a vector population compatible with a D2 strike-slip stress regime and a N226°E trending compressional axis. South of San José de Ocoa town, the eastern strand juxtaposes the folded and faulted mudstones of the Numero Fm and the gravels and sands of the basin through a subvertical D2 fault system that also tilts westward the Quaternary deposits. Striations measured in NNW-striking oblique reverse right-lateral faults of the 20JE15 site are compatible with a D2 strike-slip regime and a N186°E σ_1 axis (Fig. 12)

The D2 strike-slip deformation is also very penetrative along the western branch of the S-OBFZ segment, which is morphologically marked by an east facing 200 m-high scarp. This strand juxtaposes the folded and faulted rocks of the Peralta Belt to the W with poorly consolidated gravels and sands that fill the San José de Ocoa basin to the E (Fig. 5). In several sites (20JE14, 21JE97, 21JE98 and 21JE99), striations measured on metric to decametric-scale faults subparallel to the S-OBFZ segment define a population of pure strike-slip to oblique reverse slip vectors, compatible with a D2 strike-slip regime and a predominant NE trending σ_1 stress axis (Fig. 12). The subvertical

731 orientation of calcite veins and T-planes in clasts of the Quaternary conglomerates consistently
732 establishes a WNW to NW trend of subhorizontal extension.

733 However, the effects of D3 extensional deformation are limited in this sector and geographically
734 localized to the right-hand releasing-bend that forms the San José de Ocoa basin. Site 21JE99 is
735 located between the two branches of the S-OBFZ segment, where the mafic to intermediate tuffs of
736 the Tireo Group are in tectonic contact with the well-bedded limestones of Maastrichtian age. Slip
737 measurements show two different populations: oblique reverse righ-lateral and dip-slip reverse
738 vectors (Fig. 12); and oblique normal vectors (Fig. 13). The overlap relationships between striaes
739 establish that these two populations represent two successive stress fields: the first corresponds to a
740 transpressional D2 stress regime with a N270°E trending σ_1; and the second corresponds to a more
741 purely extensional D3 regime characterized by a N121°E trending σ_3. Also related to local D3
742 extensional tectonics, NW to N-striking normal faults have also been observed at sites 21JE103 and
743 21JE108 (Fig. 5). Dip-slip striations measured on these fault planes establish an extensional D3
744 regime characterized by a W-trending σ_3 (Fig. 13).

745 *5.7. Fault-slip data inversion in the Cordillera Central*

746 The Cordillera Central is characterized by the development of crustal shortening structures,
747 topographic uplift and exposure of the late Cretaceous volcano-plutonic basement in the core of
748 large-scale WNW to NW-trending D1 anticlines (Fig. 3). In the Constanza-Sabana Quéliz area, the
749 macrostructure consists of D1 folds and thrusts of WNW-ESE trend and usually SW-directed
750 vergence, built up in a sequence composed by Cenomanian limestones and siliceous-rich sediments,
751 Turonian to early Campanian mafic tuffs of the Constanza Formation, late Campanian mudstones of
752 the El Convento Formation and Maastrichtian shallow-water platform limestones, as well as plutonic
753 rocks (Escuder-Viruete et al., 2008). This macrostructure is locally cut and displaced by a system of
754 high-dip angle strike-slip D2 faults, which includes NW to NNE-striking right-lateral strike-slip

faults and conjugate NE to ESE-striking left-lateral strike-slip faults. NE to E-trending D3 normal faults locally truncated the assemblage exhibiting a high-dip angle towards the NW and SE.

This deformative sequence is well recorded at the 21JE80 site, located ~10 km east of the Constanza town in the Tireo river valley (Fig. 5). Fault-slip data measurements and cross-cutting relationships show three contrasting subpopulations (Fig. 14): reverse and oblique reverse left-lateral faults; subvertical faults with low-pitch angle striations; and normal and oblique normal right-lateral faults. These subsets represent three successive stress regimes: the first corresponds to a compressional stress regime D1 characterized by a N213°E trending σ_1; the second adjusts to a near strike-slip stress regime D2 with a N321°E trending σ_1; and the third matches with a purely extensional regime D3 with a N183°E trending σ_3 (Fig. 14).

Field observations at various points in the Cordillera Central show that D3 extensional faults overlap D1 thrusts. For example, the various kinematic types of faults that deform green mafic tuffs at sites 21JE78 and 21JE79, where the fault-slip data inversion enables the separation of populations related to two distinct stress regimes (Figs. 13, 14). The first population is represented by dip-slip to variably oblique reverse slip vectors in low to mid-dip faults; the second population includes normal slip vectors along dip-slip striae in predominantly NNE to NE-striking high-dip faults. Both fault types define a NE-SW to W-E compressional D1 regime and a NW-SE extensional D3 regime, respectively.

A similar deformative sequence is recognized in the southeastern Cordillera Central, located east of the S-OBFZ segment (Fig. 3). In this sector, the S-OBFZ exhibits a fresh N-S scarp and represents the boundary between the >2000 m elevated mountains of the Cordillera Central to the W and the 650 m elevated Rancho Arriba valley to the E. Along this morphological step, the fault zone produces triangular facets, perched valleys, and dextral offsets of streams that testify its recent activity. Deformation related to this segment produced the local clockwise rotation of the D1 fold

779 and thrust structure and the formation of the Rancho Arriba intramountain basin, which is filled by
780 the Quaternary alluvial fans fed by the erosion of the surrounding relief.

781 Site 21JE70 is located at the Rancho Arriba basin southern bound. The basin exhibits an ENE-WSW
782 elongated rectangular shape controlled by a southern active master fault (Fig. 5). Fault-slip
783 measurements on hornblende-bearing tonalities of the Arroyo Caña batholith define two contrasting
784 subsets (Figs. 13, 14): oblique reverse to strike-slip vectors in NE to ENE-striking faults; and oblique
785 normal slip vectors in conjugate ENE and WSW-striking high-angle faults. The first set corresponds
786 to a strike-slip stress regime D2 with a N022°E trending σ_1 and the second set establishes a near pure
787 extensional stress regime D3 characterized by a N023°E trending σ_3, related to the formation of the
788 basin. Observations carried out in the volcanic rocks of the Tireo Group at sites 21JE72 and 21JE73
789 allow us to establish similar temporal relationships: younger NE to E-striking D3 normal faults cut
790 older D2 strike-slip and D1 reverse faults. Striations measured in decametric-scale fault planes
791 subparallel to the NW to WNW-trending regional macrostructure in these sites are compatible with a
792 compressional D1 regime, characterized by a general NNE to NE-trending σ_1 (Fig. 14).

793 The NW-SE to W-E directed D3 extensional tectonics has also been detected in other sites located
794 close to the OBFZ. Site 21JE99 is located between the two branches of the S-OBFZ segment, north
795 of San José de Ocoa town (Fig. 5), where Maastrichtian limestones exhibit a penetrative brecciation
796 associated with decametric-scale NE-striking fault surfaces, dipping a high-angle to the NW and SE.
797 Slip measurements establish an oblique normal left-lateral movement on these planes and their
798 inversion establishes an extensional D3 regime characterized by a N121°E trending σ_3 (Fig. 13). Site
799 21JE103 is located ~1.5 km east of the S-OBFZ (Fig. 5), where decametric-scale fault planes
800 measured in basalts of the Tireo Group contain striations of an oblique normal kinematics in NW to
801 NE-trending and E-dipping faults. Inversion of these fault-slip data yields an extensional stress
802 regime characterized by a N256°E trending σ_3 (Fig. 13). Finally, slip measurements in N- to NNW-

803 striking fault planes at site 21JE108 (Fig. 5) indicates a predominance of dip-slip normal vectors,
804 compatible with a purely extensional regime with a N069°E trending σ_3 (Fig. 13).

805 **6. Discussion**

806 *6.1. Relations between neotectonics and Quaternary sedimentation in southern central Hispaniola*

807 Several researchers have previously described the uplift, folding and thrusting of the Cordillera
808 Central basement and the Peralta Belt during the lower Miocene to upper Pliocene time interval
809 (Heubeck & Mann, 1991; Mann et al., 1991a, b; Ramírez, 1995; Pubellier et al., 2000). The style of
810 this D1 deformation consisted of a SW-directed fold-and-thrust belt, which was developed above a
811 basal detachment horizon following a forward propagating sequence (Heubeck & Mann, 1991;
812 Hernaiz Huerta & Pérez-Estaún, 2002; this work). D1 is superimposed on a deformation produced
813 during the upper Eocene in the Peralta accretionary prism (Witschard and Dolan, 1990). Data
814 obtained in this study indicate that a large part of this deformation is syn-sedimentary and
815 characterized by the formation of a block-in-matrix fabric typical of a heterogeneous mélange. Syn-
816 sedimentary deformation was very probably produced by submarine gravitational processes,
817 triggered by instability in the basin slope and/or tectonics (e.g., Alonso et al., 2014; Escuder-Viruete
818 & Baumgartner, 2014; Súarez Rodríguez et al., 2017).

819 In this tectonic context, the San Juan-Azua basin constitutes the foreland flexural basin developed in
820 front of the SW-directed Peralta fold-and-thrust belt, and bounded to the NE by SW-directed thrusts
821 (Hernaiz Huerta & Pérez-Estaún, 2002; Díaz de Neira, 2004; this work). These basins were filled by
822 shelf marine, turbiditic, and continental sediments giving rise to a 4-km thick, shallowing and
823 coarsening upward regressive megasequence of lower Miocene to Lower Pleistocene age. D1
824 deformation propagated to the Azua basin sediments and continued until Early to Middle Pleistocene
825 times, which is the age of the Arroyo Seco Formation deformed in the footwall of the Peralta frontal
826 thrust (Díaz de Neira & Solé Pont, 2002). As documented in the present work, these coarse-grained

827 continental deposits were folded and thrusted in the footwall of the San Juan-Pozos fault zone,
828 current frontal thrust of the Peralta Belt.

829 After a sedimentary hiatus, uplift and erosion of the resulting relief fed several staircase alluvial fan
830 systems, developed at different topographic levels on the southern slopes of the Cordillera Central
831 probably since the Early Pleistocene (Díaz de Neira, 2000; Pérez-Valera, 2010). The ages obtained
832 by optically stimulated luminescence geochronology between 43.8 ± 8.3 ka and 5.9 ± 0.6 ka for the
833 intermediate and young alluvial fan systems indicate the uplift continued, at least, during the Late
834 Pleistocene to the Holocene (Escuder-Viruete et al., 2023). The older alluvial fan is not yet been
835 dated, but probably also records uplift and erosion during the Middle Pleistocene.

836 In both the eastern and western sectors of the Ocoa Bay, these alluvial fan systems unconformably
837 overlie a fossil coral reef terrace developed during the MIS 5e (118-128 ka) and 5c (~105 ka) stages
838 in the Last Interglacial. Therefore, the fluvial incision and the progradation/aggradation of the
839 intermediate and young alluvial fans were also controlled by the global sea level fall and its
840 variations during the Last Glacial. The coral terrace also includes reworked corals grown during MIS
841 7 and 9 stages. However, no remains have been found of coral terraces built during these stages in
842 the Ocoa Bay, so erosion might eliminated them.

843 On the other hand, the Quaternary coral reef terrace and the alluvial fans unconformably overlie the
844 D1 large-scale structure of NW-trending and SW-verging folds and thrusts that affect the NE margin
845 of the Azua basin. Therefore, the regional pervasive D1 deformation ends, at least in southern central
846 Hispaniola, during the Lower Pleistocene. Late Pleistocene to Holocene alluvial fan and pediment
847 deposits are all offset by strike-slip faults of the D2 event, implying that the more recent tectonic
848 activity is mainly partitioned in the Ocoa-Bonao and Beata Ridge fault zones, as well as by faulting
849 in related structures. Finally, both the coral reef terraces of the MIS 5e and 5c stages and the

850 overlapping alluvial fan systems of Late Pleistocene to Holocene age appear deformed by the normal
851 faults of the D3 event in the Ocoa Bay sector.

852 *6.2. Evolution of the Quaternary stress regime in southern central Hispaniola*

853 The geometric characteristics of the faults at all scales, the striae sets in their planes, the compatible
854 stress tensors and their chronological succession, constrained by offset relations with dated
855 lithostratigraphic units, define three types of neotectonic fault kinematics in southern central
856 Hispaniola (Table 1). These types are: thrust and reverse faulting with horizontal σ_1 and σ_2; strike-
857 slip faulting with horizontal σ_1 and σ_3; and extensional faulting with vertical σ_1 (Fig. 15; see also
858 Supporting Information S6). Each type of fault kinematics is related to a different deformation event,
859 characterized by a specific state of stress, whose development changes geographically throughout
860 southern central Hispaniola (Fig. 16).

861 Throughout the Cordillera Central domain, Sierra Martín García and San Juan-Azua basin there is
862 evidence of slip on thrust and reverse faults related to a NNE to NE-trending compressional D1
863 stress regime (Fig. 16). These NW-trending D1 structures deform the middle Eocene-lower Miocene
864 sedimentary rocks of the Río Ocoa Group, as well as its substrate of the Peralta Belt accretionary
865 prism, the early/middle Miocene to middle Pliocene marine turbiditic and platform sediments of the
866 San Juan-Azua foreland basin, and the upper Pliocene to Early Pleistocene clastic continental
867 deposits of the Arroyo Seco Formation (Heubeck & Mann, 1991; Díaz de Neira & Solé Pont, 2002;
868 Hernáiz Huerta & Pérez-Estaún, 2002; among others). A similar structural relationship has been
869 described along the southern border of the Chaîne des Matheux in Haiti, where SW-directed thrusts
870 deform rocks of middle to upper Miocene age (Pubellier et al., 2000). Upper Miocene to lower
871 Pliocene onset of uplift in the Cordillera Central is simultaneous with uplift in the Sierra de Neiba,
872 with both ranges providing the clastic sedimentary source for the eastern San Juan and Azua
873 (piggyback) basins. The pre-Early Pleistocene folding and thrusting D1 event has been related to the

874 collision between CLIP-related units of the Southern Hispaniola Peninsula and the island-arc crust of
875 the Cordillera Central (Heubeck & Mann, 1991; Mann et al., 1991b).

876 Stress tensors obtained for D1 event indicate a general NE-trending σ_1 axis, ranging between
877 N017°E and N070°E directions, with a relatively well-constrained maximum value in the count-
878 contours stereoplot at N202°E, plunging 06° to the SW (Fig. 15). A similar NE to ENE-directed
879 shortening was obtained by Ramírez (1995) from the analysis of the faults that deform the Arroyo
880 Blanco Fm. In the calculations, the orientation of σ_1 has been restored at sites in the eastern Ocoa
881 Bay that have undergone a post-D1 clockwise rotation. The vertical arrangement of σ_3 axis in the
882 computed stress tensors is consistent with deformation by thrusting. The R stress ratio has values of
883 0.50 ± 0.25, indicating stress tensors close to pure compression. Therefore, the regional D1 stress
884 regime consisted of a NE-trending subhorizontal compression. However, R ratio presents some
885 values of 0.87 and 0.92 (21JE73 and 21JE79 sites), which means that the maximum and minimum
886 σ_H axes are close in magnitude and higher that σ_V ($\sigma_1 \approx \sigma_2$). These R values suggest that a D1
887 deformation locally characterized by a radial compression regime. On the other hand, the WSW-
888 directed GPS motions measured in JUAN, CONS and BARA stations, located away from important
889 D2 structures, are suborthogonal to the strike of the San Juan-Pozos and Barahona fault zones, as
890 well as the thrust structures in the Cordillera Central and Peralta Belt domains. Therefore, present-
891 day reverse faulting dominates active D1 structures (Fig. 16). This argument agrees with thrust
892 kinematics and reverse stress regime obtained for D1 from field permanent deformation.

893 The NNE to NE-trending strike-slip D2 stress regime has been deduced near the Ocoa-Bonao-La
894 Guácara fault zone, particularly in the eastern sector of the Ocoa Bay and in the margins of the San
895 José de Ocoa and Rancho Arriba intramountain basins (Fig. 16). This strike-slip deformation has also
896 been observed in the vicinity of the Beata Ridge fault zone, in the western sector of the Ocoa Bay,
897 and in relation to NE to ENE-striking left-hand strike-slip faults that cut and displace D1 thrusts in

898 the Cordillera Central. Therefore, D2 strike-slip faults cut and displace the D1 fold-and-thrust
899 structures, as described in previous works (Ramírez, 1995; Hernáiz Huerta & Pérez-Estaún, 2002;
900 Pérez-Valera, 2010).

901 D2 strike-slip faults deform the Quaternary deposits in several places, as the fossil coral reef terrace
902 built during the MIS 5e and 5c stages in the SW and NE flanks of the Sierra Martín García and
903 Bahoruco. Recent field-data collected in the eastern sector of Ocoa Bay (Escuder-Viruete et al.,
904 2023), indicate that D2 strike-slip faults subparallel to the O-OBFZ segment deform an alluvial fan
905 of latest Pleistocene age, but are locally fossilized by a younger alluvial fan of Holocene age.
906 Nonetheless, the Ocoa-Bonao-La Guácara fault zone cuts geomorphic features along its path, such as
907 Late Pleistocene-Holocene alluvial fans, fluvial terraces and streams in the San José de Ocoa and
908 Rancho Arriba intramountain basins, which collectively evidence active D2 deformation. Therefore,
909 the D2 stress-field continues through the latest Pleistocene and most likely today. This interpretation
910 is consistent with the moment tensor solutions of strike-slip faulting calculated for the 1977 and 1988
911 earthquakes (CMT catalogue; Ekström et al., 2012), whose epicenters are located very close to the
912 OBFZ trace.

913 The change from a D1 compressional to a D2 strike-slip stress regimes took place during the Early
914 and Middle Pleistocene (or sometime in the Early Pleistocene). This change could be related to the
915 indentation of the eastern sector of the Beata Ridge in southern Hispaniola, as part of the Caribbean
916 oceanic plateau collision in the back-arc region of the Hispaniola microplate. This processes could
917 produced the large-scale drag of the pre-existing D1 structures in the eastern Ocoa Bay and
918 generated large-scale conjugate D2 strike-slip faults on the margins of the aseismic ridge indenter. In
919 this sense, the geometric characteristics of the D2 deformation, such as landward deflection of the
920 Muertos trench axis and development of conjugate strike-slip faults and back-thrusts, are analogous
921 to those produced above a subducted conical seamount or submarine aseismic ridge (Ranero and von

922 Huene, 2000; Sak et al., 2009; Gardner et al., 2013), as it has been faithfully reproduced by sandbox
923 analogue models of such convergent margins (Dominguez et al., 2000).

924 Stress tensors of D2 event indicate a general NE-trending σ_1 axis, comprised between N015°E and
925 N055°E directions, with a relatively well-constrained maximum value at N045°E, plunging 01° to
926 the NE (Fig. 15). The dispersion of σ_1 axes is due to fault-slip measures in sites located in the San
927 José de Ocoa Basin, where the S-OBFZ trends N-S, or probably due to the reorientation of the
928 regional stress field that occurs around this large-scale strike-slip fault. The subvertical arrangement
929 of the σ_2 axes indicates that the D2 deformation took place in a strike-slip regime, characterized by a
930 NE-trending subhorizontal shortening for R-values ranging between 0.21 and 0.60, with prevalence
931 of values close to 0.5. These R-values suggest a deformation mode close to pure strike-slip,
932 consistent with the low-pitch angle of the displacement vectors observed in D2 strike-slip faults and
933 some focal mechanism solutions. Note that the SW-directed GPS motion measured in the TORT
934 station is parallel to the NE-SW strike of the nearby Beata Ridge fault segment, implying a present-
935 day pure strike-slip faulting along this D2 structure (Fig. 16).

936 D3 faults can be grouped into two geometric families: D3a and D3b. The first family includes NE-
937 SW to NNE-SSW trending normal and oblique normal D3a faults. Although the number of
938 computed stress tensors is limited, inversion of fault-slip data establishes a general NW-SE trending
939 extensional stress regime D3a (Fig. 15). This extensional stress regime has only been detected in the
940 western Cordillera Central-Peralta Belt domains and in sectors close to the S-OBFZ segment, as the
941 San José de Ocoa and Rancho Arriba intramountain basins (Fig. 16). The orientation of σ_3 axes has a
942 high dispersion, ranging between N103°E and N168°E, for values of the R ratio very close to 0.5,
943 establishing stress tensors of pure extension. The age of the D3a event could not be precisely
944 established. However, these normal faults affect the volcanic rocks of Pleistocene age of the Valle
945 Nuevo area whose K-Ar ages are 0.5 ± 0.3 and 0.3 ± 0.2 Ma (Vespucci, 1988; Kamenov et al., 2011;

946 and references herein) and, therefore, its age is at least post-Middle Pleistocene. The alignment of the
947 emissive centers of the Quaternary calc-alkaline to mafic alkaline volcanism in the region follows a
948 NE-SW strike (Fig. 16), so the NW-directed extension during D3a could have favoured the opening
949 of NE-SW striking planes and the rise of magmas. Alternatively, the rise of magmas could have
950 taken place in favour of releasing bends formed during D2 deformation. Hot springs and associated
951 travertine deposits in the volcanic region indicate that geothermal activity continues today.

952 The second family includes WNW to W-striking dip-slip normal faults that established an N to
953 NNE-trending extensional D3b stress regime. Its development is geographically limited to the
954 surroundings of Ocoa Bay (Fig. 16). D3b normal faults deform the coral reef terraces of the MIS 5e
955 and 5c stages (22JE26, Playa Azul; 21JE126, Playa Las Caobitas; and 20JE04, Palmar de Ocoa sites)
956 and the overlapping alluvial fan of Late Pleistocene to Holocene? age (21JE127 and 22JE15 sites).
957 Inversion of 12 fault-slip data sets gives rise to NNE-trending σ_3 axes, comprised between N003°E
958 and N023°E directions, with a relatively well-constrained maximum value at N022°E, plunging 6° to
959 the NE (Fig. 15). The subvertical arrangement of the σ_1 axes and the obtained R-values close to 0.5
960 indicate stress tensors close to pure extension.

961 In summary, a relatively constant NE-trending horizontal shortening, parallel to the current direction
962 of plate convergence established by GPS measurements, controlled the evolution of the Quaternary
963 stress tensor in southern central Hispaniola. This evolution included a D1 event of compression
964 followed by a D2 near pure strike-slip event, which was locally coeval by a more heterogeneous and
965 geographically localized D3 regime of pure extension. The successive changes in the stress regime
966 were related to a permutation of σ_3 by σ_2 vertical stress between D1 and D2 events, and to a
967 permutation of σ_2 by σ_1 vertical stress between D2 and D3 events (Fig. 15).

968 *6.3. Origin of the extensional tectonics localized in the Ocoa Bay*

969 Figure 13 shows the coast of southern central Hispaniola intermittently covered by the fossil coral
970 reef terrace that grew as a fringing reef during MIS 5e/5c stage and currently ranges in elevation
971 from 0 to 20 m above sea level. The MIS 5e stage corresponds to a relatively long period of high-sea
972 level that took place during the 118–128 ka interval in the Last Interglacial, when the sea level was
973 between 2 and 6 m above the current level (e.g., Schellmann & Radtke, 2004). The existence of coral
974 reef terraces of the MIS 5e/5c stage at elevations between 1 and 25 m above the current sea level can
975 be explained by active tectonics that has uplifted in variable amounts the southeastern margin of
976 Cordillera Central, the Sierra Martín García and the Sierra Bahoruco. Assuming a *Diploria* sp.
977 growth depth of ~2 m and an average sea level height during the MIS 5e of +2.0 m (see details in
978 Escuder-Viruete et al., 2020), the minimum uplift rates for the terrace range between 0.01 and 0.22
979 m/ka. The absence of the coral terrace, as well as of other coral terraces presumably built up during
980 older MIS stages, can be explained as due to erosion or to being located at elevations below present
981 sea level as a consequence of later subsidence. In our case, the absence of the coral terrace of the
982 MIS 5c/5e stage coincides with the reentrant of the Ocoa Bay affected by D3b extensional tectonics.

983 Figure 13 also shows two outcrops of the modern fringing reef raised between 0.5 and 3 m above sea
984 level, which are currently subjected to strong marine erosion. An specimen of coral *Diploria* sp.
985 collected in the uppermost levels of the terrace at Playa Caracoles (21JE124 site) have provided an
986 U-Th ages of 0.730 ± 0.01 ka. This age indicates growth of the coral terrace during MIS 1 stage in
987 the Middle Holocene. The calculated minimum uplift rate for the terrace is 4.11 m/ka.

988 Thus, the spatial distribution of the topography in the Ocoa Bay, the D3b extensional deformation,
989 outcrops of the coral reef terraces and uplift rates are, to the first order, controlled by the subducting
990 Beata Ridge of the Caribbean plate. This is because the Muertos accretionary prism that makes up
991 the margin wedge on the Ocoa Bay must deform around this indenting bathymetric feature. The
992 topographically low area of the Ocoa Bay lines up along the relative plate motion vector with the
993 Beata Ridge indenter. The highest uplift rates are recorded along the central northern coast of the

994 Ocoa Bay and decrease parallel to the trench and perpendicular to the Beata Ridge to the E
995 (southeast coast of the Cordillera Central) and the W (Sierra Martín García).

996 This pattern in the distribution of the D3b deformation and vertical motions can be interpreted as a
997 wave of rapid uplift followed by subsidence that propagates parallel to the current plate motion
998 vector in the Ocoa Bay, as a response to the subduction of bathymetric irregularities in the Beata
999 Ridge. Following the deformation mechanism proposed for seamount subduction in the New
1000 Hebrides and Solomon Arcs (e.g., Taylor et al. 2005), the passage of a subducting bathymetric high
1001 produces a history of rapid uplift and subsequent collapse and subsidence in a block of similar
1002 dimensions of the upper plate.

1003 Along the Ocoa Bay, where the Beata Ridge indenter currently entering the Muertos Trench,
1004 macroscale WNW to W-striking dip-slip normal faults and mesoscale fault-slip data, are consistent
1005 with SSW to S-directed extension perpendicular to the margin (Fig. 16). These steeply-dipping
1006 normal faults may be a consequence of the collapse of the margin, constituted by relatively soft
1007 sedimentary rocks of the Muertos accretionary prism, in the wake of the stronger mafic igneous
1008 rocks of the subducting Beata Ridge that produce a basal erosion of the upper plate (Ramero & von
1009 Huene, 2000; Sak et al., 2009; Gardner et al., 2013; Vannucchi et al., 2013). The subvertical and NE-
1010 striking faults formed during D2, such as the N-BRFZ and O-OBFZ segments, are arranged at high
1011 angles to the margin and may have accommodated differential displacements during D3, acting as
1012 transfer faults. Ocoa Bay would therefore be an embayment of ~20 km wide and ~25 km length,
1013 formed by the passage of a bathymetric high in the subducting Beata Ridge. A similar mechanism
1014 has been proposed along the northern Hispaniola-Puerto Rico margin, where subduction/collision of
1015 bathymetric highs built on the Atlantic oceanic crust has resulted to basal erosion in the upper plate
1016 and forearc collapse (Grindlay et al., 2005; Escuder-Viruete and Pérez, 2020).

This interpretation is favored by the absence of the coral terrace of the MIS 5e/5c inboard of the Beata indenter (Fig. 13), which must have been uplifted and eroded or sunk by D3b extensional tectonics. In turn, the gravimetric and magnetic anomaly produced by the CLIP magnetic basalts that characterizes the surroundings of Ocoa Bay (Fig. 4) suggests a thinning of the upper plate wedge in the submarine portion of the margin. In this tectonic context, the high uplift rates detected in the uplifted modern coral terrace indicate a new episode of rapid uplift and future subsidence of the margin during continued subduction of the Beata Ridge.

Although the role of seamounts/aseismic ridge subduction in the plate-margin seismicity is disputed, e.g. enhancing seismic coupling (e.g., Bangs et al., 2015) versus decreasing the degree of coupling and limiting the lateral propagation of megathrust-earthquake rupture planes (e.g., Bonnet et al., 2019), the 1751 earthquake occurred in the vicinity of the Ocoa Bay and destroyed the city of Azua. The presence of the subducting Beata Ridge in high-resolution bathymetric swath maps of the Caribbean-Hispaniola plate boundary region and in seismic reflection profiles across the Muertos Trench (e.g., Granja Bruña et al., 2014), together with the proposed location of the Azua earthquake intensity center in the Ocoa Bay (Bakun et al., 2012), suggest that this M_w = 7.5 event may have resulted from the rupture of a ridge asperity in the subduction and can therefore be repeated in the future.

6.4. Definition of seismotectonic structures in southern central Hispaniola

The characterization of seismotectonic structures has been previously carried out in some sectors of Hispaniola Island (Frankel et al., 2010; Bertil et al., 2015; Escuder-Viruete et al., 2020; Terrier-Sedan and Bertil, 2021). Used criteria in the definition were: geodynamic situation; geological, stratigraphic and/or tectonic evidence of recent activity; kinematic type of fault and rate of displacement; and associated historical and/or instrumental seismicity. The definition of these large-scale active structures is critical since it allows for establishing seismotectonic zonation models of

1041 the area under consideration, which is fundamental for the quantitative seismic hazard assessment.
1042 However, this approach requires updating the inventory of active structures as tectonic and
1043 seismological knowledge increases.

1044 The previous works and the new data presented in this work allow updating the main seismotectonic
1045 fault zones structures in southern central Hispaniola, including its adjacent offshore sector. They are:
1046 San Juan-Pozos (Mann et al., 1991a); Matheux-Sierra de Neiba (MAFZ, Hernaiz Huerta et al.,
1047 2007); Bahoruco (BAFZ or Barahona Thrust; Rodríguez et al., 2018); Beata Ridge (Mauffret and
1048 Leroy, 1999); Muertos Trough (Granja Bruña et al., 2009; 2014); Ocoa-Bonao-La Guacara (Pérez-
1049 Estaún et al., 2007; Escuder-Viruete et al., 2023); and probably the eastern end of the Enriquillo-
1050 Plantain Garden (EPGFZ; Mann et al., 1995).

1051 The attribute compilation of these seismotectonic structures is outlined in Table 2, including the fault
1052 or segment name, deformation mechanism, estimated maximum magnitude (Mw), known biggest
1053 earthquake (magnitude in M_w), estimated displacement rate, length, strike and dip, and width of the
1054 fault zone. Following Bertil et al. (2015), the maximum magnitude of rupture for each fault/segment
1055 was estimated using the major recorded historical earthquake (Terrier-Sedan and Bertil, 2021), or its
1056 geometric parameters (e.g. Wells and Coppersmith, 1994), taking into account its degree of
1057 uncertainty. Displacement rates for each seismogenic structure were derived from geological
1058 mapping (SYSMIN Project, 2010; Escuder-Viruete, 2022; Escuder-Viruete et al., 2023; this work),
1059 geodetic GPS measurements (Calais et al., 2002; Manaker et al., 2008), or calculated in the present
1060 study through empirical relationships (e.g. Wells and Coppersmith, 1994).

1061 From this information, a simplified seismotectonic model was built that considers two types of
1062 seismic sources: subduction and strike-slip fault zones in which the seismicity of greater magnitude
1063 is concentrated; and superficial/upper crustal areas located between them where the seismicity is of

1064 moderate to low magnitude and is more homogeneously distributed. This seismotectonic model is the
1065 starting point for the seismic hazard assessment in southern central Hispaniola presented below.

1066 *6.5. Seismic hazard assessment in southern central Hispaniola*

1067 The seismic hazard assessment carried out in this work follows a probabilistic approach. Following
1068 the Cornell-McGuire methodology, the R-CRISIS calculation code (Ordaz et al., 2014) builds a
1069 probabilistic model that takes into account the spatial distribution of seismogenic sources, the
1070 occurrence and magnitude of earthquakes in time, and the attenuation characteristics of the strong
1071 motion in the ground. Thus, the R-CRISIS code computes the seismic hazard in terms of the
1072 probability of exceeding a peak ground acceleration (PGA) value for a specific site in a given period.

1073 For the seismic hazard assessment in southern Central Hispaniola, the previously described
1074 seismotectonic zonation model composed of subduction zones, main strike-slip fault zones and
1075 diffuse seismogenic zones located between them, was geometrically built as simplified 3-D
1076 polygonal surfaces of specific wildth. In these seismic sources, earthquakes can occur at any point of
1077 the source with equal probability (Ordaz et al., 2014). Functions selected to describe the attenuation
1078 of the ground motion acceleration with distance from the source are the same as those used by
1079 Frankel et al. (2010) and Benito et al. (2012) to evaluate the seismic hazard in Haiti after the 12
1080 October, 2010 earthquake. Parameters used to establish the seismic activity of each source and their
1081 uncertainties are included in Escuder-Viruete et al. (2020). The hazard analysis performed in this
1082 work did not take into account possible amplifications of the seismic parameters by site effects.
1083 Seismic hazard was computed in a rectangular point grid, framed by the coordinates: 17.960°N and
1084 18.835°N of latitude; -70.175°W and -71.250°W of longitude (WGS-84 projection system), with a
1085 point spacing of 0.025° in both directions. Results were converted in a continuous surface using an
1086 inverse distance squared weighted interpolation algorithm.

Figure 17 includes the results of the seismic hazard assessment in southern central Hispaniola, expressed as PGA intervals (values in cm/s^2) and for a return period of 475 years (i.e., for a probability of exceedance of 10% in 50 years). Modeled minimum and maximum PGA values are 86 cm/s^2 and 857 cm/s^2, respectively, with a mean (and standard deviation) of 386.7 (148.0). Therefore, the regional seismic hazard values range from low to very high. PGA zoning defines an elongated pattern sub-parallel to the main fault zones. Seismic hazard is higher in the Ocoa Bay, along the San José de Ocoa valley in the southern Cordillera Central, and in the topographic transition between the northern Cordillera Central and the eastern Cibao Valley. It decreases towards the NW and SE regions. This seismic hazard zoning contrasts with the previously proposed by Frankel et al. (2010), Benito et al. (2012) and Bertil et al. (2010, 2015), which did not take into account all the seismic sources included in the present work, particularly the Ocoa-Bonao-La Guácara fault zone.

With this seismotectonic model, the highest PGA values (> 600 cm/s^2) are associated with the N-BRFZ, O-OBFZ and C-OBFZ segments. Branches of the S-OBFZ segment set intermediate to high values (500-650 cm/s^2). The C-OBFZ segment also has associated high PGA values (>650 cm/s^2), which decrease to intermediate and low values westward along the W-OBFZ segment (250-450 cm/s^2). The superficial trace of the O-MT segment of the Muertos Trough also has associated high PGA values (600 cm/s^2), which extend into depth following the subduction interface. The BAFZ has associated intermediate PGA values in its connection to the BRFZ, which also decrease westward. The S-JPFZ presents high PGA values at its SE end (500-700 cm/s^2), where it is displaced by the N-BRFZ, decreasing towards the NW. The Hispaniola fault zone has also been included in the modeling, giving rise to intermediate values of the PGA that become high in its central segment. The E-EPGFZ segment also has associated intermediate to low PGA values (400-500 cm/s^2).

In summary, the highest PGA values in southern central Hispaniola are associated with N-BRFZ, O-OBGFZ and A-MT segments, whose traces frame a triangular zone centered on Ocoa Bay where the seismic hazard is very high. As described, this sector includes the intensity center estimated for the

1751 Azua earthquake (M_w 7.5), which according to some historical accounts gave rise to a tsunami in the bay. For Bakun et al., (2012), this event could be produced by the Enriquilo-Platain Garden fault zone or, as an alternative source, the Muertos deformation belt. The results of the PGA modeling rule out the EPGFZ as a source and indicate that the BRFZ, the O-MT and, less likely, the O-OBFZ, could have generated this earthquake.

Historical records indicate that the greatest effects of the 1615, 1684, 1691 and 1911 earthquakes (M_w from 6.0 to 7.5) were in the southern sector of the Central Cordillera. However, the determination of its seismic source could not be confidently established with the available data, since these strong earthquakes did not produce known surface ruptures. Future neotectonic and paleoseismological studies, together with the seismic hazard modeling, may shed light on the active fault zones that generated large earthquakes in the region and therefore allow updating the spatial distribution of the seismic hazard.

7. Conclusions

The characterization of active tectonics and the main seismotectonic faults in southern central Hispaniola was developed from tectonic and geomorphologic field observations, the regional gravimetric and magnetic data interpretation, and the inversion of fault-slip data. The main conclusions of this work are:

(1) A relatively constant NE-directed shortening controlled the geometry and kinematics of main active faults in central southern Hispaniola, as well as the evolution of the Quaternary stress regime.

(2) Quaternary stress regime evolution includes a compressional D1 event, which gave rise to the large-scale fold and thrust structure in the Cordillera Central, Peralta Belt, Sierra Martín García and San Juan-Azua basin.

(3) D1 was followed by a strike-slip D2 stress regime, partitioned into the N-S to NE-SW transverse Ocoa-Bonao-La Guácara and Beata Ridge fault zones, which are related to indentation of the Beata Ridge in southern Hispaniola from the Early to Middle Pleistocene and continues today.

(4) D2 was coeval by a more heterogeneous and geographically localized D3 extensional deformation.

(5) Several seismotectonic fault zones divide the region into a set of simplified seismogenic zones.

(6) Modeled highest peak ground acceleration values establish a very high seismic hazard. in the Ocoa Bay.

Acknowledgments

We would like to thank the support and infrastructures provided by the Servicio Geológico Nacional of the Dominican Republic, particularly to Yésica Pérez-Alejandro, Maria Betania Roque-Quezada and Edwin García. Detailed and constructive reviews made by Grenville Draper and Mark B. Gordon, as well as the editorial work by Yamirka Rojas-Agramonte and Claudio Faccenna, significantly improved the manuscript. The research was funded through PID2019-105625RB-C22 project of the MCIN/AEI/10.13039/501100011033 of the Spanish Government. Some works also received funding from the DR-T 1190 Project of the Banco Interamericano de Desarrollo (World Bank) and the FONDOCYT project 2015-1b3-118 of the MESCyT of the Dominican Republic Government.

Open Research

The data for this paper are contained in the text, figures and supporting information and can also be found in the data repository DIGITAL.CSIC which is the institutional repository of the Spanish National Research Council (Escuder-Viruete et al., 2023).

References

Alonso, J. L., Marcos, A. Villa, E., Suárez, A., Merino-Tomé, O. A. & Fernández, L. P. (2014). Mélanges and other types of block-in-matrix formations in the Cantabrian Zone (Variscan Orogen, northwest Spain): origin and significance. *International Geology Review*, 57 (5-8), 563-580. https://doi.org/10.1080/00206814.2014.950608

Alvarez, L., Chuy, T., García, J., Moreno, B., Álvarez, H., Blanco, M., Expósito, O., González, O., & Fernández, A. I. (1999) An earthquake catalogue of Cuba and neighboring areas. The Abdus Salam International Centre for Theoretical Physics. Internal Report IC/IE/99/1. Trieste, Italy. 62 pp.

Angelier, J. (1994). Fault slip analysis and paleostress reconstruction. In Hancock, P. (Ed.), *Continental Deformation*. Pergamon Press, United Kingdom, pp. 53–100.

Ayala, C., García-Lobón, J. L., Escuder-Viruete, J., Rey-Moral, C., Pérez-Estaún, A., & Padín-Debén, A. (2017). High-resolution magnetic, regional gravity and petrophysical characterization of the Dominican Republic tectonic domains with special focus on the Central Cordillera. *Boletín Geológico y Minero*, 128 (3): 611-631.

Bakun, W. H., Flores, C. H., & Uri, S. (2012). Significant earthquakes on the Enriquillo fault system, Hispaniola, 1500–2010: Implications for seismic hazard. *Bulletin of the Seismological Society of America*, 102, 18–30.

Bangs, N. L., McIntosh, K. D., Silver, E. A., Kluesner, J. W., & Ranero, C. R. (2015). Fluid accumulation along the Costa Rica subduction thrust and development of the seismogenic zone. *Journal of Geophysical Research: Solid Earth*, 120, 67–86.

Benford, B., Demets, C., & Calais, E. (2012). GPS estimates of microplate motions, northern Caribbean: evidence for a Hispaniola microplate and implications for earthquake hazard. *Geophysical Journal International*, 191 (2), 481-490.

Benito, O. B., Cervera B. J., Molina P. S., Navarro B. M., Doblas L. M., Martínez D. J. and others (2012). Évaluation de l'aléa et du risque sismique en Haïti dirigée vers la conception parasismique. Monografía ETSI en Topografía, Geodesia y Cartografía. Universidad Politécnica de Madrid, 137pp. http://oa.upm.es/view/institution/Topografia/

Bertil, D., Lemoine, A., Winter, T., & Belvaux, M. (2010). Microzonificación sísmica de Santiago – Republica Dominicana. Amenaza regional. Informe final, BRGM/RC-59107-FR. Bureau de Recherches Géologiques et Minières, France. 100 pp.

Bertil, D., Terrier, M., & Belvaux, M. (2015). Análisis de las fuentes sísmicas y evaluación de la amenaza sísmica regional del gran Santo Domingo. Estudio de la amenaza sísmica y vulnerabilidad física del Gran Santo Domingo. Informe Actividad, BRGM/RP-65305-FR. Bureau de Recherches Géologiques et Minières, France. 149 pp.

Bonnet, G., Agard, P., Angiboust, S., Fournier, M., & Omrani, J. (2019). No large earthquakes in fully exposed subducted seamount. *Geology*, 47, 407–410.

Byrne, D. B., Suarez, G., & McCann, W. R. (1985). Muertos Trough subduction, microplate tectonics in the northern Caribbean?. *Nature,* 317, 420–421.

Calais, E., Freed, A., Mattioli, G., Amelung, F., Jonsson, S., Jansma, P., Hong, S. H., Dixon, T., Prépetit, C., & Momplaisir, R. (2010). Transpressional rupture of an unmapped fault during the 2010 Haiti earthquake. *Nature Geoscience*, 3 (11), 1–6.

Calais, E., Symithe, S., Mercier de Lépinay, B. M., & Prépetit, C. (2016). Plate boundary segmentation in the northeastern Caribbean from geodetic measurements and Neogene geological observations. *Comptes Rendus Geoscience*, 348, 42-51.

Célérier, B., Etchecopar, A., Bergerat, F., Vergely, P., Arthaud, F., & Laurent, P. (2012). Inferring stress from faulting: from early concepts to inverse methods. *Tectonophysics*, 581, 206-219.

Cheng, H., Edwards, R. L., Hoff, J., Gallup, C. D., Richardsm D. A., & Asmerom, Y. (2000). The half-lives of uranium-234 and thorium-230. *Chemical Geology*, 169, 17-33.

Corbeau, J., Rolandone, F., Leroy, S., de Lépinay, B.M., Meyer, B., Ellouz-Zimmermann, N., & Momplaisir, R., 2016. The northern Caribbean plate boundary in the Jamaica Passage: structure and seismic stratigraphy. Tectonophysics 675, 209–226.

Corbeau, J., Rolandone, F., Leroy, S., Guerrier, K., Keir, D., Stuart, G., Clouard, V., Gallacher, R., Ulysse, S., Boisson, D., Bien-Aime Momplaisir, R., Saint Preux, F., Preprtit, C., Saurel, J.-M., de Lépinay, B.M., & Meyer, B. (2017). Crustal structure of the western Hispaniola (Haiti) from teleseismic receiver function study. *Tectonophysics*, 709, 9–19.

Corbeau, J., Gonzalez, O. L. Clouard, V., Rolandone, F., Leroy, S., Keir, D., Stuart, G., Momplaisir, R., Boisson, D. & Prépetit, C. (2019). Is the local seismicity in western Hispaniola (Haiti) capable of imaging northern Caribbean subduction? *Geosphere*, 15, 6, 1738–1750. https://doi.org/10.1130 /GES02083.1.

Díaz de Neira, J. A. (2000). Evolución geomorfológica del Llano de Azua (Sur de la República Dominicana). *Acta Geológica Hispánica*, 37, 207-227.

Díaz de Neira, J. A. (2004). Mapa Geológico de la Hoja a E. 1:50.000 nº 5970-I (Barahona). Dirección General de Minería, Santo Domingo. 68 pp. https://www.sgn.gob.do

Díaz de Neira, J. A., & Solé Pont, F. J. (2002). Precisiones estratigráficas sobre el Neógeno de la cuenca de Azua (República Dominicana). *Acta Geologica Hispanica*, 37, 163-181.

Dolan, J., Mann, P., De Zoeten, R., Heubeck, C., & Shiroma, J. (1991). Sedimentologic, stratigraphic, and tectonic synthesis of Eocene-Miocene sedimentary basins, Hispaniola and Puerto Rico. In P. Mann, G. Draper & J. F. Lewis (Eds.), *Geologic and Tectonic Development of the North America-Caribbean Plate Boundary in Hispaniola*. Geological Society of America Special Paper 262, 17–26.

Dolan, J. F., Mullins, H. T., & Wald, D. J. (1998). Active tectonics of the north-central Caribbean region: oblique collision, strain partitioning and opposing slabs. In J. Dolan, & P. Mann (Eds.), *Active Strike-Slip and Collisional Tectonics of the Northern Caribbean Plate Boundary in Hispaniola*. Geological Society America Special Paper 326: 1-61

Dominguez, S., Malavieille, J., & Lallemand, S.E. (2000). Deformation of accretionary wedges in response to seamount subduction: Insights from sandbox experiments. *Tectonics* 19, 182-196.

Draper, G., Mann, P., & Lewis, J. F. (1994). Hispaniola. In S.K. Donovan, & T. A. Jackson (Eds.), *Caribbean Geology: An introduction. Jamaica*. University of the West Indies Publishers Association, 129-150.

Driscroll, N. W., & Diebold, J. B. (1998). Deformation of the Caribbean region: one plate or two? *Geology*, 26 (11), 1043–1046.

Dürkefälden, A., Hoernle, K., Hauff, F., Wartho, J.A., Bogaard, P. van den, & Werner, R. (2019). Age and geochemistry of the Beata Ridge: Primary formation during the main phase (~89 Ma) of the Caribbean Large Igneous Province. *Lithos*, 328–329, 69-87.

Ekström, G., Nettles, M., & Dziewonski, A. M. (2012). The global CMT project 2004-2010: Centroid-moment tensors for 13,017 earthquakes. *Physics of the Earth and Planetary Interiors*, 200-201, 1-9.

Escuder Viruete, J. (2022). Microzonificación sísmica y escenario de daños en los cascos urbanos de Barahona y Jimaní: Neotectónica, Sismotectónica y Modelización de la Amenaza Sísmica. Fortalecimiento del Sistema Nacional de la Gestión de Riesgo de Desastre (DR-T 1190), República Dominicana. *Banco Interamericano de Desarrollo, World Bank. Informe Final*. 153 pp. 6 Anexos.

Escuder-Viruete, J., & Baumgartner, P. O. (2014). Structural evolution and deformation kinematics of a subduction-related serpentinite-matrix mélange, Santa Elena Península, northwest Costa Rica. *Journal of Structural Geology*, 66, 356-381.

Escuder Viruete, J., & Pérez, Y. (2020). Neotectonic structures and stress fields associated with oblique collision and forearc sliver formation in northern Hispaniola: Implications for the seismic hazard assessment. *Tectonophysics*, 784, 228452.

Escuder-Viruete, J., Joubert, M., Urien, P., Friedman, R., Weis, D., Ullrich, T., & Pérez-Estaún, A. (2008). Caribbean island-arc rifting and back-arc basin development in the Late Cretaceous: geochemical, isotopic and geochronological evidence from Central Hispaniola. *Lithos*, 104, 378-404. doi:10.1016/j.lithos.2008.01.003.

Escuder-Viruete, J., Pérez-Estaún, A., Gabites, J., & Suárez-Rodríguez, Á. (2011a). Structural development of a high-pressure collisional accretionary wedge: The Samaná complex, northern Hispaniola. *Journal of Structural Geology*, 33, 928-950.

Escuder-Viruete, J., Pérez-Estaún, A., Booth-Rea, G., & Valverde-Vaquero, P. (2011b). Tectonometamorphic evolution of the Samaná complex, northern Hispaniola: Implications for the burial and exhumation of high-pressure rocks in a collisional accretionary wedge. *Lithos*, 125, 190-210.

Escuder-Viruete, J., Valverde-Vaquero, P., Rojas-Agramonte, Y., Gabites, J., & Pérez-Estaún, A. (2013). From intra-oceanic subduction to arc accretion and arc-continent collision: Insights from the structural evolution of the Río San Juan metamorphic complex, northern Hispaniola. *Journal of Structural Geology*, 46, 34-56.

Escuder-Viruete, J., Joubert, M., Abad, M., Pérez-Valera, F., & Gabites, J. (2016a). The basaltic volcanism of the Dumisseau Formation in the Sierra de Bahoruco, SW Dominican Republic: a record of the mantle plume-related magmatism of the Caribbean large Igneous Province. *Lithos*, 254–255, 67–83.

Escuder-Viruete, J., Súarez, A., Gabites, J., & Pérez-Estaún, A. (2016b). The Imbert Formation of northern Hispaniola: a tectono-sedimentary record of arc-continent collision and ophiolite emplacement in the northern Caribbean accretionary prism. *Solid Earth Discuss,* 6, 1-50.

Escuder Viruete, J., Beranoaguirre, A., Valverde-Vaquero, P., & Mcdermott, F. (2020). Quaternary deformation and uplift of coral reef terraces produced by oblique subduction and underthrusting of the Bahama Platform below the northern Hispaniola forearc. *Tectonophysics*, 796, 228631.

Escuder-Viruete, J., Fernández, F. J., Pérez Valera, F., & Medialdea, A. (2023). Present-day accommodation of Caribbean-North American oblique plate convergence through the Ocoa-Bonao-La Guacara fault zone, southern central Hispaniola: a transition zone between oceanic subduction and arc-oceanic plateau collision. Tectonics 42, e2022TC007618. https://doi.org/10.1029/2022TC007618

Escuder-Viruete, J., Fernández, F. J., Pérez Valera, F., & McDermott, F. (submitted). Active tectonics, Quaternary stress regime evolution and seismotectonic faults in southern central Hispaniola: implications for the quantitative seismic hazard assessment. [Dataset]. DIGITAL.CSIC repository.

Fankhauser, A., McDermott, F., & Fleitmann, D. (2016). Episodic speleothem deposition tracks the terrestrial impact of millennial-scale last glacial climate variability in SW Ireland. *Quaternary Science Review*, 152, 104-117. http://dx.doi.org/10.1016/j.quascirev.2016.09.019

Flores, C. H., ten Brink, U. S., & Bakun, W. H. (2011). Accounts of damage from historical earthquakes in the northeastern Caribbean, to aid in the determination of their location and intensity magnitudes, U.S. Geological Survey Open File Report. 2011–1133, 226 pp.

Frankel, A., Harmsen, S., Mueller, Ch., Calais, E., & Haase, J. (2011). Seismic Hazard Maps for Haiti. *Earthquake Spectra*, 27, S1, S23-S41.

García Lobón, J. L., & Rey Moral, C. (2004). Magnetismo y radiación gamma natural de la República Dominicana. *Boletín Geológico y Minero,* 115 (1), 153-168.

García-Lobón J. L., & Ayala. C. (2007). Cartografía geofísica de la República Dominicana: datos de densidad, susceptibilidad magnética y magnetización remanente. *Boletín Geológico y Minero*, 118 (2), 175-194.

Gardner, T. W., Fisher, D. M., Morell, K.D., & Cupper, M. L. (2013). Upper-plate deformation in response to flat slab subduction inboard of the aseismic Cocos Ridge, Osa Peninsula, Costa Rica. *Lithosphere*, 5, 3, 247-264.

Granja Bruña, J. L., ten Brink, U. S., Carbó-Gorosabel, A., Muñoz-Martín, A. & Gómez Ballesteros, M. (2009). Morphotectonics of the central Muertos thrust belt and Muertos Trough (northeastern Caribbean). *Marine Geology*, 263, 7–33.

Granja Bruña, J. L., Carbó-Gorosabel, A., Llanes Estrada, P., Muñoz-Martín, A., ten Brink, U. S., Gómez Ballesteros, M., Druet, M., & Pazos, A. (2014). Morphostructure at the junction between the Beata ridge and the Greater Antilles island arc (offshore Hispaniola southern slope). *Tectonophysics*, 618, 138–163.

Grindlay, N. R., Mann, P., Dolan, J. F., van Gestel, J. P. (2005). Neotectonics and subsidence of the northern Puerto Rico–Virgin Islands margin in response to the oblique subduction of high-standing ridges. *Geological Society American Special Paper*, 385, 31–60.

Hernáiz-Huerta, P. P., & Pérez-Estaún, A. (2002). Estructura del cinturón de pliegues y cabalgamientos de Peralta, República Dominicana. *Acta Geológica Hispánica*, 37, 183-205.

Hernáiz-Huerta, P. P., Díaz de Neira, J. A, García Senz, J., Deschamps, I., Lopera, E., Escuder Viruete, J., Ardévol Oró, Ll., Granados L., Calvo J. P. & Pérez Estaún, A. (2007a). La estratigrafía de la Sierra de Neiba, República Dominicana. *Boletín Geológico y Minero*, 118, 313-336.

Hernáiz-Huerta, P. P., Díaz de Neira, J.A, García Senz, J., Deschamps, I., Genna, A., Nicole, N., Lopera, E., Escuder Viruete, J., Ardévol Oró, Ll. & Pérez Estaún, A. (2007b). La estructura

de la sierra de Neiba, margen norte de la sierra de Bahoruco, Sierra de Martín García y cuenca de Enriquillo de la República Dominicana: un ejemplo de deformación transpresiva. *Boletín Geológico y Minero*, 118, 337-357.

Heubeck, C., & Mann, P. (1991). Structural geology and Cenozoic tectonic history of the southeastern termination of the Cordillera Central, Dominican Republic. In P. Mann, G. Draper, & J. F. Lewis (Eds.), *Geologic and Tectonic Development of the North America-Caribbean Plate Boundary in Hispaniola*. Geological Society of America Special Paper 262, 315–336.

Heubeck, C., Mann, E, Dolan, J., & Monechi, S. (1991). Diachronous uplift and recycling of sedimentary basins during Cenozoic tectonic transpression, northeastern Caribbean plate margin. *Sedimentary Geology*, 70: 1-32.

Hibbert, F. D., Rohling, E. J., Dutton, A., Williams, F. H., Chutcharavan, P. M., Mark, Ch. Z., & Tamisiea, E., 2016. Coral indicators of past sea-level change: A global repository of U-series dated benchmarks. *Quaternary Science Reviews*, 145, 1-56.

Jaffey, A. H., Flynn, K. F., Glendenin, L. E., Bentley, W. C., & Essling, A. M. (1971). Precision measurement of half-lives and specific activities of ^{235}U and ^{238}U. *Physical Reviews*, C 4, 1889–1906.

Kamenov, G., Perfit, M., Lewis, J., Goss A. R, Arévalo, R., & Shuster, R.D. (2011). Ancient lithospheric source for Quaternary lavas in Hispaniola. *Nature Geoscience*, 4, 554–557.

Kroehler, M. E., Mann, P., Escalona, E., & Christeson, G. L. (2011). Late Cretaceous-Miocene diachronous onset of back thrusting along the South Caribbean deformed belt and its importance for understanding processes of arc collision and crustal growth. *Tectonics*, 30 (6), 1–31.

Manaker, D. M., Calais, E., Freed, A. M., Ali, S. T., Przybylski, P., Mattioli, G., Jansma, P., Prépetit, C., & De Chabalier, J. B. (2008). Interseismic plate coupling and strain partitioning in the Northeastern Caribbean. *Geophysical Journal International*, 174, 889-903.

Mann, P., Draper, G., & Lewis, J.F. (1991a). An overview of the geologic and tectonic development of Española. In P. Mann, G. Draper & J.F. Lewis (Eds.), *Geologic and Tectonic Development of the North America-Caribbean Plate Boundary in Hispaniola*. Geological Society of America Special Paper, 262, 1-28.

Mann, P., McLaughlin, P. P., Jr., & Cooper, J.C. (1991b). Geology of the Enriquillo-Azua basins, Dominican Republic, 2. Structure and tectonics. In P. Mann, G. Draper & J.F. Lewis (Eds.), *Geologic and Tectonic Development of the North America-Caribbean Plate Boundary in Hispaniola*. Geological Society of America Special Paper, 262, 367-389.

Mann, P., Taylor, F. W., Edwards, R. L., & Ku, T. L. (1995). Actively evolving microplate formation by oblique collision and sideways motion along strike-slip faults: an example from the northeastern Caribbean plate margin. *Tectonophysics*, 246, 1-69.

Mann, P., Calais, E., Ruegg, J. C., Demets, C., Jansma, P. E., & Mattioli, G. S. (2002). Oblique collision in the northeastern Caribbean from GPS measurements and geological observations. *Tectonics*, 21(6), 1-23.

Mann, P., Rogers, R., & Gahagan, L. (2007). Overview of plate tectonic history and its unresolved tectonic problems. In J. Bundschuh, & G.E. Alvarado (Eds.), *Central America: Geology, Resources and Hazards*, v. 1. Leiden. The Netherlands, 201-237.

Mauffret, A., & Leroy, S. (1999). Neogene intraplate deformation of the Caribbean plate at the Beata Ridge, In P. Mann (Ed.), *Sedimentary Basins of the World, 4. Caribbean Basins*. Elsevier Science, N. Y. 627–669.

Mauffret, A., Leroy, S., Vila, J. M., Hallot, E., Mercier de Lepinay, B., & Duncan, R.A. (2001). Prolonged magmatic and tectonic development of the Caribbean Igneous Province revealed by a diving submersible survey. Marine Geophysical Research, 22, 17–45.

McCann, W. R., Feldman, L., & McCann, M. (2011), Catalog of felt earthquakes for Puerto Rico and neighboring islands 1492–1899 with additional information for some 20th century earthquakes. Revista Geofísica, 62, 141–293.

McLaughli, P. P., van den Bold, W.A., & Mann, P. (1991). Geology of the Azua and Enriquillo basins, Dominican Republic; 1, Neogene lithofacies, biostratigraphy, biofacies, and paleogeography. In P. Mann, G. Draper & J.F. Lewis (Eds.), Geologic and Tectonic Development of the North America-Caribbean Plate Boundary in Hispaniola. Geological Society of America Special Paper, 262, 337-366.

Mercier de Lépinay, B. (1987). L'évolution géologique de la bordure nord-caraïbe: L'exemple de la transversale del'île d'Hispaniola (Grandes Antilles). Thèse d'Etat, Université Pierre et Marie Curie, 366 p.

Mercier de Lépinay, B., Deschamps, A., Klingelhoefer, F., Mazabraud, Y., Delouis, B., Clouard, V., Hello, Y., Crozon, J., Marcaillou, B., Graindorge, D., Vallée, M., Perrot, J., Bouin, M. P., Saurel, J. M., Charvis, P., & St-Louis, M. (2011). The 2010 Haiti earthquake: A complex fault pattern constrained by seismologic and tectonic observations. *Geophysical Research Letters*, 38, L22305. https:// doi .org /10 .1029 /2011GL049799.

Müller, R. D., Cannon, J., Qin, X., Watson, R. J., Gurnis, M., Williams, S., et al. (2018). GPlates: Building a virtual Earth through deep time. *Geochemistry, Geophysics, Geosystems*, 19. doi:10.1029/2018GC007584

Ordaz, M., Cardona O., Salgado-Gálvez M. A., Bernal G., Singh K., & Zuloaga D. (2014). Probabilistic seismic hazard assessment at global level. *International Journal of Disaster Risk Reduction*. 10(B):419-427.

Ortner, H., Reiter, F., & Acs, P. (2002). Easy handling of tectonic data: the programs TectonicVB for Mac and TectonicsFP for Window. *Computers & Geosciences*, 28, 1193-1200.

Pérez-Estaún, A., Hernaiz Huerta, P. P., Lopera, E., Joubert, M., Escuder Viruete, J., Díaz de Neira, A., Monthel, J., García-Senz, J., Urien, P., Contreras, F., Bernárdez, E., Stein, G., Deschamps, I., García-Lobón, J. L., & Ayala, C. (2007). Geología de la República Dominicana: De la construcción de arco-isla a la colisión arco-continente. *Boletín Geológico y Minero*, 118, 157-174.

Pérez Valera, F. (2010). Mapa Geológico de la Hoja a E. 1:50.000 nº 6070-I (Sabana Buey). Dirección General de Minería, Santo Domingo, 96 pp. https://www.sgn.gob.do

Pindell, J., & Kennan, L. (2009). Tectonic evolution of the Gulf of Mexico, Caribbean and northern South America in the mantle reference frame: an update. In K. James, M. A. Lorente & J. Pindell (Eds.), *The geology and evolution of the region between North and South America*, Geological Society of London Special Publication, 328, 1-55.

1408 Prentice, C. S., Mann, P., Crone, A. J., Gold, R. D., Hudnut, K. W., Briggs, R. W., Koehler, R. D., &
1409 Jean, P. (2010). Seismic hazard of the Enriquillo–Plantain Garden fault in Haiti inferred from
1410 palaeoseismology. *Nature Geoscience*, 3, 789–793.

1411 Pubellier, M., Mauffret, A., Leroy, S., Vila, J.M., & Amilcar, H. (2000). Plate boundary readjustment
1412 in oblique convergence: Example of the Neogene of Hispaniola, Greater Antilles. *Tectonics*,
1413 19, 4, 630–648.

1414 Ramírez, M. I. (1995). Neotectonic structures and paleostress in the Azua region, south-central
1415 Hispaniola. Master of Science in Geology. Florida International University, 144 pp.

1416 Ranero, C. R., & von Huene, R. (2000). Subduction erosion along the Middle America convergent
1417 margin. *Nature*, 404, 748–752.

1418 Reiter, F., & Acs, P. (2000). TectonicsFP 1.6. Computer Software for Structural Geology. Operating
1419 Manual, 48 pp. [Software]. https://github.com/freiter/TectonicsFP/blob/master/Tectfp32.dsk

1420 Révillon, S., Hallot, E., Arndt, N., Chauvel, C., & Duncan, R.A. (2000). A Complex History for the
1421 Caribbean Plateau: Petrology, Geochemistry, and Geochronology of the Beata Ridge, South
1422 Hispaniola. *Journal of Geology*, 108, 641–661.

1423 Rodríguez, J., Havskov, J., Botter Sorebseb, M., & Santos, L.F. (2018). Seismotectonics of south-
1424 west Dominican Republic using recent data. *Journal of Seismology*, 22, 883–896.

1425 Rodríguez-Zurrunero, J. L. Granja-Bruña, A. Carbó-Gorosabel, A. Muñoz-Martín, J. M. Gorosabel-
1426 Araus, L. Gómez de la Peña, M. Gómez Ballesteros, A. Pazos, M. Catalán, S. Espinosa, M.
1427 Druet, P. Llanes, & ten Brink, U. (2019). Submarine morpho-structure and active processes
1428 along the North American-Caribbean plate boundary (Dominican Republic sector). *Marine*
1429 *Geology*, 407, 121-147.

1430 Russo, R.M., & Villaseñor, A. (1995). The 1946 Hispaniola earthquake and the tectonics of the
1431 North America Caribbean plate boundary, northeastern Hispaniola. *Journal Geophysical*
1432 *Research*, 100, 6265–6280

1433 Ryan, W. B. F., Carbotte, S. M. Coplan, J., O'Hara, S. Melkonian, A., Arko, R., Weissel, R.A.,
1434 Ferrini, V., Goodwillie, A., Nitsche, F., Bonczkowski, J., & Zemsky, R. (2009). Global
1435 Multi-Resolution Topography (GMRT) synthesis data set. *Geochemistry, Geophysics,*
1436 *Geosystems*, 10, Q03014, doi: 10.1029/2008GC002332

1437 Sak, P. B., Fisher, D. M., Gardner, T. W., Marshall, J. S., & LaFemina, P. C. (2009). Rough crust
1438 subduction, forearc kinematics, and Quaternary uplift rates, Costa Rican segment of the
1439 Middle American Trench. *Geological Society America Bulletin*, 121 (7-8), 992–1012.

1440 Schellmann, G., & Radtke, U. (2004). A revised morpho- and chronostratigraphy of the late and
1441 middle Pleistocene coral reef terraces on Southern Barbados (West Indies). *Earth-Science*
1442 *Reviews*, 64, 157–187.

1443 Sinton, C. W., Duncan, R. A., Storey, M., Lewis, J., & Estrada, J. J. (1998). An oceanic flood basalt
1444 province within the Caribbean plate. *Earth Planetary Science Letters*, 155, 221– 235.

1445 SISFRANCE Antilles (2009). Sismicité historique de la France Antilles-Guyane-Mer des Caraïbes.
1446 Bureau de Recherches Géologiques et Minières. Available online:
1447 https://sisfrance.irsn.fr/Antilles/

Suárez-Rodríguez, Á., Escuder-Viruete, J., & Colmenero-Hidalgo, E. (2017). La mélange de San Marcos, Cordillera Septentrional de la República Dominicana. Significado, origen y edad. *Boletín Geológico y Minero*, 128 (3), 633-656.

Symithe, S., Calais, E., de Chabalier, J. B., Robertson, R., & Higgins, M. (2015). Current block motions and strain accumulation on active faults in the Caribbean. *Journal Geophysical Research Solid Earth*, 120, 3748-3774.

Tanner, J. G., & Shepherd, J. B. (1997) Seismic hazard in Latin America and the Caribbean, Final Report. Volume I: Project Catalogue and Seismic Hazard Maps. Instituto Panamericano de Geografia y Historia (IPGH). Project n°89-0190. International Development Research Centre, Ottawa, Canada, 143 p

Takaku, J., Tadono, T., Doutsu, M., Ohgushi, F., & Kai, H. (2020). Updates of 'AW3D30' ALOS Global Digital Surface Model with Other Open Access Datasets. The International Archives of the Photogrammetry, Remote Sensing and Spatial Information Sciences, ISPRS, Vol.XLIII-B4-2020, 183–189.

Taylor, F. W., Mann, P., Bevis, M. G., Edwards, R. L., Cheng, H., Cutler, K. B., et al. (2005). Rapid forearc uplift and subsidence caused by impinging bathymetric features: Examples from the New Hebrides and Solomon arcs. Tectonics, 24, 6. https://doi.org/10.1029/2004tc001650

ten Brink, U. S., Bakun, W. H., & Flores, C. H. (2011). Historical perspective on seismic hazard to Hispaniola and the northeast Caribbean region. *Journal Geophysical Research*, 116, b12318.

Terrier-Sedan, M., & Bertil, D. (2021). Active fault characterization and seismotectonic zoning of the Hispaniola island. *Journal of Seismology*, 25, 499–520.

Tozer, B., Sandwell, D. T., Smith, W. H. F., Olson, C., Beale, J. R., & Wessel, P. (2019). Global bathymetry and topography at 15 Arc Sec: SRTM15+. *Earth and Space Science*, 6(10), 1847–1864. https://doi.org/10.1029/2019EA000658

Twiss, R. J., & Unruh, J.R. (1998). Analysis of fault slip inversions: do they constrain stress or strain rate? *Journal of Geophysical Research*, 103 (6), 12.205–12.222.

Vannucchi, P., Sak, P. B., Morgan, J. P., Ohkushi, K., & Ujiie, K. (2013). Rapid pulses of uplift, subsidence, and subduction erosion offshore Central America: Implications for building the rock record of convergent margins. *Geology*, 41, 995–998.

Vespucci, R. M. (1988). Petrology and Geochemistry of Late Cenozoic Volcanic Rocks of the Dominican Republic. PhD thesis, George Washington University. 378 pp.

Wells, D. L., & Coppersmith, K. J. (1994). New empirical relationships among magnitude, rupture length, rupture width, rupture area, and surface displacement. *Bulletin of the Seismological Society of America,* 84, 974–1002.

Witschard, M., & Dolan, J. F. (1990). Contrasting structural styles in siliciclastic and carbonate rocks of an offscraped sequence: The Peralta accretionary prism, Hispanio*la. Geological Society of America Bulletin*, 102 (6), 792–806.

References From the Supporting Information

André, A. S., Sausse J., & Lespinasse M. (2001). New approach for the quantification of paleostress magnitudes: application to the Soultz vein system (Rhine graben, France). *Tectonophysics,* 336, 215–231.

Angelier, J. & Goguel, J. (1979). Sur une method simple de determination des axes principaux des contraintes pour une population de failles. *Comptes Rendus Hebdomadaires des Seances de l'Academie des Sciences, Serie D: Sciences Naturelles*, 288 (3), 307–310.

Angelier, J. & Mechler, P. (1977). Sur une méthode graphique de recherche des contraintes principales également utiliable en tectonique et en séismologie: la méthode des dièdres driots. *Bulletin de la Société Géologique de France,* 7, 1309–1318.

Bott, M. H. P. (1959). The mechanics of oblique slip faulting. *Geological Magazine*, 96 (2), 109–117.

Montaggioni, L. F. & Braithwaite, C. J. R. (2009). *Quaternary Coral Reef Systems: History, Development Processes and Controlling Factors.* Elsevier, Amsterdam. 5, 532 pp.

Muhs, D. R., Pandolfi, J. M., Simmons, K. R. & Schumann, R. R. (2012). Sea-level history of past interglacial periods from uranium-series dating of corals, Curaçao, Leeward Antilles islands. *Quaternary Research*, 78, 157-169.

Sperner, B. & Zweigel, P. (2010). A plea for more caution in fault-slip analysis. *Tectonophysics*, 482 (1–4), 29–41.

Turner, F. J. (1953). Nature and dynamic interpretation of deformation lamellae in calcite of three marbles. *American Journal of Science*, 251, 276–298.

Woodroffe, C. D. & Webster, J. M. (2014). Coral reefs and sea-level change. *Marine Geology*, 352, 248-267.

Figure Captions

Fig. 1. Geodynamic reconstructions made with *Gplates* 2.3.0 software for arc-continent and arc-oceanic plateau collisions in northern and southern Hispaniola, respectively. Different tectonic elements are color coded and described in the key. (a) Reconstruction at 80 Ma (lower Campanian): the large white area in the present-day location of the central Caribbean represents the proto-Caribbean oceanic crust that will be subducted by the NE motion of the intra-oceanic Caribbean island-arc. Dark grey areas represent zones of thickened Caribbean oceanic plateau (CLIP; Caribbean Large Igneous Province). (b) Reconstruction at 40 Ma (middle Eocene): at this time the Caribbean island-arc collided with the southern North American continental margin and is moving eastward. The small white area adjacent to southern Hispaniola will start to subduct due to back-thrusting in the Peralta-Muertos accretionary prism. (c) Present-day: the ENE-directed convergence led to Caribbean plate subduction and Beata Ridge collision in southern central Hispaniola. The blue line represents the path of a point (blue star) on the Sierra Bahoruco in the Caribbean plate since 80

1521 Ma. *GPlates* reconstructions show that the direction of motion of the central Caribbean plate
1522 abruptly changes from northeastward to east-northeastward in the middle Eocene. This means that
1523 the direction of subduction/collision is highly oblique along the E-W-striking Peralta-Muertos
1524 deformed belt in southern Hispaniola. AVR, Aves Ridge; BR, Barbados Prism; BE, Beata
1525 Escarpement; BOFZ, Boconó Fault Zone; BOFZ, Bowin Fault Zone; BFZ, Bucaramanga fault zone;
1526 CAT, Cayman Trough; CHO, Chortis block; CGFZ, Cerro Golden Fault Zone; CR, Costa Rica; CU,
1527 Cuba; EPFZ, El Pilar Fault Zone; EPGFZ, Enriquillo-Platain Garden Fault Zone; GRB, Grenada
1528 basin; H; Hispaniola (Dominican Republic and Haiti); HP, Haiti Plateau; HE, Hess Escarpement;
1529 HB, Hispaniola Basin; LA, Lesser Antilles; MB, Maracaibo basin; MES, Mesquito terranes; MAT,
1530 Middle America Trench; MC, Mona Canyon; MP, Mona Passage; MDB, Muertos Deformed Belt;
1531 MT, Muertos Trough; MPFZ, Motaguá Polochic fault zone; NHDB, North Hispaniola Deformed
1532 Belt; NHFZ, North Hispaniola Fault Zone; NPFB, Nothern Panamá Fold Belt; OFZ, Oriente fault
1533 zone; P, Panamá; PB, Peralta Belt; PR, Puerto Rico; PRT, Puerto Rico Trench; SFZ, Septentrional
1534 Fault Zone; SCDB, South Caribbean Deformed Belt; SFB, South Florida basin; TB, Tobago basin;
1535 VDB, Venezuela Deformed Belt; VI, Virgin Islands; YUC, Yucatán block.

1536 Fig. 2. (a) Map of the northeastern margin of the Caribbean Plate showing the location of plate and
1537 microplate boundaries, as well as the main tectonic structures. The red arrow defines the movement
1538 vector of 18-20 mm/a in the direction N070ºE of the Caribbean Plate with respect to the North
1539 American Plate (mod. Mann et al., 2002). Relief in color scale has been made from the GMRT
1540 synthesis data set (Ryan et al., 2009) with *GeoMapApp* (www.geomapapp.org). The discontinuous
1541 red rectangle defines the situation of the study area in the Dominican Republic. (b) Schematic
1542 geologic map of southern Hispaniola (mod. from the SYSMIN Project; Pérez-Estaún et al., 2007).
1543 The discontinuous red line marks location of Fig. 3. (c) Geological cross-section of the study area.
1544 The location is shown in (b). Abbreviations as in Fig. 1, in addition: CFZ, Camú fault zone; HFTB;

1545 Haitian fold-and-thrust belt; OBFZ, Ocoa-Bonao-La Guacara fault zone; SFZ, Septentrional fault
1546 zone; SJPFZ, San Juan-Los Pozos fault zone; TBFZ; Trois Baies fault zone.

1547 Fig. 3. Neotectonic map of southern central Hispaniola. Shaded relief in grayscale has been made
1548 from the GMRT synthesis data set (Ryan et al., 2009) with *GeoMapApp* (www.geomapapp.org). The
1549 neotectonic structures and late Neogene and Quaternary lithostratigraphic units compiled in the map
1550 result from integrating new field data with the geologic map obtained by the SYSMIN Project in the
1551 Dominican Republic (Pérez-Estaún et al., 2007). The main neotectonic structures are: Offshore (O-
1552 OBFZ) and Southern (S-OBFZ) segments of the Ocoa-Bonao-La Guacara fault zone; Central (C-
1553 SFZ) segment of the Septentrional fault zone; Southern (S-HFZ), Central (C-HFZ) and Northern (N-
1554 HFZ) segments of Hispaniola fault zone; Southern (S-JPFZ) and Central (C-JPFZ) segments of the
1555 San Juan-Los Pozos fault zone; and Northern (N-BRFZ) and Central (C-BRFZ) segments of the
1556 Beata Ridge fault Zone. Other relevant structures are the Bahoruco fault zone (BAFZ) and the Ocoa
1557 segment of the Muertos Trust (O-MT). Abbreviations as in Fig. 1, in addition: AZ, Azua; BA,
1558 Barahona; BN, Baní; BO, Bonao; CO, Constanza; JA, Jánico; JB, Jarabacoa; LV, La Vega; MA,
1559 Mao; MN, Manabao; RA, Rancho Arriba; SB, Sabana Buey; SC, Santiago de los Caballeros; SJ, San
1560 José de Ocoa; SQ, Sábana Quéliz; VA, Villa Altagracia.

1561 Fig. 4. (a) Bouguer gravity anomaly map of southern central Hispaniola showing major tectonic
1562 features delineated by sharp gravity gradients (source of gravity data: https://www.nga.mil). Areas of
1563 exposed or shallow igneous and metamorphic basement of Cretaceous age in the northern Cordillera
1564 Central and Sierra Bahoruco show higher anomalies (red to yellow tones), whereas areas with high
1565 sediment accumulation in the Cibao, San Juan and Azua basins are expressed by low anomalies (dark
1566 to light blue tones). (b) Reduced to the magnetic pole map showing major lithologic and tectonic
1567 features of southern central Hispaniola (mod. from García Lobón & Rey Moral, 2004; Ayala et al.,
1568 (2017). The reduction to the pole of the whole magnetic field improves the spatial position of

1569 anomalies that help to define areas with long and short wavelengths, regional trends and tectonic
1570 boundaries between magnetic provinces. See explanation in the text.

1571 Fig. 5. Structural analysis of the Peralta Belt. (a) Structural map of the eastern Peralta Belt in
1572 southern central Hispaniola (see location in Fig. 3), showing the tectonic domains, main Quaternary
1573 lithostratigraphic units, neotectonic structures, and sites of fault-slip data measurements. OBFZ,
1574 Ocoa-Bonao-La Guacara fault zone; SJ, San José de Ocoa intramountain basin; RA, Rancho Arriba
1575 intramountain basin. (b) Stereoplots of the non-coaxial Sp-Lp fabric produced by syn-sedimentary
1576 deformation during the upper Eocene in the Peralta and Ocoa Groups. (c) Field aspect of the syn-
1577 sedimentary deformation developed heterogeneously in the turbidites of the Ocoa Group. (d) Zone of
1578 stratal disruption in the Ocoa Group, characterized by boudinage of sandstone beds, tight to isoclinal
1579 folds with rootless limbs, and a pervasive scary clay fabric (Sp) in mudstone interbeds. (e) Detail of
1580 the boudinaged sandstone beds and the S-C structures in the mudstones.

1581 Fig. 6. Structural analysis of the Peralta Belt. (a) Stereoplots of the principal stress axes obtained
1582 from inversion of fault-slip data. n, number of data. Inversion methods: PTM, P–T Method; RDM,
1583 Right Dihedra Method; DIM (Direct Inversion Method); and NDA, Numerical Dynamic Analysis
1584 Method. (b) Asymmetric D1 folds of SW vergence, associated with mid-dip angle reverse faults,
1585 developed in the limestones of the lower Miocene Sobrerito Formation. (c) D1 reverse faults cutting
1586 the block-in-matrix fabric (Sp) and calcite veins in the Peralta Group.

1587 Fig. 7. Structural analysis of the Peralta Belt. (a) Stereoplots of the principal stress-axes obtained
1588 from inversion of fault-slip data. (b) Structural map of the northern Ocoa Bay in southern central
1589 Hispaniola (see location in Fig. 3), showing main lithostratigraphic units, neotectonic structures, and
1590 sites of fault-slip data measurements. (c) Geological cross-section of the frontal part of the Peralta
1591 Belt. (d, e) Field aspect of the Loma Vieja frontal thrust (site 21JE123, see location in the cross-
1592 section), where the lower to middle Miocene limestones of the Sobrerito Formation overthrust the

1593 conglomerates of the late Pliocene to lower Pleistocene Arroyo Seco Formation. Acronyms as in Fig.
1594 3.

1595 Fig. 8. Structural analysis in the Loma Vigia sector of the Ocoa Bay. (a) Stereoplots of the principal
1596 stress axes obtained from inversion of fault-slip data. (b) D1 fold and reverse fault truncated by D3
1597 normal faults, dragging the limestone layers in the hanging-wall block to the SW (site 21JE120). (c,
1598 d) Limestone beds of the Sombrerito Formation displaced by a system of ENE to E-striking normal
1599 faults along whose planes intrude locally mafic magmas (site 21JE113).

1600 Fig. 9. Structural analysis in the Sierra Martín García. (a) Stereoplots of the principal stress axes
1601 obtained from inversion of fault-slip data. (b) Structural map of the eastern Sierra Martín García in
1602 southern central Hispaniola (see location in Fig. 3), showing main lithostratigraphic units,
1603 neotectonic structures, and sites of fault-slip data measurements. (c) Stratigraphic logs in Cañada
1604 Arenazo and Playa Caobita sites. (d) Aspect of the bands of fault-gouge and fine crush breccia
1605 several tens of meters thick associated with the strike-slip D2 deformation. View width is 40 m. (e)
1606 D3 normal faults deforming the alluvial fans deposits of Late Pleistocene to Holocene age?. View
1607 width is 18 m. (f) Coral-reef terrace of Late Pleistocene boundary age (MIS 5c) deformed by D3
1608 normal faults. (g) Field appearance of the calcite fill in the planes of the D3 extensional faults that
1609 deform the coral terrace. Gm, matrix-supported, muddy-sandy conglomerate; Gp, clast-supported,
1610 sandy conglomerate; Sc, medium-to-thick bedded coarse-grained sandstone and
1611 microconglomerates; Sm, thin-bedded, medium-to-fine-grained sandstone; Sf, fine-grained
1612 sandstone, siltstone and laminated mudstone; Ms, massive variocolored mudstone; Ls, coral reef
1613 limestone.

1614 Fig. 10. Structural analysis in northeast Sierra Bahoruco. (a) Stereoplots of the principal stress axes
1615 obtained from inversion of fault-slip data. (b) Geological cross-section of the Playa Azul site (see
1616 location in Fig. 3). (c) Panoramic view of the geological cross-section outcrop. (d) Field relationships

of the limestones of the Sombrerito Formation, coral-reef terrace of Middle to Late Pleistocene boundary age (MIS 5e stage) and gravels and red mudstones of the alluvial fan faulted by D2 strike-slip faults. (e) Field aspect of the gravels and red mudstones of the alluvial fan faulted by D3 extensional faults.

Fig. 11. Structural analysis in the Sierra Martín García. (a) Stereoplots of the principal stress axes obtained from inversion of fault-slip data. (b) Structural map of the southwestern Sierra Martín García (see location in Fig. 3), showing main lithostratigraphic units, neotectonic structures, and sites of fault-slip data measurements. (c) WNW-trending and SW-verging asymmetric D1 folds developed in the the marls and gypsum beds of the upper Pliocene La Salina Formation. (d) SW-verging asymmetric D1 folds associated with mid-dip angle reverse faults inclined to the NE developed in the gypsum deposits. The asymmetry of D1 folds and mesoscopic S-C structures establish a top-to-the-SW reverse movement. (e) Field relationships of superposition of D3 normal fault striations (e2) over D2 strike-slip striations (e1) deforming stratified gypsum beds (S0). (f) Accumulation of *Diploria* sp. forming the reef-platform facies of a coral terrace grown during the MIS 5e stage that fossilizes the D1 frontal thrust of the Sierra Martín García.

Fig. 12. Structural analysis in the San José de Ocoa basin. (a) Stereoplots of the principal stress axes obtained from inversion of fault-slip data. (b) Folded and faulted mudstones of the Numero Formation juxtaposed to tilted and faulted San José de Ocoa basin deposits through subvertical oblique reverse right-lateral D2 faults of the eastern branch of the S-OBFZ segment. (c) Low-pitch angle striations developed in subvertical fault planes subparallel to the S-OBFZ segment deforming the volcanic rocks of the Tireo Group. (d) Brecciated damage fault zone with low-pitch angle striations developed in subvertical D2 fault planes sub-parallel to the S-OBFZ segment. (e) Field overlapping relationships between low-pitch angle strike-slip striaes deformed by dip-slip normal striaes in the same fault plane, establishing a temporal order between D2 and D3 deformations.

Fig. 13. Structural analysis of the extensional D3 deformation in the Cordillera Central. (a) Stereoplots of the principal stress-axes obtained from inversion of fault-slip data. (b) Map of distribution of fossil coral reef terraces of the MIS 5e/5c and 1 stages, as well as the area affected by the D3b extensional event. See explanation in text. Shaded relief as in Fig.3.

Fig. 14. Structural analysis in the Cordillera Central. (a) Stereoplots of the principal stress-axes obtained from inversion of fault-slip data. (b) Late Cretaceous green tuffs of the Tireo Group imbricated by WSW-directed D1 thrusts. (c) Detail of D3 extensional faults overlaping D1 thrusts in the green tuffs. (d) Panoramic view of Constanza mountainous area showing a D1 macrostructure of NW-striking thrusts built up on late Cretaceous volcano-plutonic rocks overthrusting the sedimentary fill of a Quaternary intramountaneous basin. Note the development of perched valleys and triangular facets in the hanging-wall block. (e) Detail of the striae associated to the development of a D2 sinistral strike-slip fault in late Cretaceous tonalitic rocks.

Fig. 15. (a) Stereoplots of the principal stress-axes obtained from fault-slip data inversion grouped by deformation events and (b) their classification according to its kinematic regime (see Supporting Information S6). The orientation of σ_1 has been restored at sites that have undergone a post-D1 rotation. Contours in stereoplots at 1.0, 5.0, 10.0, 15.0, 20.0 and 25.0%. Computed mean stress axes for each deformation event are expressed in % and trend/plunge angles.

Fig. 16. Neotectonic diagrams showing the evolution of the Quaternary stress regime in southern central Hispaniola set up for (a) D1 reverse, (b) D2 strike-slip, and (c) D3 extensional events (Table 1). Maximum horizontal stress axis trends were derived from fault-slip data inversion. Shaded relief in grayscale has been made as in Fig. 3, indicating the overlay colour different geological domains: green, the Cretaceous basement of the Cordillera Central; pink, the middle Eocene-lower Miocene Peralta fold-and-thrust belt and the overlying uplifted forearc basin; yellow, the Tertiary limestones of the Sierras de Neiba, Martín García y Bahoruco; and pale blue, the Neogene San Juan-Azua

1665 Basin. Vectors of GPS velocities relative to the Caribbean plate at stations located in the study area
1666 are from Symithe et al. (2015), Calais et al. (2016) and UNAVCO (https://coconet.unavco.org).
1667 Acronyms as in Fig. 3. See text for explanation.

1668 Fig. 17. Result of the probabilistic seismic hazard modeling in southern central Hispaniola, as well as
1669 adjacent offshore sectors of the Ocoa Bay, expressed as iso-PGA (Peak Ground Acceleration) zones
1670 (in cm/s^2) for a return period of 475 years (i.e., an exceedance probability of 10% in 50 years). The
1671 modelled area is the same of Fig. 3 and framed by a discontinuous red box in Fig. 2. Figure also
1672 includes the trace of the main seismogenic structures described in Table 2. MDT. Shaded relief and
1673 acronyms as in Fig. 3. See text for explanation.

Figure1.

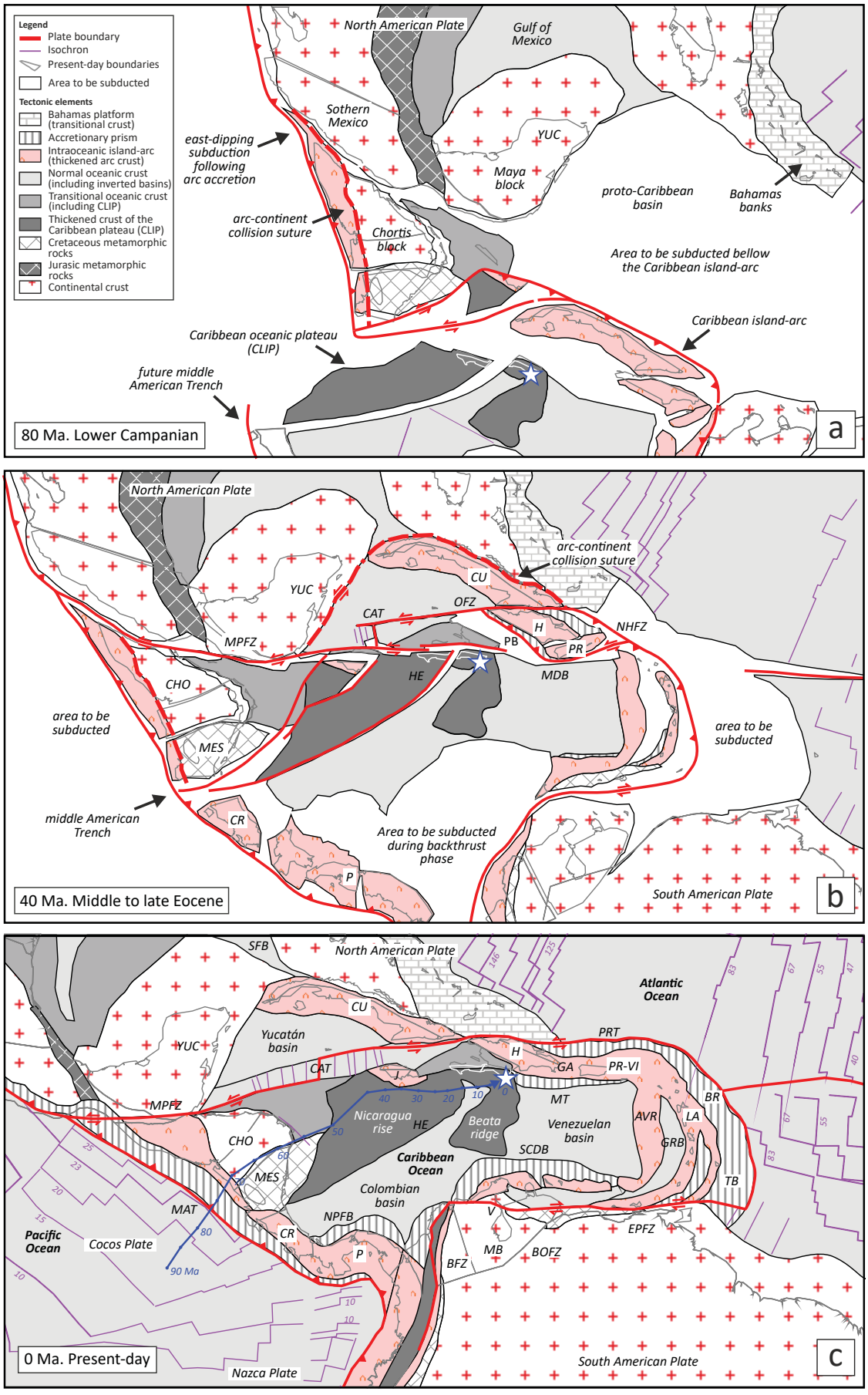
Legend
Plate boundary
Isochron
Present-day boundaries
Area to be subducted
Tectonic elements
Bahamas platform (transitional crust)
Accretionary prism
Intraoceanic island-arc (thickened arc crust)
Normal oceanic crust (including inverted basins)
Transitional oceanic crust (including CLIP)
Thickened crust of the Caribbean plateau (CLIP)
Cretaceous metamorphic rocks
Jurasic metamorphic rocks
Continental crust
North American Plate
Gulf of Mexico
Sothern Mexico
east-dipping subduction following arc accretion
YUC
Maya block
proto-Caribbean basin
Bahamas banks
arc-continent collision suture
Chortis block
Area to be subducted bellow the Caribbean island-arc
Caribbean island-arc
Caribbean oceanic plateau (CLIP)
future middle American Trench
80 Ma. Lower Campanian
a
North American Plate
arc-continent collision suture
CU
YUC
OFZ
CAT
H
NHFZ
MPFZ
PB
PR
HE
MDB
CHO
area to be subducted
area to be subducted
MES
middle American Trench
CR
Area to be subducted during backthrust phase
P
South American Plate
40 Ma. Middle to late Eocene
b
SFB
North American Plate
Atlantic Ocean
CU
Yucatán basin
PRT
YUC
H
CAT
GA
PR-VI
MPFZ
MT
BR
Nicaragua rise
HE
Beata ridge
AVR
LA
Venezuelan basin
CHO
GRB
SCDB
Caribbean Ocean
MES
TB
Colombian basin
MAT
V
NPFB
EPFZ
Pacific Ocean
Cocos Plate
CR
MB
BOFZ
P
BFZ
90 Ma
0 Ma. Present-day
Nazca Plate
South American Plate
c

Figure2.

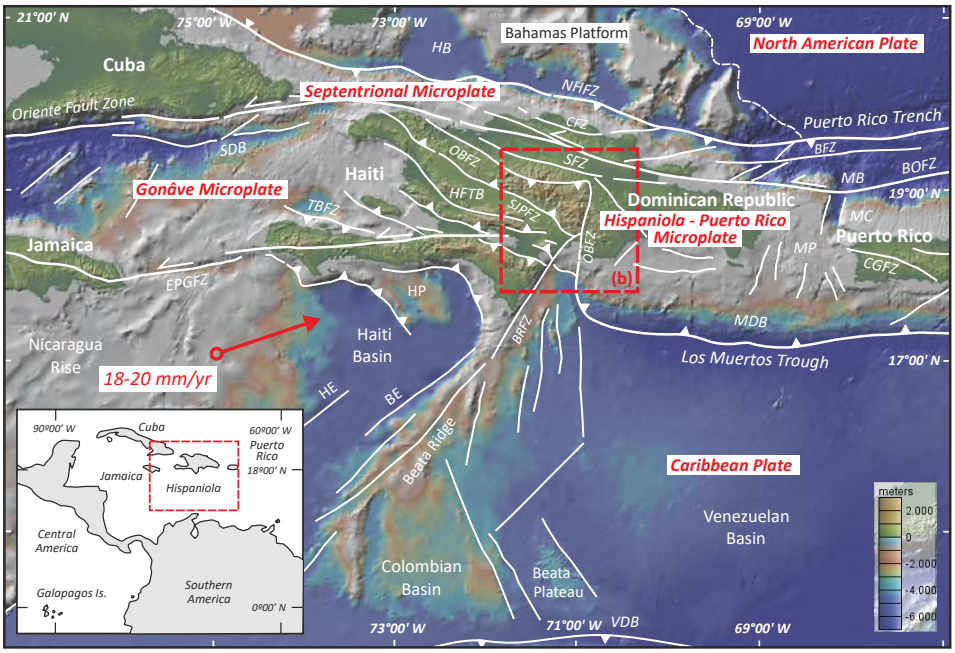

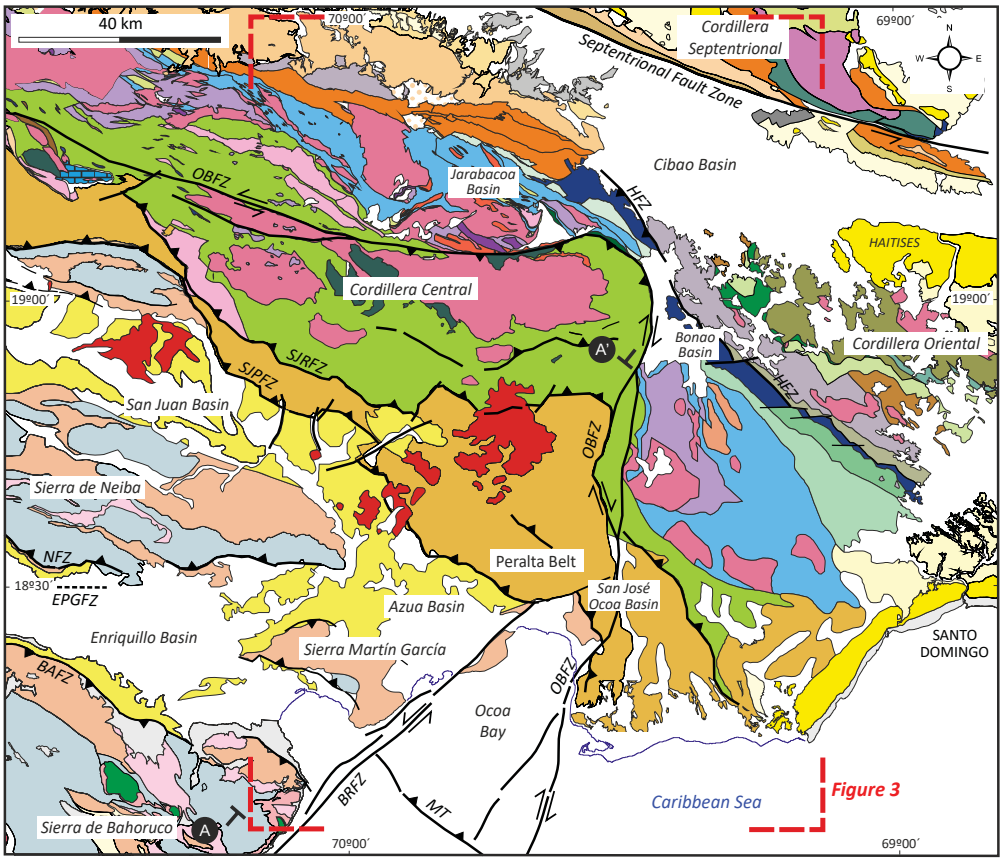

b

QUATERNARY
- Undifferenciated deposits
- Alluvial fan deposits
- Volcanic rocks

CIBAO, SAN JUAN-AZUA AND ENRIQUILLO BASINS
- Yaque del Norte deltaic deposits. Holocene
- Sedimentary rocks. Mioc.-Pleistocene
- Sedimentary rocks. Eocene-Oligocene

SIERRAS NEIBA, MARTÍN GARCÍA AND BAHORUCO
- Sombrerito Fm. Miocene
- El Aguacate Volcanosedimentary Complex. Early-Middle Eocene
- Neiba Fm. Eocene-Early Miocene.
- Dumisseau Fm. Late Cretaceous

CORDILLERA CENTRAL
- Haitises, Cevicos and Yanigua Fm. Late Miocene-Pliocene
- Peralta and Río Ocoa Belts. Late Cretaceous-Pliocene
- Don Juan Fm. Eocene
- Tonalite and Diorite
- Gabbro and Gabbronorite
- Foliated Tonalite
- Las Lagunas Fm. Late Cretaceous
- Pelona-Duarte Fm. Late Cretaceous
- Tireo Group. Late Cretaceous
- Peralvillo Sur Fm. Late Cretaceous
- Siete Cabezas Fm. Late Cretaceous
- Hatillo Limestone. Apt.-Albian
- Peralvillo Norte Fm. Early Cretaceous
- Los Ranchos Fm. Early Cretaceous
- Maimón Schists. Early Cretaceous
- Río Verde Complex. Early Cretaceous
- Duarte Complex. Early Cretaceous
- Loma Caribe Peridotite

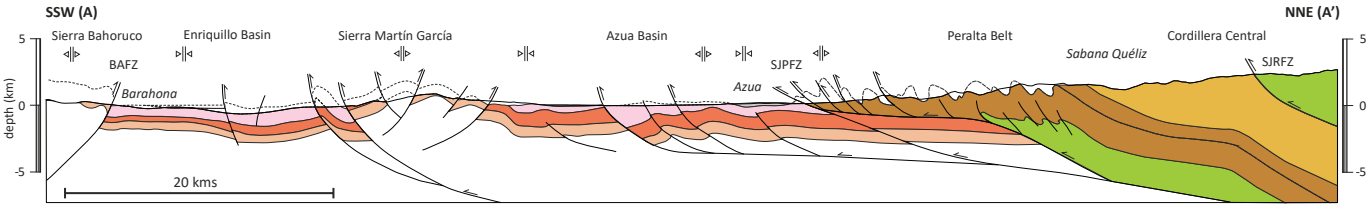

c

SAN JUAN, AZUA AND ENRIQUILLO BASINS
- Alluvial, colluvial and deltaic deposits. Holocene
- Sedimentary rocks. Miocene-Pleistocene
- Arroyo Blanco-Arroyo Seco Fms. Pliocene-Pleistocene
- Trinchera-Quita Coraza Fms. Neogene
- Sombrerito Fm. Miocene

PERALTA BELT
- Río Ocoa Group. Late Eocene-Miocene
- Peralta fold-and-thrust belt. Late Cretaceous-Middle Eocene

CORDILLERA CENTRAL
- Tireo Group. Late Cretaceous

- Anticline
- Sincline

Figure3.

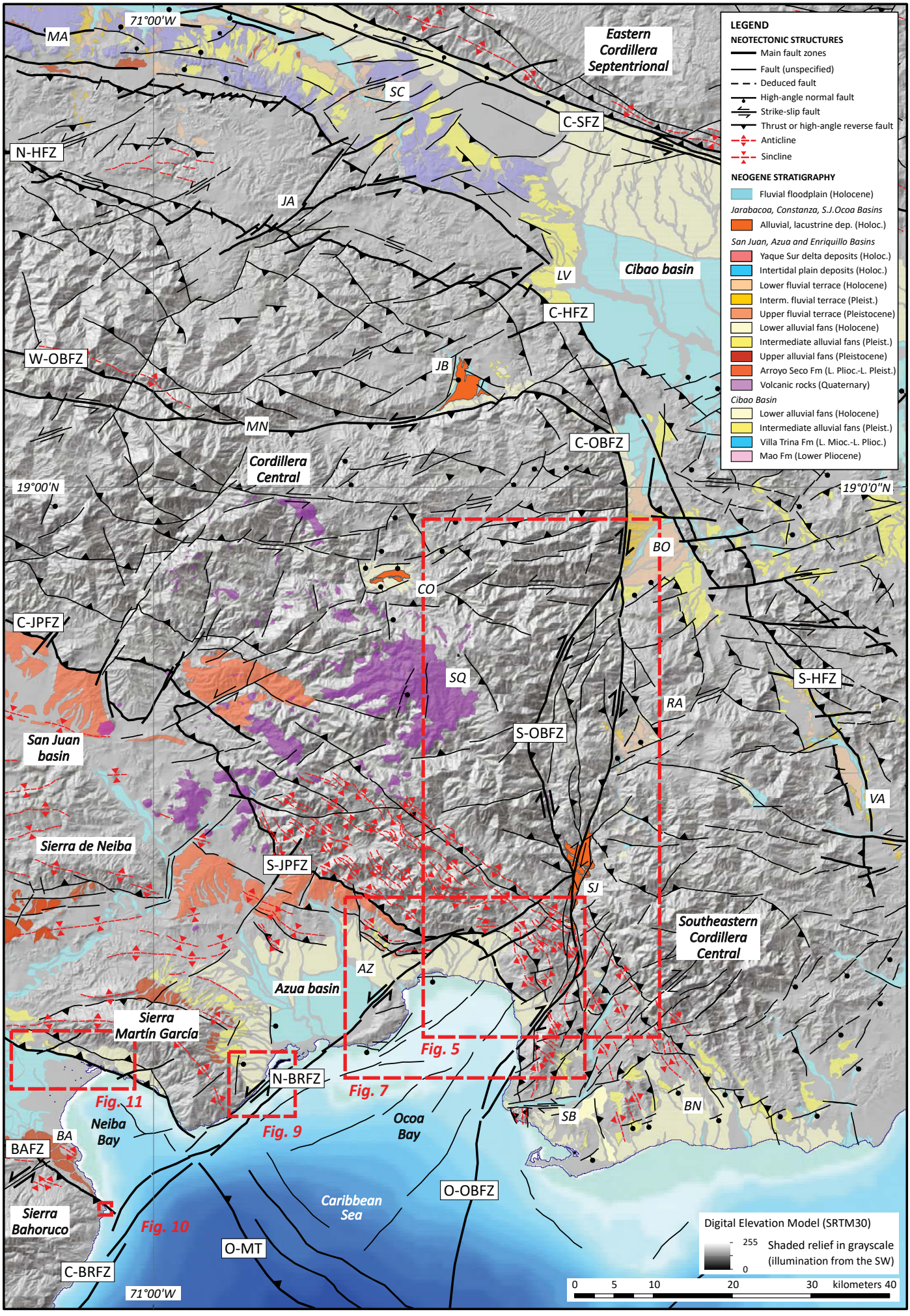
LEGEND
NEOTECTONIC STRUCTURES
Main fault zones
Fault (unspecified)
Deduced fault
High-angle normal fault
Strike-slip fault
Thrust or high-angle reverse fault
Anticline
Sincline
NEOGENE STRATIGRAPHY
Fluvial floodplain (Holocene)
Jarabacoa, Constanza, S.J.Ocoa Basins
Alluvial, lacustrine dep. (Holoc.)
San Juan, Azua and Enriquillo Basins
Yaque Sur delta deposits (Holoc.)
Intertidal plain deposits (Holoc.)
Lower fluvial terrace (Holocene)
Interm. fluvial terrace (Pleist.)
Upper fluvial terrace (Pleistocene)
Lower alluvial fans (Holocene)
Intermediate alluvial fans (Pleist.)
Upper alluvial fans (Pleistocene)
Arroyo Seco Fm (L. Plioc.-L. Pleist.)
Volcanic rocks (Quaternary)
Cibao Basin
Lower alluvial fans (Holocene)
Intermediate alluvial fans (Pleist.)
Villa Trina Fm (L. Mioc.-L. Plioc.)
Mao Fm (Lower Pliocene)
71°00'W
19°00'N
19°0'0"N
MA
SC
JA
LV
JB
MN
CO
SQ
BO
RA
VA
SJ
AZ
SB
BN
BA
Eastern Cordillera Septentrional
Cibao basin
Cordillera Central
San Juan basin
Sierra de Neiba
Azua basin
Sierra Martín García
Neiba Bay
Ocoa Bay
Caribbean Sea
Sierra Bahoruco
Southeastern Cordillera Central
C-SFZ
N-HFZ
C-HFZ
W-OBFZ
C-OBFZ
C-JPFZ
S-HFZ
S-OBFZ
S-JPFZ
N-BRFZ
BAFZ
O-OBFZ
O-MT
C-BRFZ
Fig. 5
Fig. 7
Fig. 9
Fig. 10
Fig. 11
Digital Elevation Model (SRTM30)
255
0
Shaded relief in grayscale
(illumination from the SW)
0 5 10 20 30 kilometers 40

Figure4.

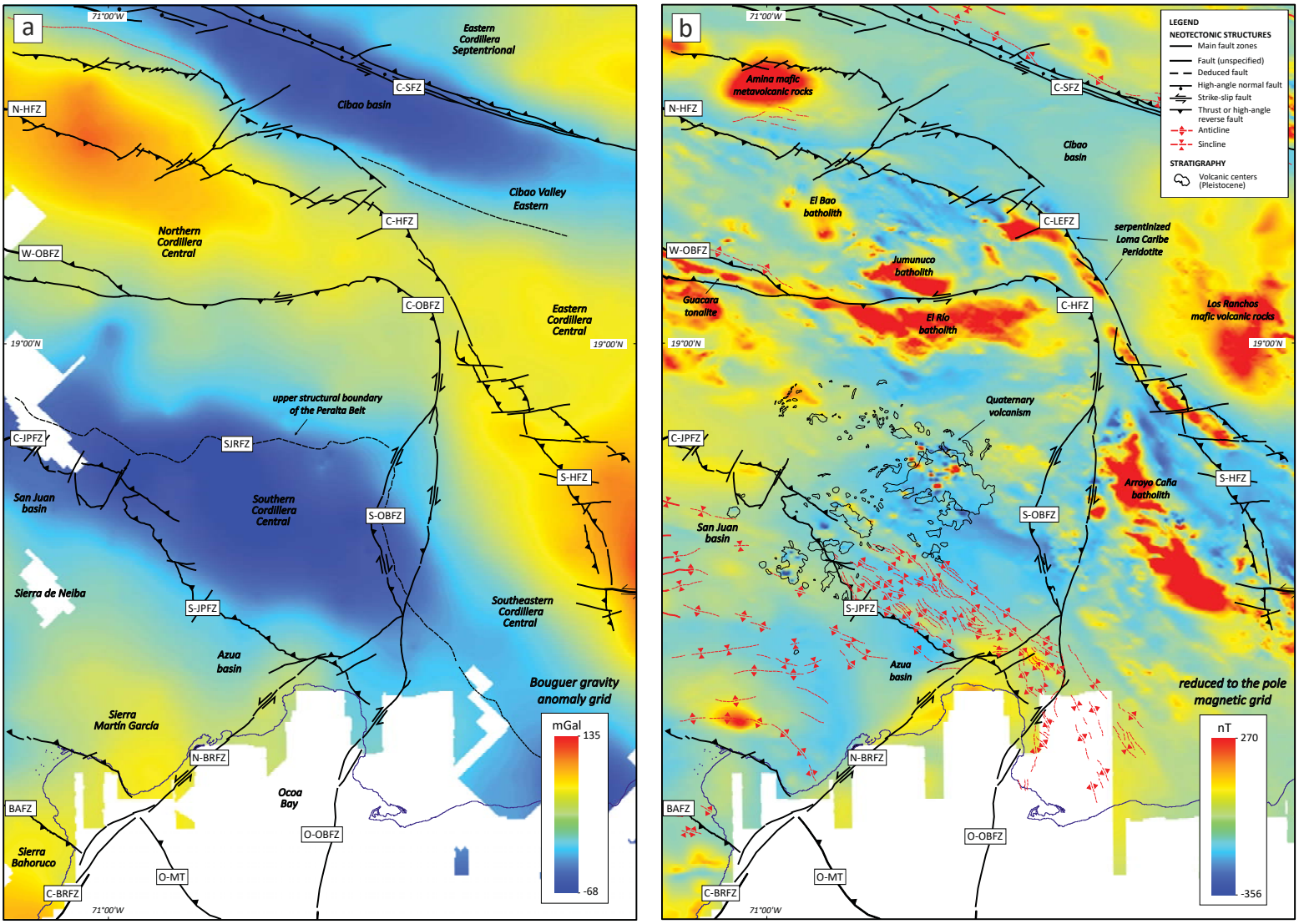
a
71°00'W
Eastern Cordillera Septentrional
C-SFZ
Cibao basin
N-HFZ
Cibao Valley Eastern
C-HFZ
Northern Cordillera Central
W-OBFZ
C-OBFZ
Eastern Cordillera Central
19°00'N
upper structural boundary of the Peralta Belt
C-JPFZ
SJRFZ
S-HFZ
San Juan basin
Southern Cordillera Central
S-OBFZ
Sierra de Neiba
S-JPFZ
Southeastern Cordillera Central
Azua basin
Bouguer gravity anomaly grid
mGal
135
-68
Sierra Martín García
N-BRFZ
Ocoa Bay
BAFZ
O-OBFZ
Sierra Bahoruco
O-MT
C-BRFZ
71°00'W
b
71°00'W
Amina mafic metavolcanic rocks
C-SFZ
N-HFZ
Cibao basin
El Bao batholith
C-LEFZ
serpentinized Loma Caribe Peridotite
W-OBFZ
Jumunuco batholith
Guacara tonalite
C-HFZ
El Río batholith
Los Ranchos mafic volcanic rocks
19°00'N
Quaternary volcanism
C-JPFZ
S-HFZ
Arroyo Caña batholith
S-OBFZ
San Juan basin
S-JPFZ
Azua basin
reduced to the pole magnetic grid
nT
270
-356
N-BRFZ
BAFZ
O-OBFZ
O-MT
C-BRFZ
71°00'W
LEGEND
NEOTECTONIC STRUCTURES
Main fault zones
Fault (unspecified)
Deduced fault
High-angle normal fault
Strike-slip fault
Thrust or high-angle reverse fault
Anticline
Sincline
STRATIGRAPHY
Volcanic centers (Pleistocene)

Figure5.

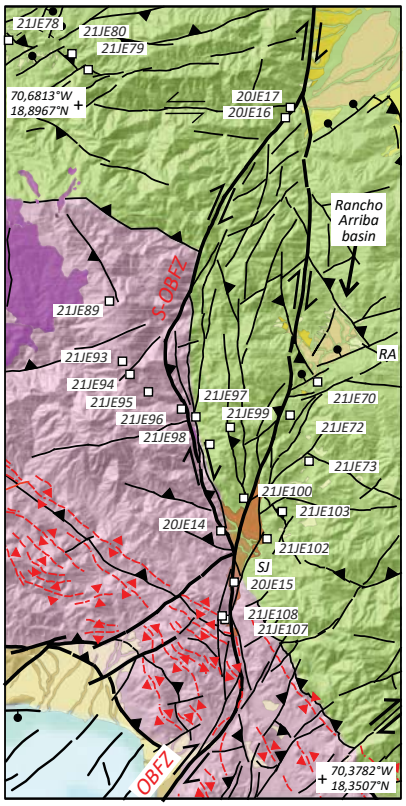
21JE78
21JE80
21JE79
70,6813°W
18,8967°N
20JE17
20JE16
Rancho Arriba basin
SJ OBFZ
21JE89
21JE93
21JE94
21JE95
21JE96
21JE98
21JE97
21JE99
RA
21JE70
21JE72
21JE73
21JE100
21JE103
20JE14
21JE102
SJ
20JE15
21JE108
21JE107
OBFZ
70,3782°W
18,3507°N

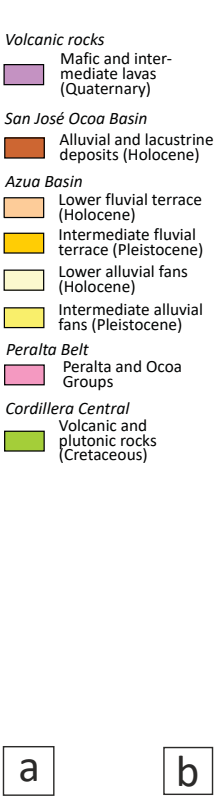
Volcanic rocks
Mafic and inter-mediate lavas (Quaternary)
San José Ocoa Basin
Alluvial and lacustrine deposits (Holocene)
Azua Basin
Lower fluvial terrace (Holocene)
Intermediate fluvial terrace (Pleistocene)
Lower alluvial fans (Holocene)
Intermediate alluvial fans (Pleistocene)
Peralta Belt
Peralta and Ocoa Groups
Cordillera Central
Volcanic and plutonic rocks (Cretaceous)

a

b

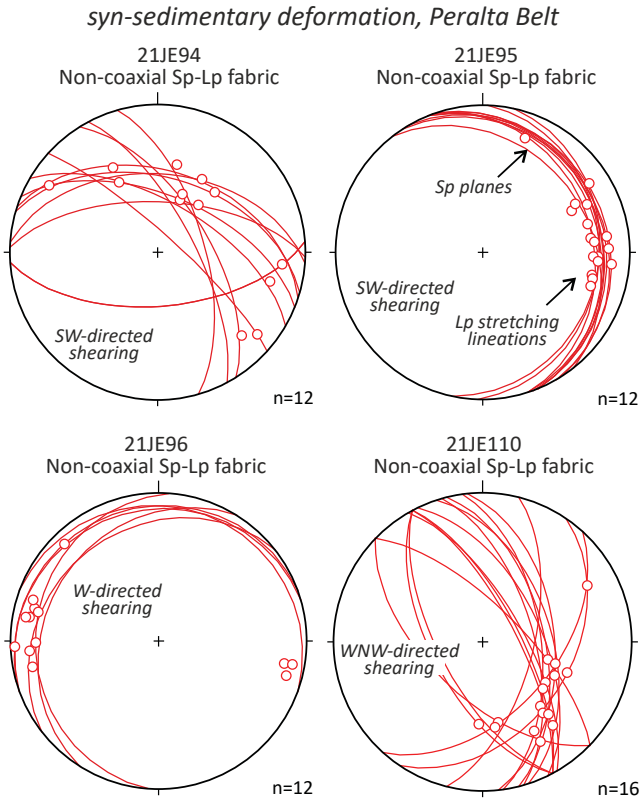
syn-sedimentary deformation, Peralta Belt
21JE94
Non-coaxial Sp-Lp fabric
SW-directed shearing
n=12
21JE95
Non-coaxial Sp-Lp fabric
Sp planes
SW-directed shearing
Lp stretching lineations
n=12
21JE96
Non-coaxial Sp-Lp fabric
W-directed shearing
n=12
21JE110
Non-coaxial Sp-Lp fabric
WNW-directed shearing
n=16


SW
NE
asymmetrical pich-and-swell structures
zones of intense stratal disruption
lense of undeformed bedding
boudinaged sandstone beds in lozenged blocks
c
21JE95

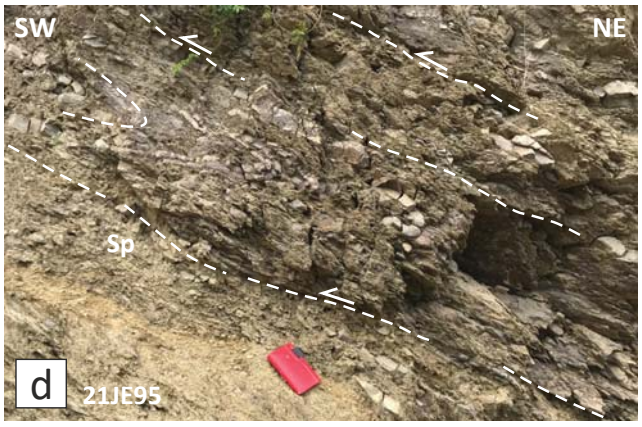
SW
NE
Sp
d
21JE95


SW
NE
Sp
C
S
e

Figure6.

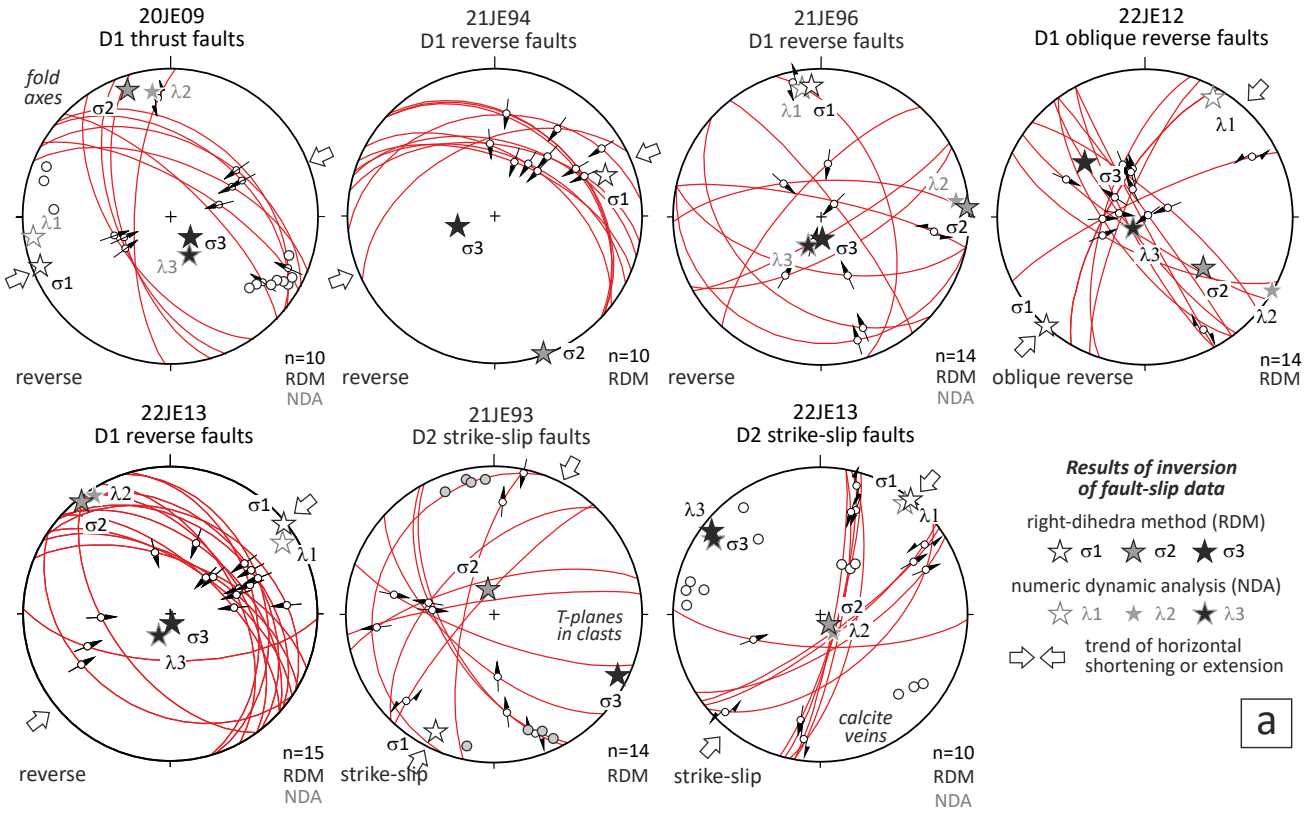
20JE09
D1 thrust faults
fold axes
σ2
λ2
λ1
σ3
λ3
σ1
reverse
n=10
RDM
NDA
21JE94
D1 reverse faults
σ1
σ3
σ2
reverse
n=10
RDM
21JE96
D1 reverse faults
λ1
σ1
λ2
σ2
σ3
λ3
reverse
n=14
RDM
NDA
22JE12
D1 oblique reverse faults
λ1
σ3
λ3
σ2
σ1
λ2
oblique reverse
n=14
RDM
22JE13
D1 reverse faults
σ1
λ2
σ2
λ1
σ3
λ3
reverse
n=15
RDM
NDA
21JE93
D2 strike-slip faults
σ2
T-planes in clasts
σ3
σ1
strike-slip
n=14
RDM
22JE13
D2 strike-slip faults
σ1
λ3
σ3
λ1
σ2
λ2
calcite veins
strike-slip
n=10
RDM
NDA
Results of inversion of fault-slip data
right-dihedra method (RDM)
σ1 σ2 σ3
numeric dynamic analysis (NDA)
λ1 λ2 λ3
trend of horizontal shortening or extension
a

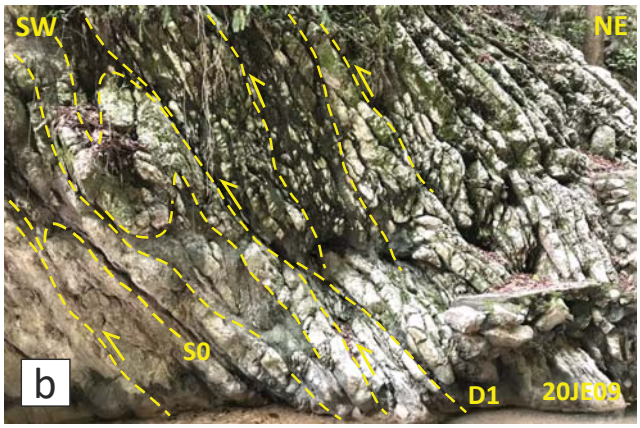
SW
NE
S0
D1
20JE09
b

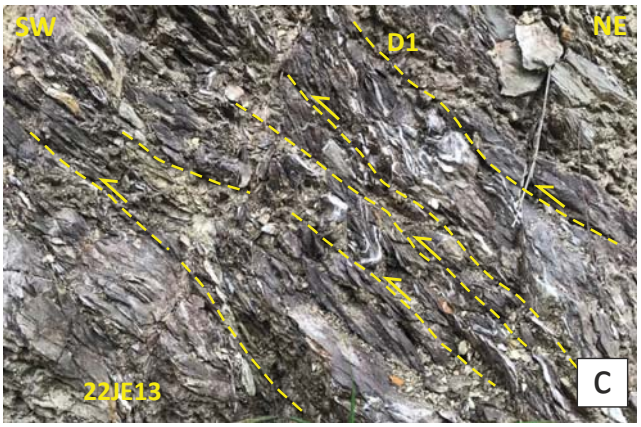
SW
D1
NE
22JE13
c

Figure7.

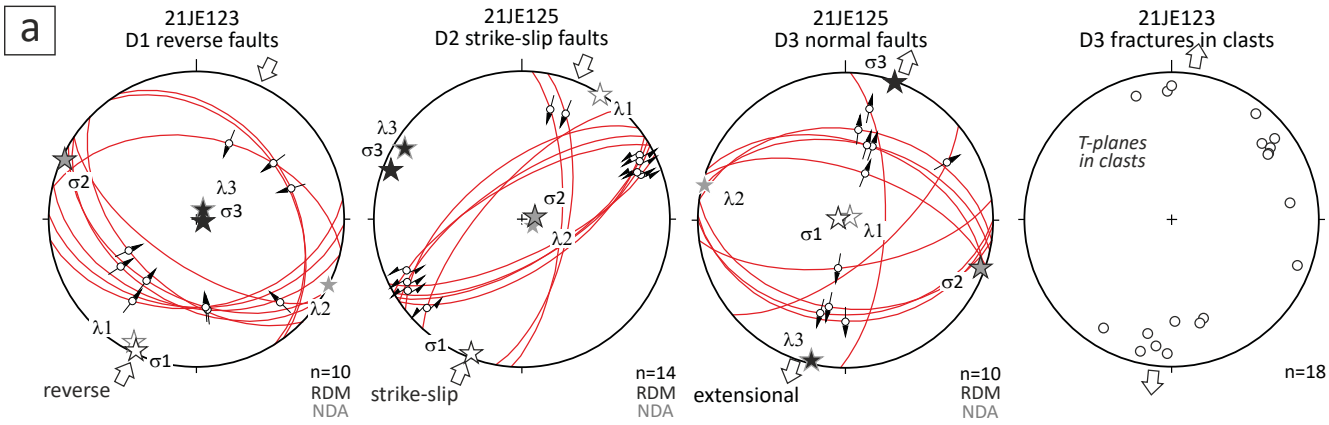

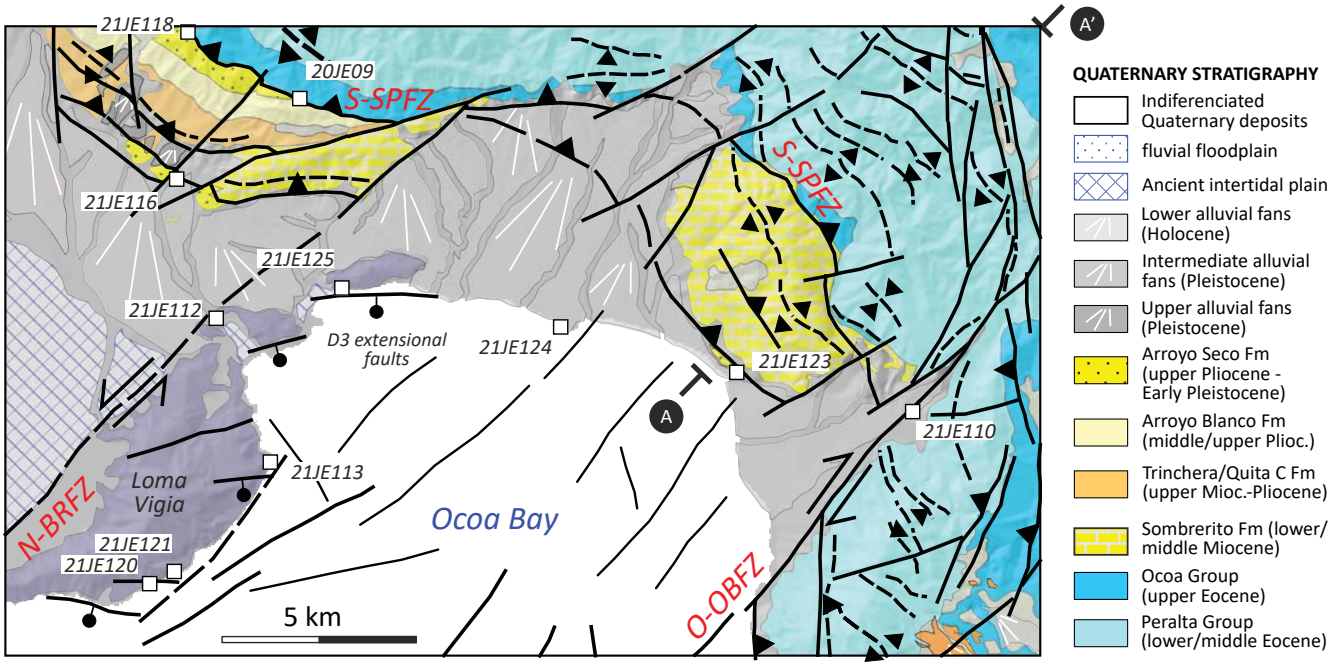

STRUCTURES

Fault (unspecified) — Deduced fault — High-angle normal fault — Strike-slip fault — Thrust or high-angle reverse fault — Anticline — Sincline

b

c

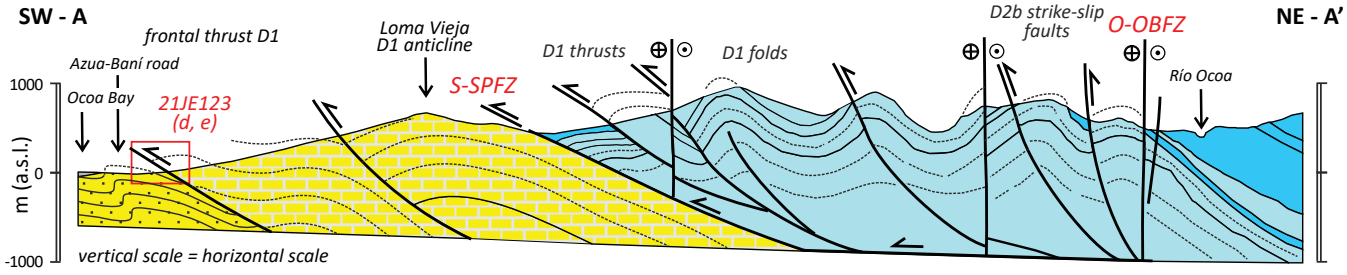

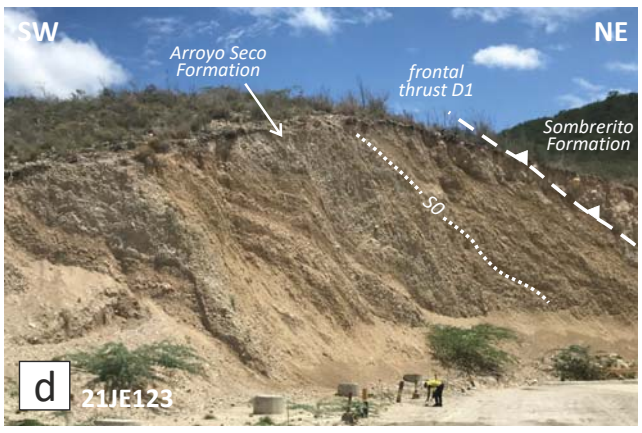

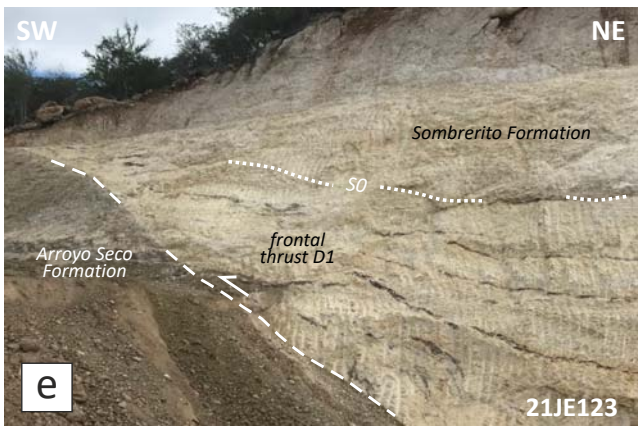

Figure8.

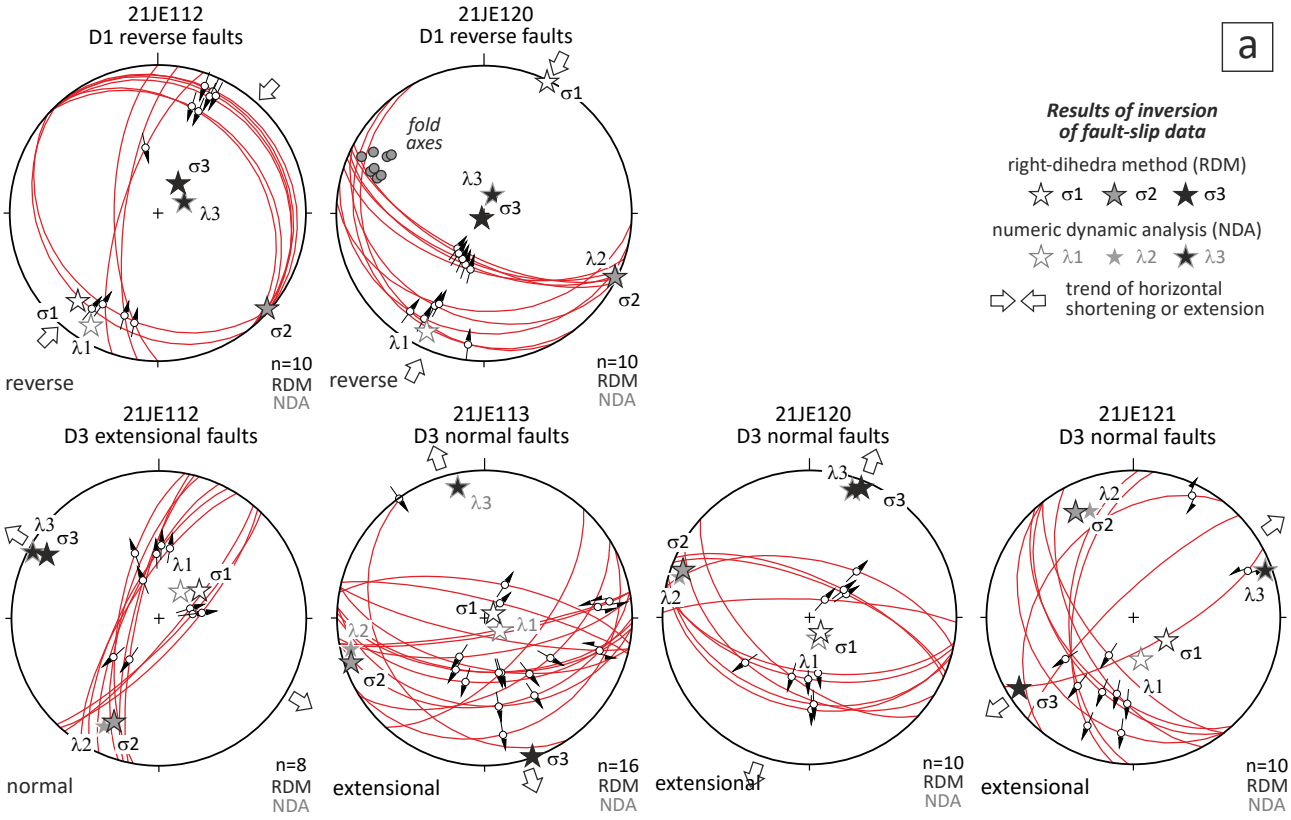
a
Results of inversion of fault-slip data
right-dihedra method (RDM)
σ1 σ2 σ3
numeric dynamic analysis (NDA)
λ1 λ2 λ3
trend of horizontal shortening or extension
21JE112
D1 reverse faults
reverse
n=10
RDM
NDA
21JE120
D1 reverse faults
fold axes
reverse
n=10
RDM
NDA
21JE112
D3 extensional faults
normal
n=8
RDM
NDA
21JE113
D3 normal faults
extensional
n=16
RDM
NDA
21JE120
D3 normal faults
extensional
n=10
RDM
NDA
21JE121
D3 normal faults
extensional
n=10
RDM
NDA

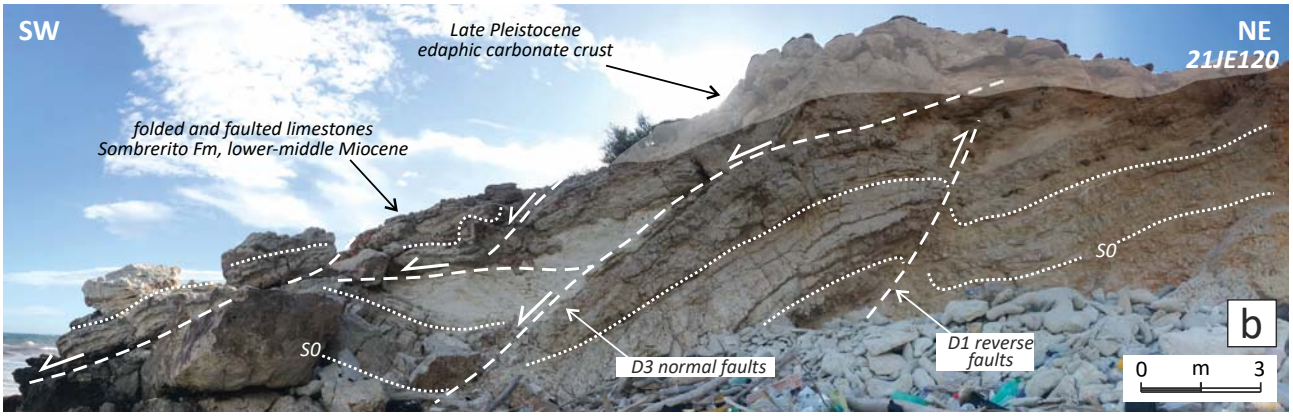
SW
NE
21JE120
Late Pleistocene edaphic carbonate crust
folded and faulted limestones Sombrerito Fm, lower-middle Miocene
S0
S0
D3 normal faults
D1 reverse faults
b
0 m 3


SW
NE
D3 normal faults
c
21JE113


SW
NE
21JE113
d
syn-D3 magmas
D3 normal faults

Figure9.

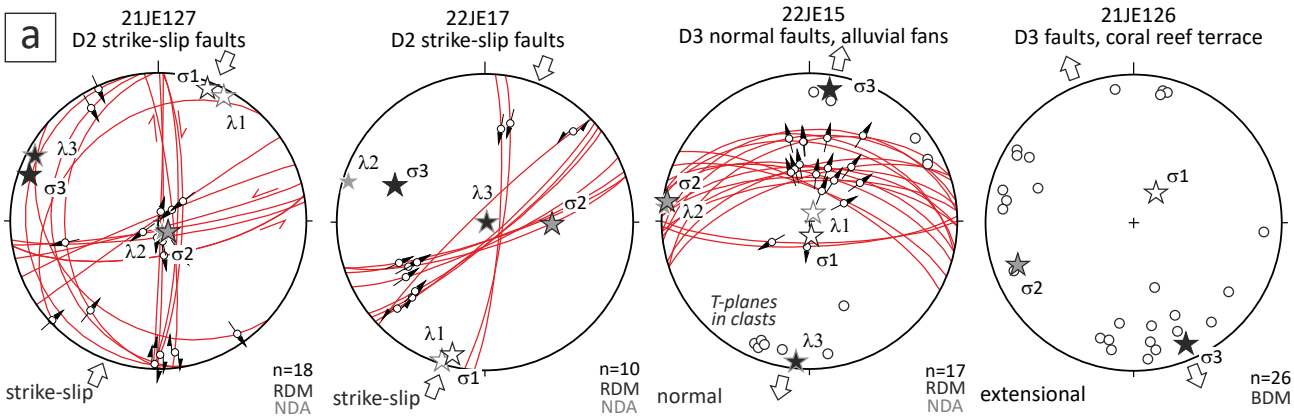
a
21JE127
D2 strike-slip faults
σ1
λ1
λ3
σ3
λ2
σ2
strike-slip
n=18
RDM
NDA
22JE17
D2 strike-slip faults
λ2
σ3
λ3
σ2
λ1
σ1
strike-slip
n=10
RDM
NDA
22JE15
D3 normal faults, alluvial fans
σ3
σ2
λ2
λ1
σ1
T-planes
in clasts
λ3
normal
n=17
RDM
NDA
21JE126
D3 faults, coral reef terrace
σ1
σ2
σ3
extensional
n=26
BDM

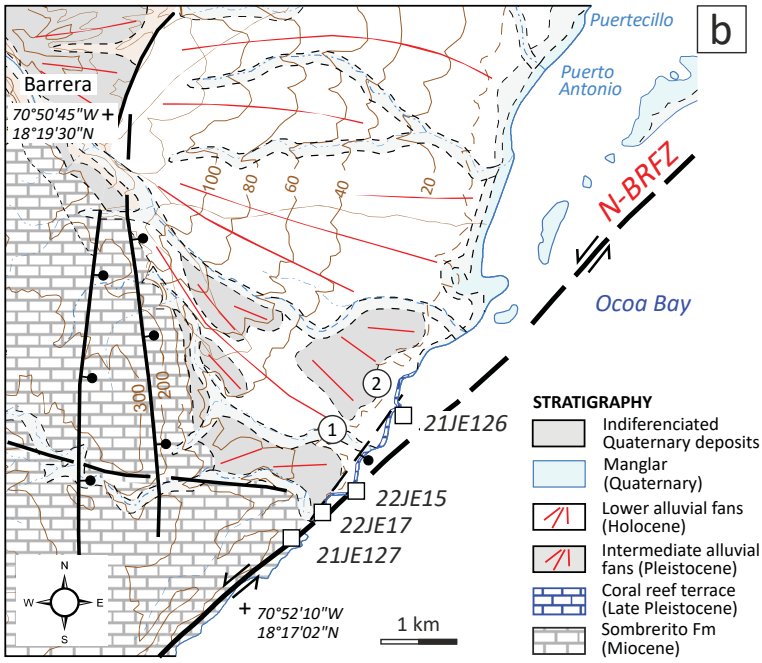
b
Puertecillo
Puerto
Antonio
Barrera
70°50'45"W
18°19'30"N
N-BRFZ
Ocoa Bay
100
80
60
40
20
300
200
1
2
21JE126
22JE15
22JE17
21JE127
N
W
E
S
70°52'10"W
18°17'02"N
1 km
STRATIGRAPHY
Indiferenciated
Quaternary deposits
Manglar
(Quaternary)
Lower alluvial fans
(Holocene)
Intermediate alluvial
fans (Pleistocene)
Coral reef terrace
(Late Pleistocene)
Sombrerito Fm
(Miocene)

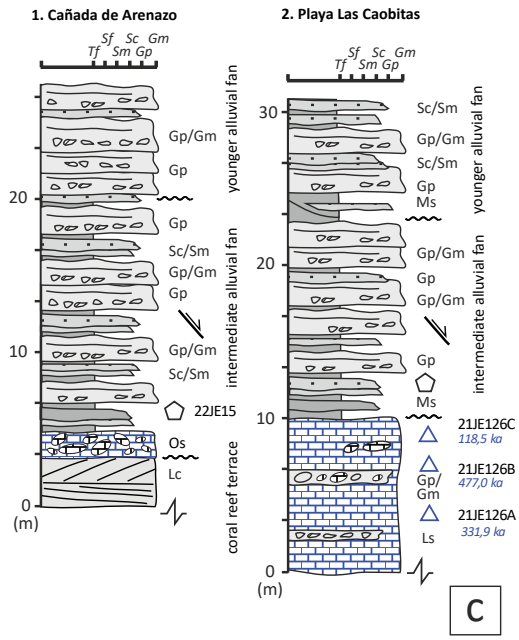
1. Cañada de Arenazo
Sf Sc Gm
Tf Sm Gp
Gp/Gm
Gp
Gp
Sc/Sm
Gp/Gm
Gp
Gp/Gm
Sc/Sm
22JE15
Os
Lc
20
10
0
(m)
younger alluvial fan
intermediate alluvial fan
coral reef terrace
2. Playa Las Caobitas
Sf Sc Gm
Tf Sm Gp
Sc/Sm
Gp/Gm
Sc/Sm
Gp
Ms
Gp/Gm
Gp
Gp/Gm
Gp
Ms
21JE126C
118,5 ka
21JE126B
477,0 ka
Gp/
Gm
21JE126A
331,9 ka
Ls
30
20
10
0
(m)
younger alluvial fan
intermediate alluvial fan
c

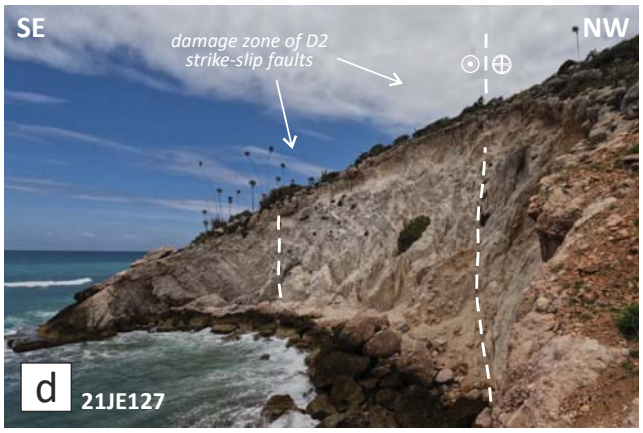
SE
NW
damage zone of D2
strike-slip faults
d
21JE127

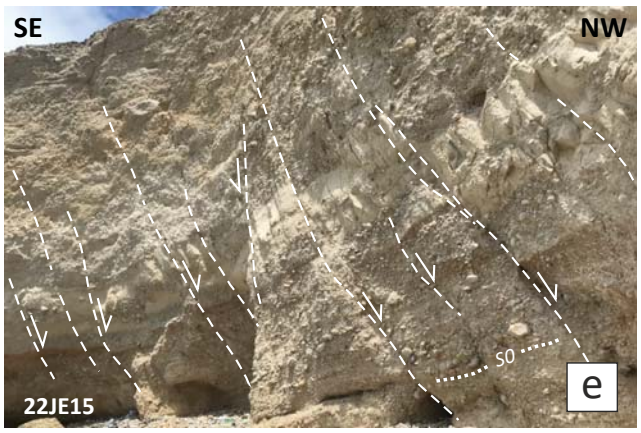
SE
NW
S0
22JE15
e


NE
SW
118ka
21JE126
f


21JE126
g

Figure10.

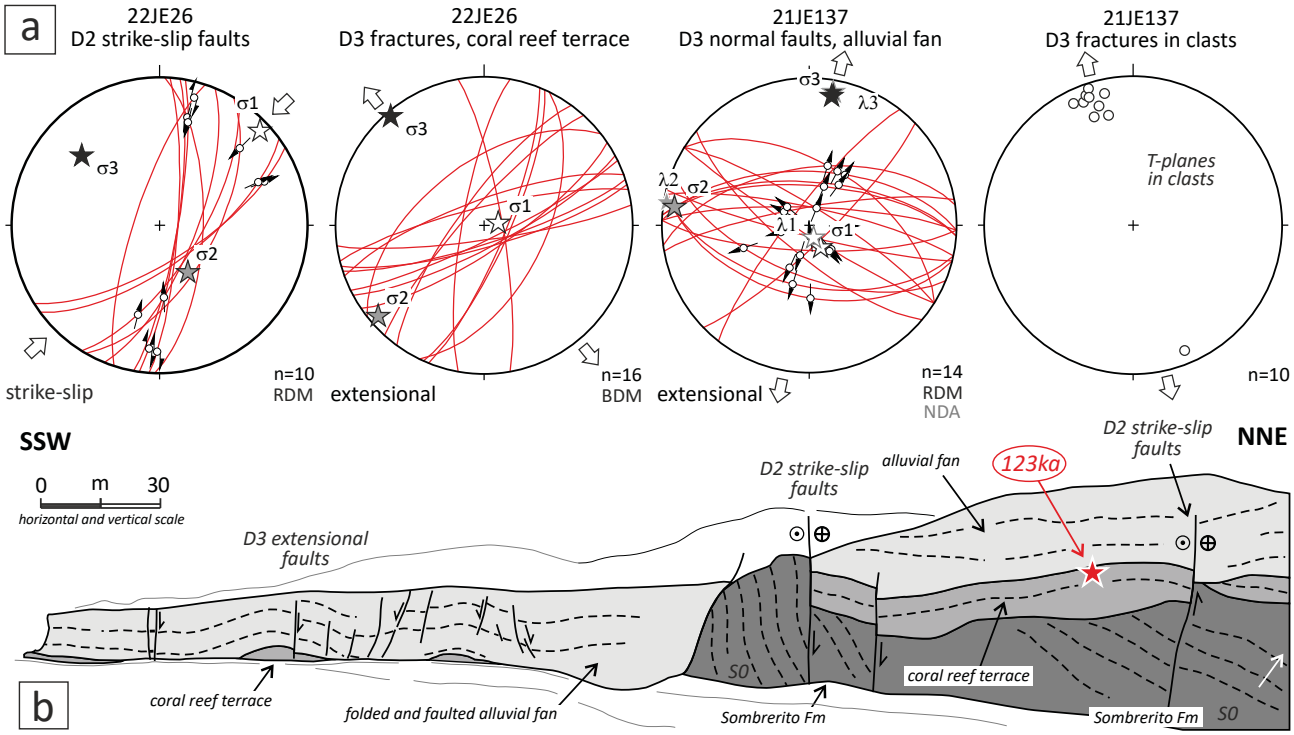
a
22JE26
D2 strike-slip faults
σ1
σ3
σ2
strike-slip
n=10
RDM
22JE26
D3 fractures, coral reef terrace
σ3
σ1
σ2
extensional
n=16
BDM
21JE137
D3 normal faults, alluvial fan
σ3
λ3
λ2
σ2
λ1
σ1
extensional
n=14
RDM
NDA
21JE137
D3 fractures in clasts
T-planes
in clasts
n=10
SSW
NNE
0 m 30
horizontal and vertical scale
D3 extensional
faults
D2 strike-slip
faults
alluvial fan
123ka
D2 strike-slip
faults
S0
coral reef terrace
folded and faulted alluvial fan
Sombrerito Fm
coral reef terrace
Sombrerito Fm
S0
b


c
alluvial fan
coral reef terrace
folded and faulted alluvial fan
Sombrerito Fm
coral reef terrace
Sombrerito Fm

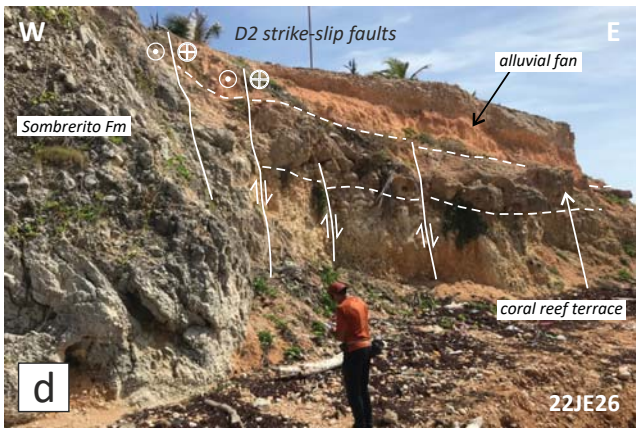
W
D2 strike-slip faults
E
alluvial fan
Sombrerito Fm
coral reef terrace
d
22JE26

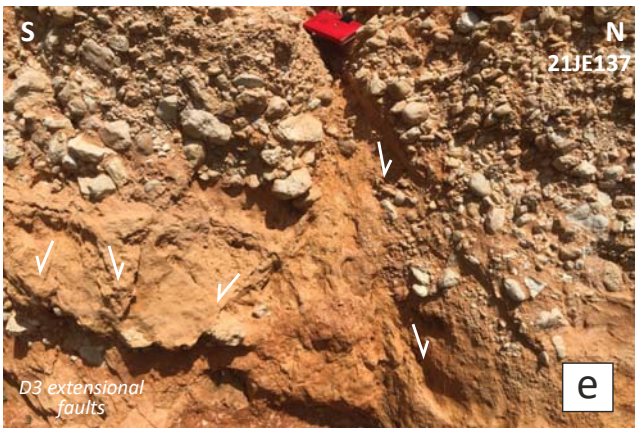
S
N
21JE137
D3 extensional
faults
e

Figure11.

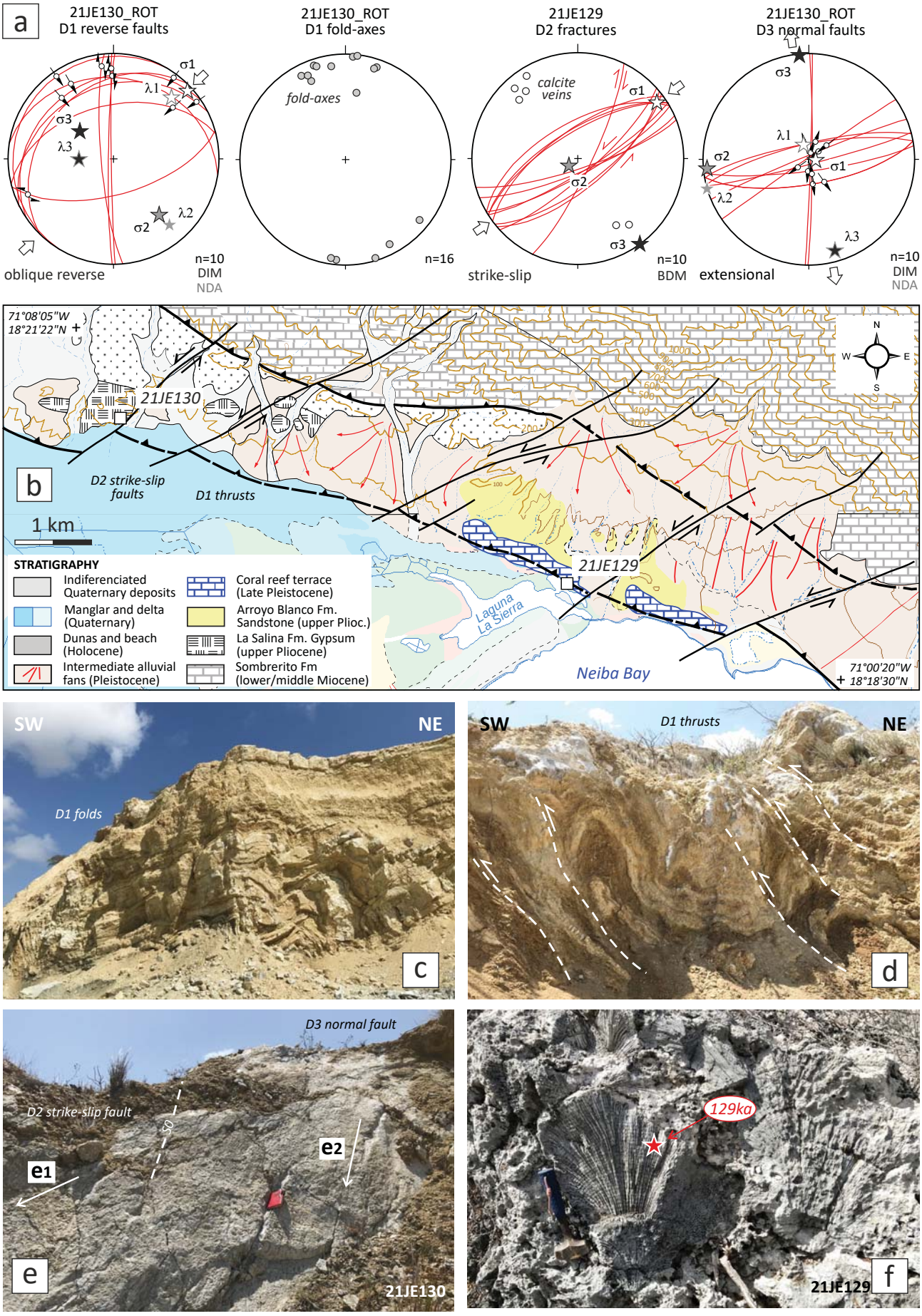
a
21JE130_ROT
D1 reverse faults
σ1
λ1
σ3
λ3
σ2
λ2
oblique reverse
n=10
DIM
NDA
21JE130_ROT
D1 fold-axes
fold-axes
n=16
21JE129
D2 fractures
calcite veins
σ1
σ2
σ3
strike-slip
n=10
BDM
21JE130_ROT
D3 normal faults
σ3
λ1
σ2
σ1
λ2
λ3
extensional
n=10
DIM
NDA
71°08'05"W
18°21'22"N
21JE130
b
D2 strike-slip faults
D1 thrusts
1 km
N
W
E
S
STRATIGRAPHY
Indiferenciated Quaternary deposits
Manglar and delta (Quaternary)
Dunas and beach (Holocene)
Intermediate alluvial fans (Pleistocene)
Coral reef terrace (Late Pleistocene)
Arroyo Blanco Fm. Sandstone (upper Plioc.)
La Salina Fm. Gypsum (upper Pliocene)
Sombrerito Fm (lower/middle Miocene)
21JE129
Laguna La Sierra
Neiba Bay
71°00'20"W
18°18'30"N
SW
NE
D1 folds
c
SW
D1 thrusts
NE
d
D3 normal fault
D2 strike-slip fault
e1
e2
e
21JE130
129ka
21JE129
f

Figure12.

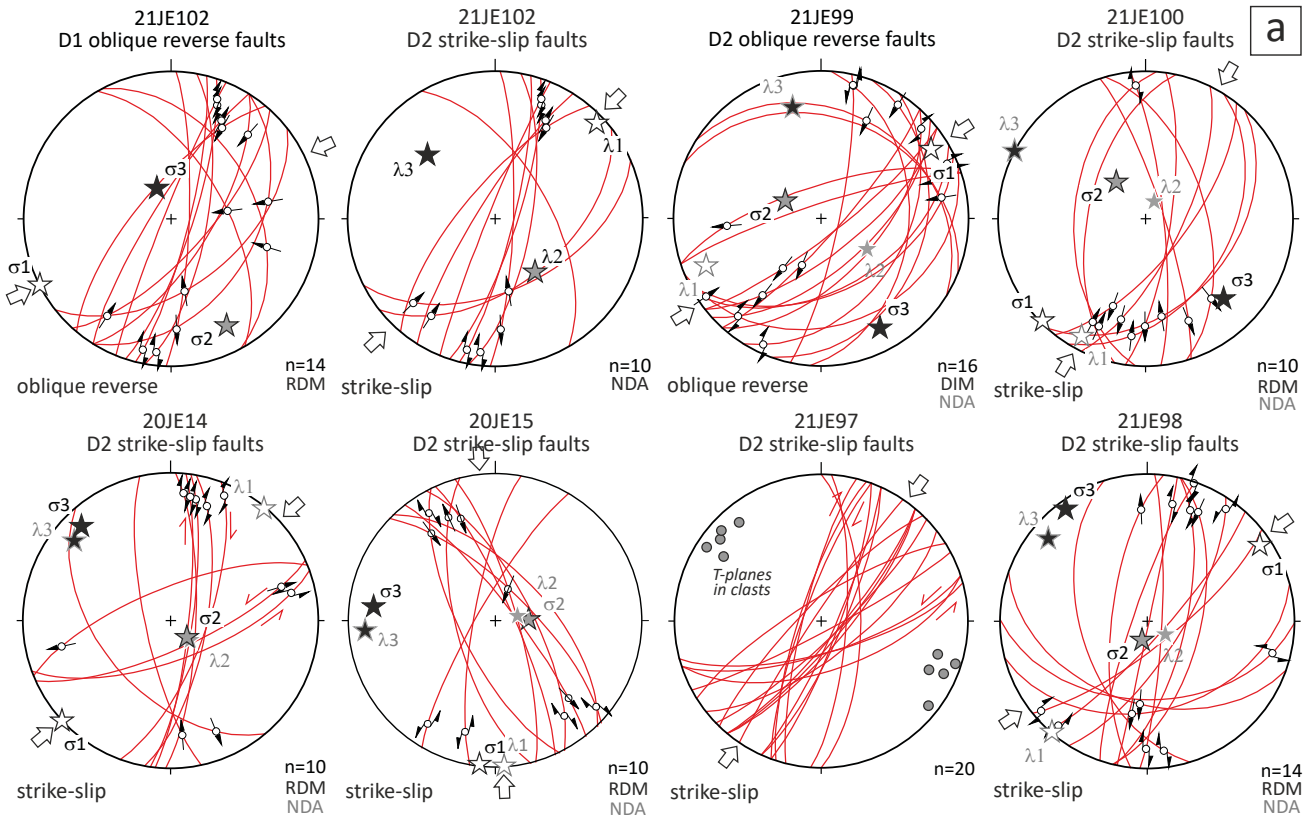
21JE102
D1 oblique reverse faults
σ1
σ3
σ2
oblique reverse
n=14
RDM
21JE102
D2 strike-slip faults
λ3
λ1
λ2
strike-slip
n=10
NDA
21JE99
D2 oblique reverse faults
λ3
σ1
σ2
λ1
λ2
σ3
oblique reverse
n=16
DIM
NDA
21JE100
D2 strike-slip faults
a
λ3
σ2
λ2
σ1
σ3
λ1
strike-slip
n=10
RDM
NDA
20JE14
D2 strike-slip faults
σ3
λ3
λ1
σ2
λ2
σ1
strike-slip
n=10
RDM
NDA
20JE15
D2 strike-slip faults
λ2
σ2
σ3
λ3
σ1
λ1
strike-slip
n=10
RDM
NDA
21JE97
D2 strike-slip faults
T-planes
in clasts
strike-slip
n=20
21JE98
D2 strike-slip faults
σ3
λ3
σ1
σ2
λ2
λ1
strike-slip
n=14
RDM
NDA

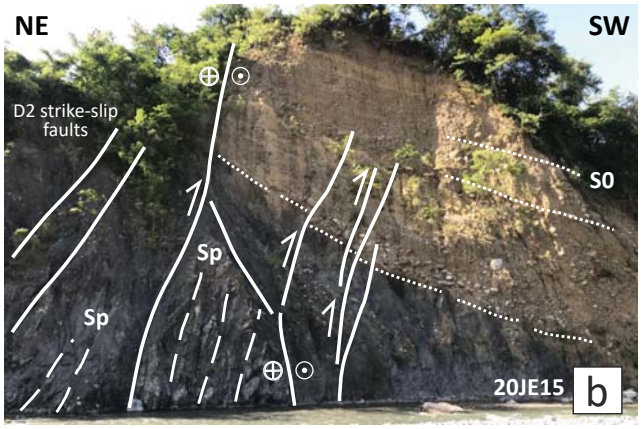
NE
SW
D2 strike-slip
faults
S0
Sp
Sp
20JE15
b

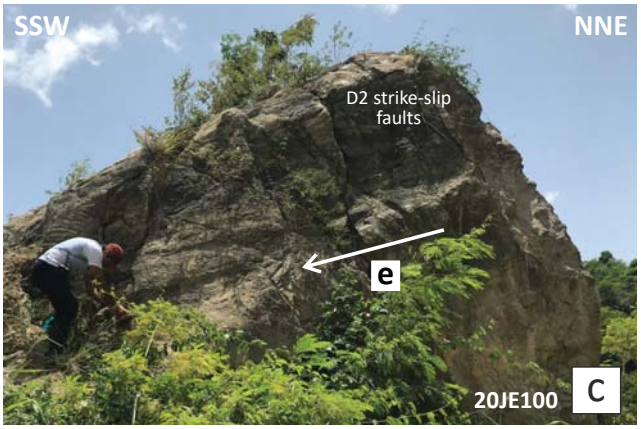
SSW
NNE
D2 strike-slip
faults
e
20JE100
c


SSW
NNE
D2 strike-slip
faults
e
20JE100
d

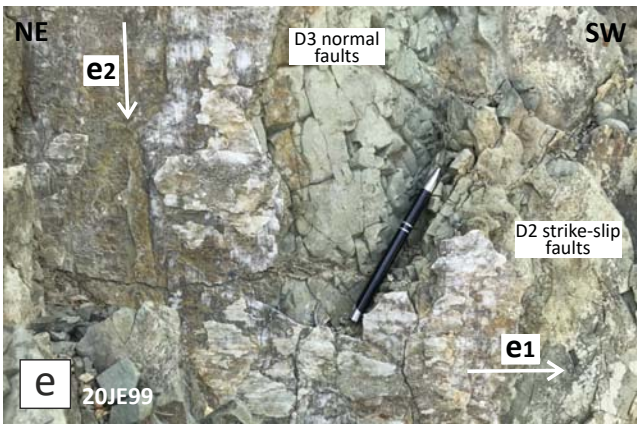
NE
SW
e2
D3 normal
faults
D2 strike-slip
faults
e1
e
20JE99

Figure13.

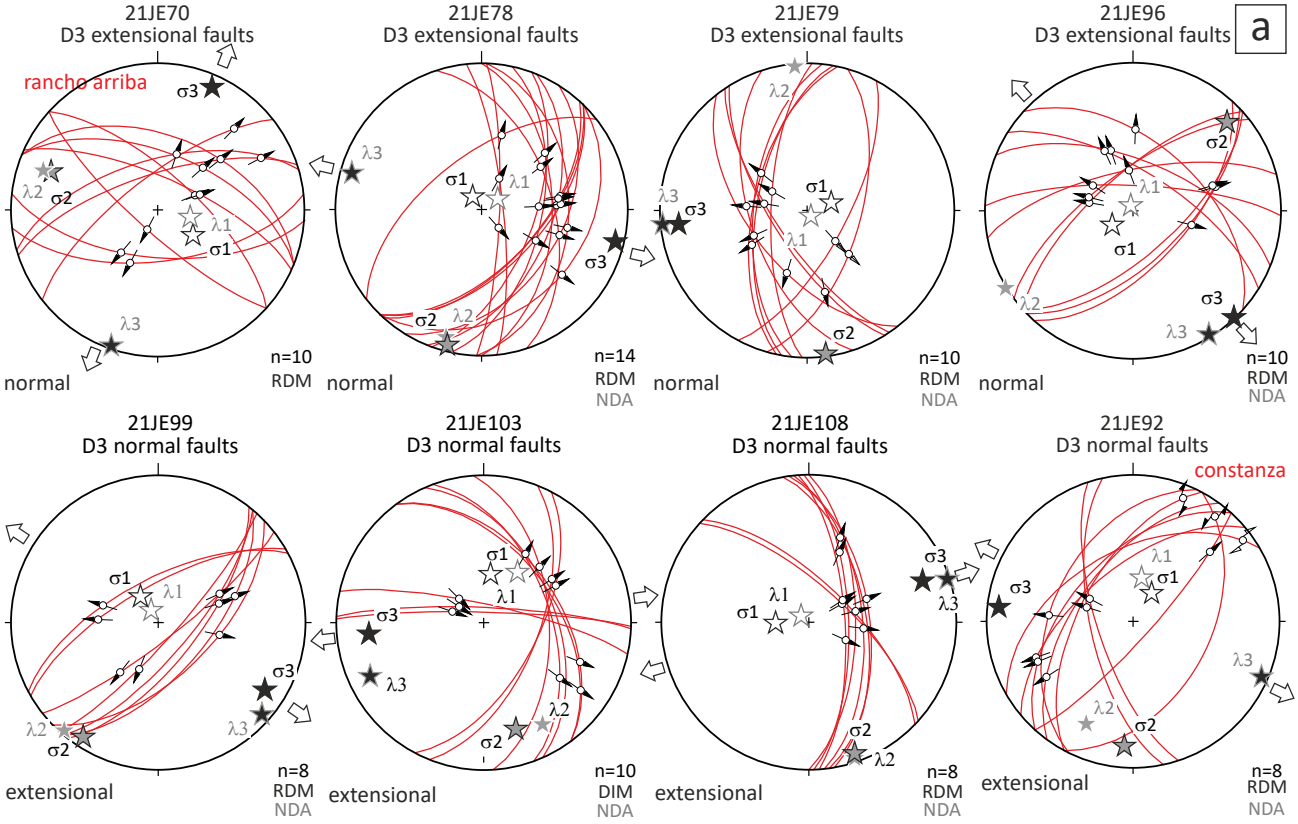
a
21JE70
D3 extensional faults
rancho arriba
σ3
λ2
σ2
λ1
σ1
λ3
normal
n=10
RDM
21JE78
D3 extensional faults
λ3
σ1
λ1
σ3
σ2
λ2
normal
n=14
RDM
NDA
21JE79
D3 extensional faults
λ2
λ3
σ3
σ1
λ1
σ2
normal
n=10
RDM
NDA
21JE96
D3 extensional faults
σ2
λ1
σ1
λ2
σ3
λ3
normal
n=10
RDM
NDA
21JE99
D3 normal faults
σ1
λ1
σ3
λ2
σ2
λ3
extensional
n=8
RDM
NDA
21JE103
D3 normal faults
σ1
λ1
σ3
λ3
λ2
σ2
extensional
n=10
DIM
NDA
21JE108
D3 normal faults
σ3
λ3
λ1
σ1
σ2
λ2
extensional
n=8
RDM
NDA
21JE92
D3 normal faults
constanza
λ1
σ1
σ3
λ3
λ2
σ2
extensional
n=8
RDM
NDA

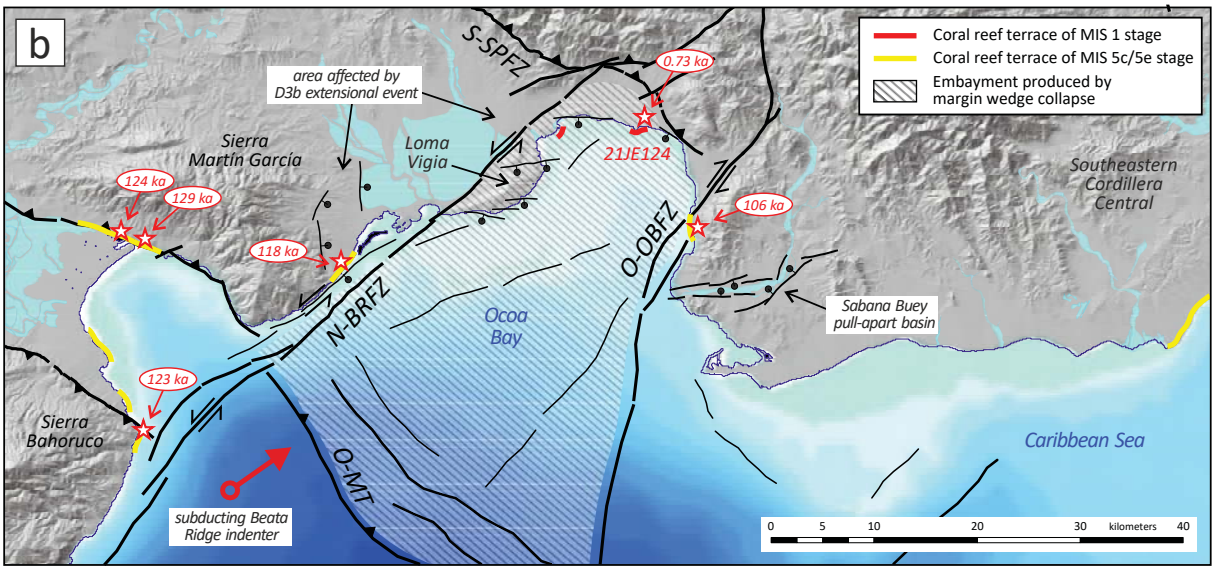
b
Coral reef terrace of MIS 1 stage
Coral reef terrace of MIS 5c/5e stage
Embayment produced by margin wedge collapse
area affected by D3b extensional event
S-SPFZ
0.73 ka
21JE124
Sierra Martín García
Loma Vigia
124 ka
129 ka
118 ka
106 ka
O-OBFZ
N-BRFZ
Ocoa Bay
Southeastern Cordillera Central
Sabana Buey pull-apart basin
123 ka
Sierra Bahoruco
O-MT
subducting Beata Ridge indenter
Caribbean Sea
0
5
10
20
30
kilometers
40

Figure14.

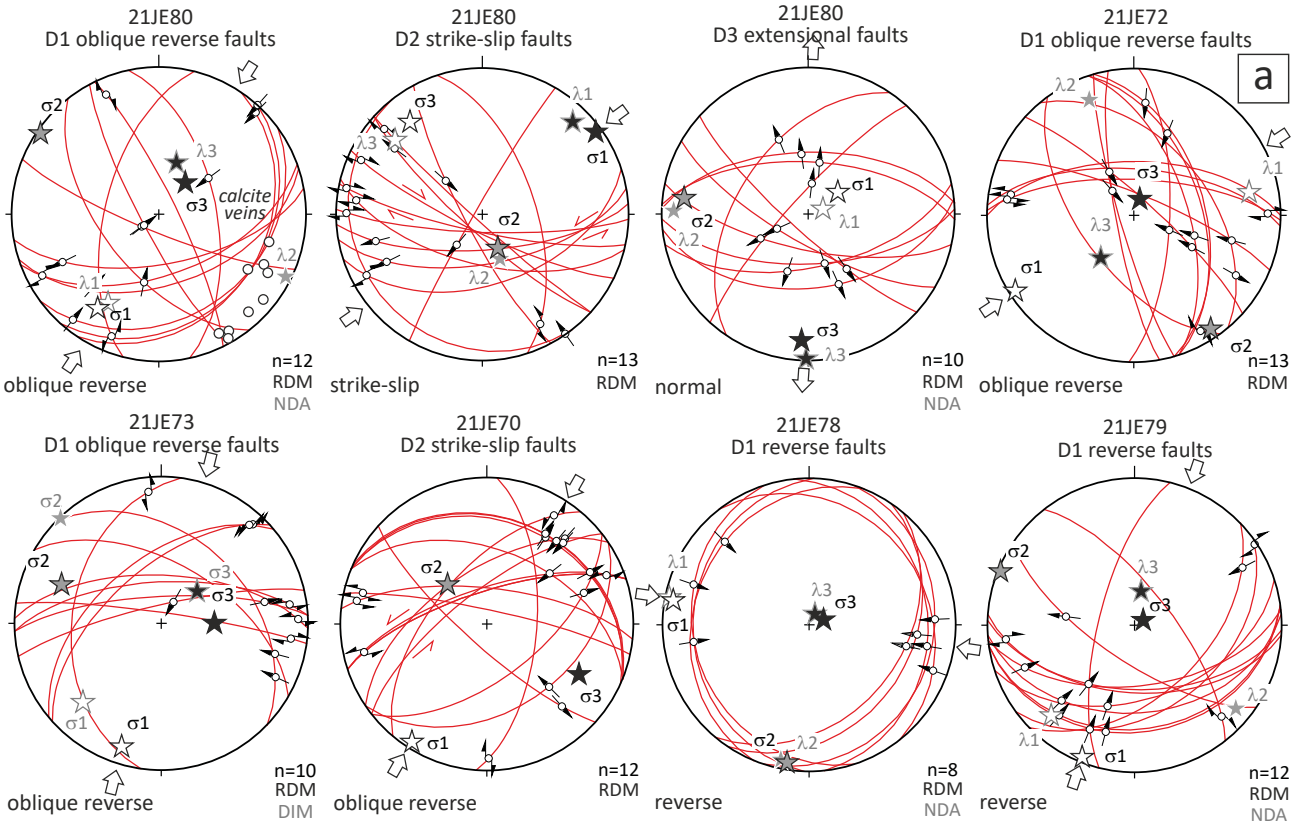
21JE80
D1 oblique reverse faults
σ2
λ3
σ3
calcite veins
λ2
λ1
σ1
oblique reverse
n=12
RDM
NDA
21JE80
D2 strike-slip faults
σ3
λ1
σ1
λ3
σ2
λ2
strike-slip
n=13
RDM
21JE80
D3 extensional faults
σ1
λ1
σ2
λ2
σ3
λ3
normal
n=10
RDM
NDA
21JE72
D1 oblique reverse faults
a
λ2
λ1
σ3
λ3
σ1
σ2
oblique reverse
n=13
RDM
21JE73
D1 oblique reverse faults
σ2
σ2
σ3
σ3
σ1
σ1
oblique reverse
n=10
RDM
DIM
21JE70
D2 strike-slip faults
σ2
σ3
σ1
oblique reverse
n=12
RDM
21JE78
D1 reverse faults
λ1
λ3
σ3
σ1
σ2
λ2
reverse
n=8
RDM
NDA
21JE79
D1 reverse faults
σ2
λ3
σ3
λ2
λ1
σ1
reverse
n=12
RDM
NDA

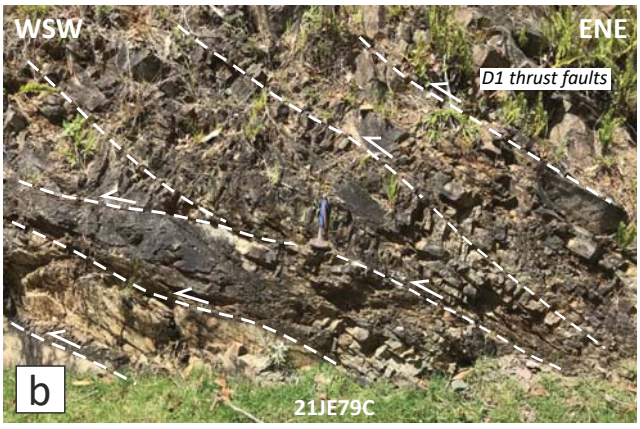
WSW
ENE
D1 thrust faults
b
21JE79C

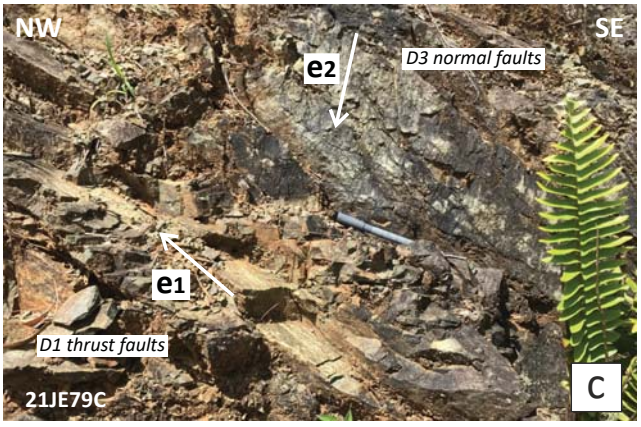
NW
SE
e2
D3 normal faults
e1
D1 thrust faults
21JE79C
c

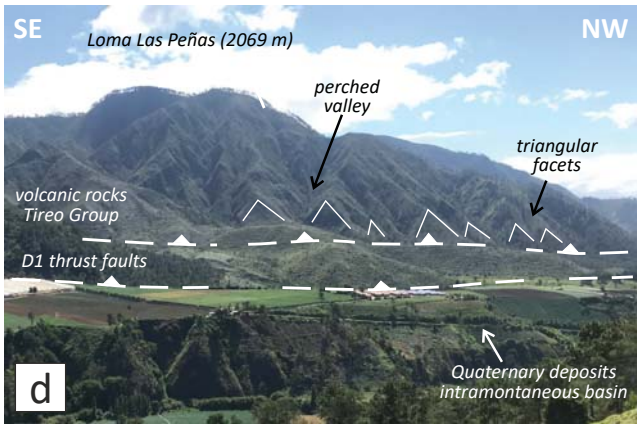
SE
Loma Las Peñas (2069 m)
NW
perched valley
triangular facets
volcanic rocks Tireo Group
D1 thrust faults
Quaternary deposits intramontaneous basin
d

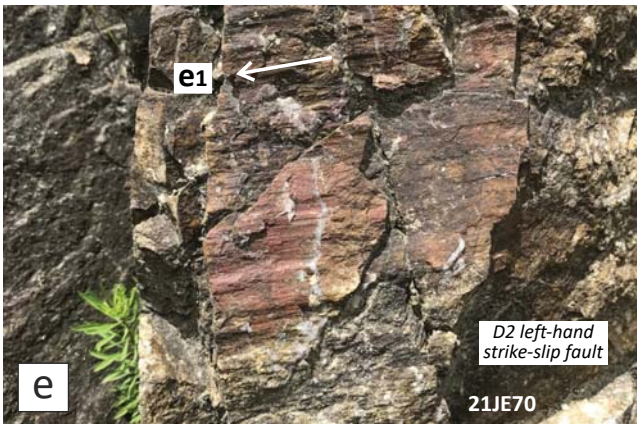
e1
D2 left-hand strike-slip fault
e
21JE70

Figure15.

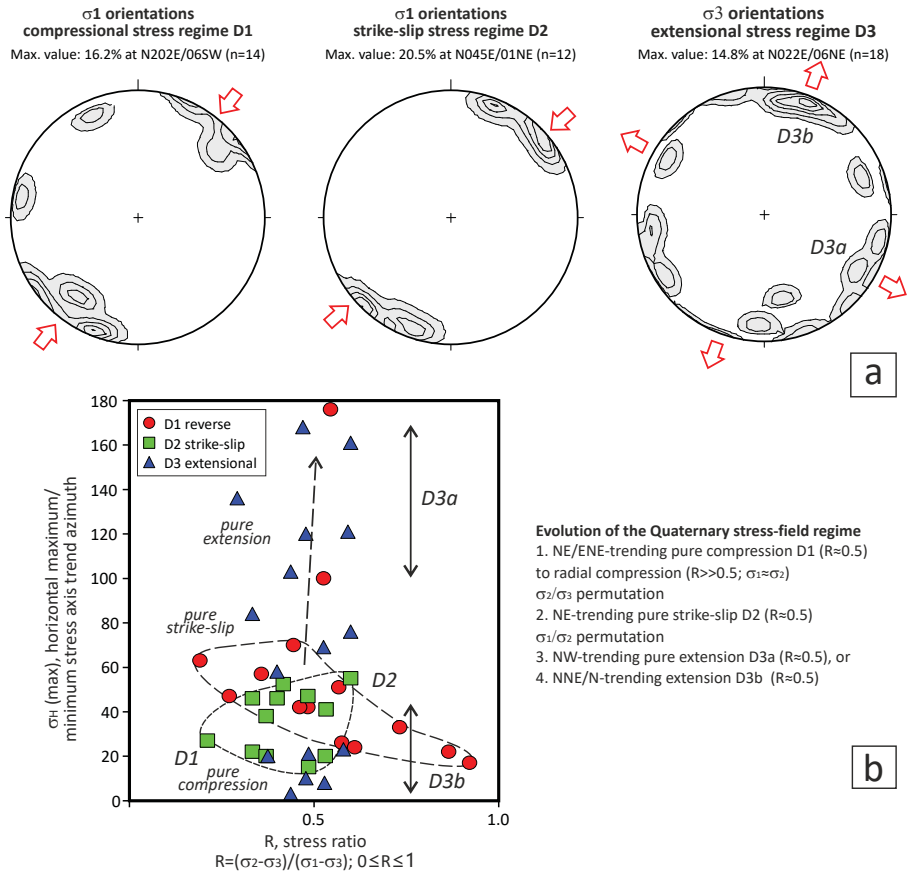

Evolution of the Quaternary stress-field regime

1. NE/ENE-trending pure compression D1 (R≈0.5) to radial compression (R>>0.5; $\sigma_1 \approx \sigma_2$) σ_2/σ_3 permutation
2. NE-trending pure strike-slip D2 (R≈0.5) σ_1/σ_2 permutation
3. NW-trending pure extension D3a (R≈0.5), or
4. NNE/N-trending extension D3b (R≈0.5)

Figure16.

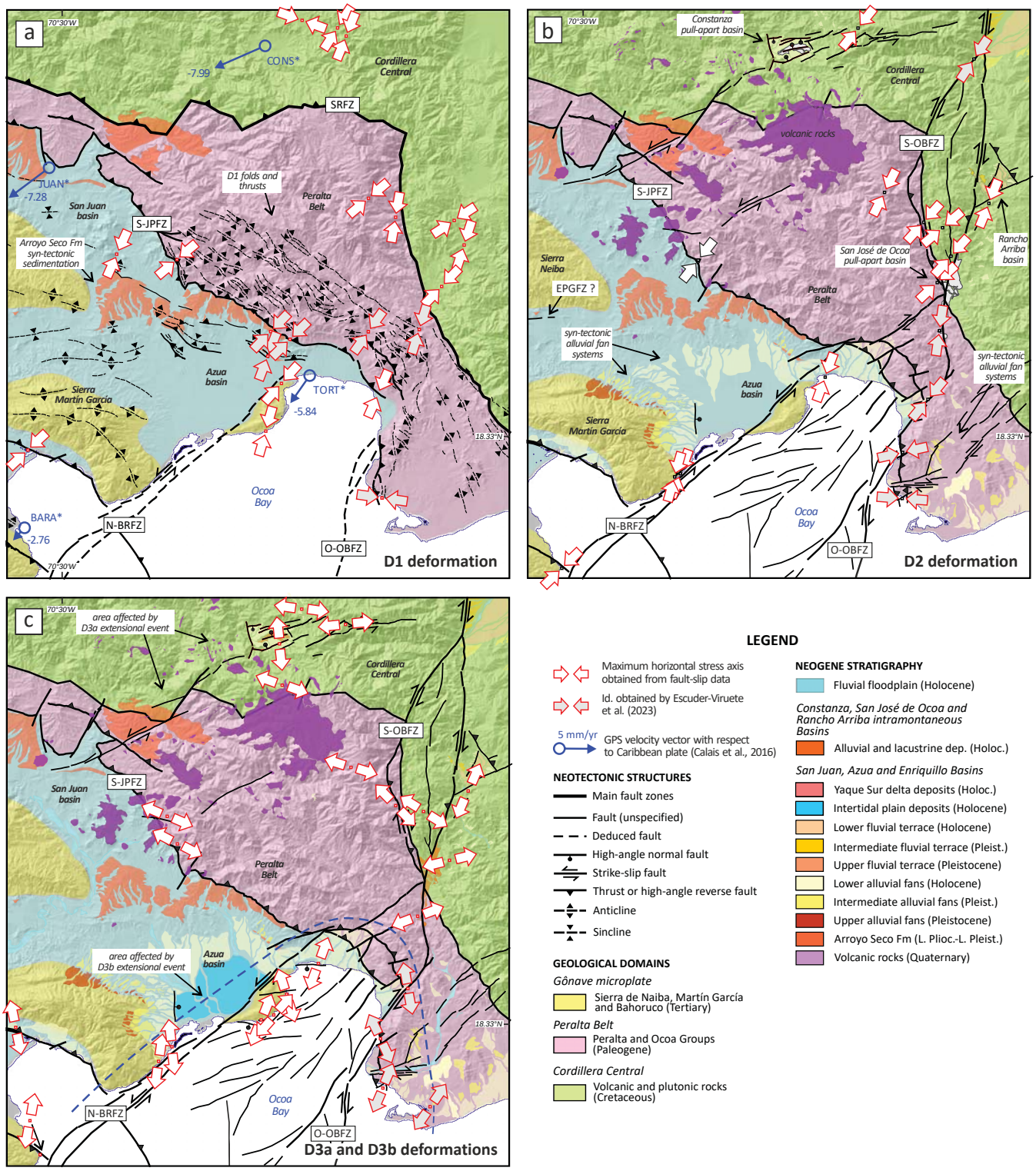
a
70°30'W
CONS*
-7.99
Cordillera Central
SRFZ
JUAN*
-7.28
San Juan basin
D1 folds and thrusts
Peralta Belt
S-JPFZ
Arroyo Seco Fm syn-tectonic sedimentation
Azua basin
Sierra Martín García
TORT*
-5.84
18.33°N
Ocoa Bay
BARA*
-2.76
N-BRFZ
O-OBFZ
70°30'W
D1 deformation
b
70°30'W
Constanza pull-apart basin
Cordillera Central
volcanic rocks
S-OBFZ
S-JPFZ
Sierra Neiba
EPGFZ ?
San José de Ocoa pull-apart basin
Rancho Arriba basin
Peralta Belt
syn-tectonic alluvial fan systems
Azua basin
Sierra Martín García
18.33°N
Ocoa Bay
N-BRFZ
O-OBFZ
D2 deformation
c
70°30'W
area affected by D3a extensional event
Cordillera Central
S-OBFZ
S-JPFZ
San Juan basin
Peralta Belt
area affected by D3b extensional event
Azua basin
18.33°N
Ocoa Bay
N-BRFZ
O-OBFZ
D3a and D3b deformations
LEGEND
Maximum horizontal stress axis obtained from fault-slip data
Id. obtained by Escuder-Viruete et al. (2023)
5 mm/yr
GPS velocity vector with respect to Caribbean plate (Calais et al., 2016)
NEOTECTONIC STRUCTURES
Main fault zones
Fault (unspecified)
Deduced fault
High-angle normal fault
Strike-slip fault
Thrust or high-angle reverse fault
Anticline
Sincline
GEOLOGICAL DOMAINS
Gônave microplate
Sierra de Naiba, Martín García and Bahoruco (Tertiary)
Peralta Belt
Peralta and Ocoa Groups (Paleogene)
Cordillera Central
Volcanic and plutonic rocks (Cretaceous)
NEOGENE STRATIGRAPHY
Fluvial floodplain (Holocene)
Constanza, San José de Ocoa and Rancho Arriba intramontaneous Basins
Alluvial and lacustrine dep. (Holoc.)
San Juan, Azua and Enriquillo Basins
Yaque Sur delta deposits (Holoc.)
Intertidal plain deposits (Holocene)
Lower fluvial terrace (Holocene)
Intermediate fluvial terrace (Pleist.)
Upper fluvial terrace (Pleistocene)
Lower alluvial fans (Holocene)
Intermediate alluvial fans (Pleist.)
Upper alluvial fans (Pleistocene)
Arroyo Seco Fm (L. Plioc.-L. Pleist.)
Volcanic rocks (Quaternary)

Figure17.

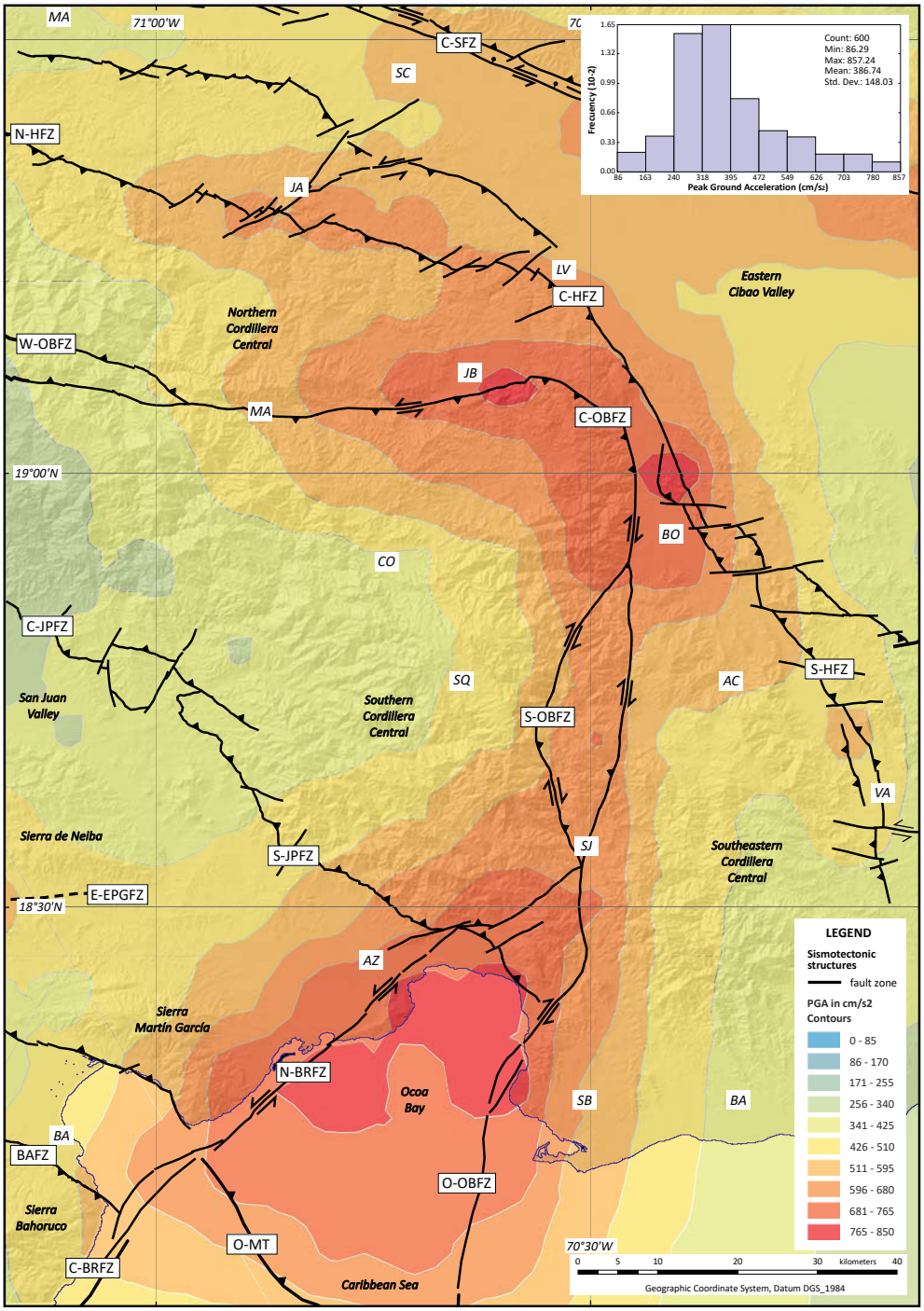
MA
71°00'W
C-SFZ
SC
N-HFZ
JA
LV
C-HFZ
Eastern
Cibao Valley
Northern
Cordillera
Central
W-OBFZ
JB
MA
C-OBFZ
19°00'N
BO
CO
C-JPFZ
SQ
AC
S-HFZ
San Juan
Valley
Southern
Cordillera
Central
S-OBFZ
VA
Sierra de Neiba
S-JPFZ
SJ
Southeastern
Cordillera
Central
E-EPGFZ
18°30'N
AZ
Sierra
Martin Garcia
N-BRFZ
Ocoa
Bay
SB
BA
BA
BAFZ
O-OBFZ
Sierra
Bahoruco
O-MT
C-BRFZ
Caribbean Sea
70°30'W
0 5 10 20 30 kilometers 40
Geographic Coordinate System, Datum DGS_1984
Frecuency (10-2)
1.65
1.32
0.99
0.66
0.33
0.00
86 163 240 318 395 472 549 626 703 780 857
Peak Ground Acceleration (cm/s2)
Count: 600
Min: 86.29
Max: 857.24
Mean: 386.74
Std. Dev.: 148.03
LEGEND
Sismotectonic structures
fault zone
PGA in cm/s2
Contours
0 - 85
86 - 170
171 - 255
256 - 340
341 - 425
426 - 510
511 - 595
596 - 680
681 - 765
765 - 850

Table 1. Characteristics of neotectonic strictires in southern central Hispaniola

Deformative event	*Main structures*	*Stress regime*	*Age*
D1	NW to WNW-striking folds and thrusts. Large-scale structure of the Cordillera Central and Peralta belt.	Compression. NE-trending σ_1 axis.	Lower Miocene to Early Pleistocene
D2	N-S to NE-SW strike-slip faults and fault segment. Transverse structures related to Ocoa-Bonao-La Guácara and Beata Ridge fault zones. ENE to E-striking left-lateral strike-slip faults. Transverse structures in the NW sector.	Near pure strike-slip. NE-trending σ_1 axis.	Early-Middle Pleistocene to Holocene
D3	Extensional faults. D3a, NE to NNE striking faults in the Cordillera Central sector; D3b, WNW to W striking faults in the Ocoa Bay sector. Alignment of the Quaternary emissive centers.	D3a, NW-directed pure extension; D3b, N to NNE-directed extension.	Late Pleistocene-Holocene

Table 2. Characteristics of the main seismotectonic structures in southern central Hispaniola

Code	*Fault/segment name*	*Deformation mechanism*	*Maximum estimated magnitude (M_w)*	*Major known earthquake and magnitude (M_w)*	*Estimated displacement rate* [a]	*Lenght* [b]	*Azimuth and dip of fault zone* [b]
S-OBFZ	Southern Ocoa-Bonao-La Guacara Fault Zone	right-lateral strike-slip	M_{max} 6,5 (± 0,5)	unknown	0.4 (± 0.2) mm/yr	60 (± 10) km	N010°E to N030°E, subvertical dip
C-OBFZ	Central Ocoa-Bonao-La Guacara Fault Zone	oblique reverse	M_{max} 6,5 (± 0,5)	unknown	0.4 (± 0.2) mm/yr	50 (± 10) km	N160°E to N010°E, subvertical dip to 40° (±15) W
W-OBFZ	Western Ocoa-Bonao-La Guacara Fault Zone	left-lateral oblique reverse to strike-slip	M_{max} 6,0 (± 1,0)	1562 earthquake?	0.2 (± 0.1) mm/yr	90 to 120 km	N100°E to N150°E, 45° (±15) SW to subvertical dip
S-HFZ	Southern Hispaniola Fault Zone	righ-lateral strike-slip?	M_{max} 7.1 (± 0.3)	unknown	< 0.2 mm/yr	50 to 70 km	N140°E (±15), subvertical dip
E-MAFZ	Eastern Sierra de Neiba-Matheux thrust	left-lateral oblique reverse to thrust	M_{max} 5.8 (± 0.3)	1942 (Mw 5.8)	0.2 mm/yr	segments of 30 (± 5) km	N120°S (±15), 65° (±10) N
S-JPFZ	Southern San Juan - Pozos Fault Zone	left-lareal oblique revrese to thust	M_{max} 6.5 (± 0.5)	1911 (Mw 6.7)	1.5 (± 1.5) mm/yr	>250 km, including segments and imbrications	N130°E (±15), 45° (±15) NE
BAFZ	Bahoruco Fault Zone or Barahona Thrust	reverse	M_{max} 7.0 (± 0.6)	1963, Mw 5.7; FD 9 km	0.2 mm/yr	50 to 85 km, including segments and imbrications	N100°E (±15), 50° (±15) S
E-EPGFZ	Eastern Enriquillo-Plantain Garden Fault Zone	left-lateral strike-slip to oblique reverse	M_{max} 7.3 (± 0.3)	1751 (Mw 7.5)?, 2010 (Mw 7.0)	8.3 (± 2.0) mm/yr	80 (± 10) km	N080°E (±10), subvertical dip
N-BRFZ	Northern Beata Ridge Fault Zone	left-lateral strike-slip to reverse	M_{max} 6.5 (± 0.1), recorded: 4.3 (12/09/2005) and 4.1 (12/10/2013)	1751 (Mw 7.5-8.0)?, 1691?	0.2 mm/yr, probably	60 (± 5) km	N040°E (±10), subvertical dip
C-BRFZ	Central Beata Ridge Fault Zone	left-lateral strike-slip to normal dip-slip	M_{max} 6.5 (± 0.1), recorded: 4.3 (12/09/2005) and 4.1 (12/10/2013)	1751 (Mw 7.5-8.0)?, 1691?	0.2 mm/yr, probably	100 (± 5) km	N030°E (±10), 70° (±15) E to subvertical dip
W-MT	Western Muertos Trough	reverse to oblique reverse	M_{max} 7.5 (± 0.5)	1673 (Mw 7.3)?; 1691 (Mw 7.7)?; 1751 (Mw 7.5-8.0)?	6.2 (± 1.0) mm/yr	170 km	N100°E (±5), 12° (±5) northward dip
W-DEEP-MT	Western Muertos Trough, deep part	reverse to oblique reverse	M_{max} 7.5 (± 0.5)	1673 (Mw 7.3)?; 1691 (Mw 7.7)?; 1751 (Mw 7.5-8.0)?	6.2 (± 1.0) mm/yr	170 km	N100°E (±5), 40° (±5) northward dip

O-MT	Muertos Trough, Ocoa Bay part	reverse to oblique reverse	M_{max} 7.5 (± 0.5)	1751 (Mw 7.5-8.0)?	6.2 (± 1.0) mm/yr	40 km	N135°E (±5), 15° (±5) northward dip

[a]Derived from geological mapping (SYSMIN Project, 2010; Escuder-Viruete, 2022; this work), geodetic GPS measurements (Calais

[b]Derived from geological mapping (SYSMIN Project, 2010; Bertil et al., 2015; Terrier-Sedan & Bertil, 2021; Escuder-Viruete, 2022;

Width of fault zone[b]
10 ± 5 km
10 ± 5 km
5 ± 2 km
10 ± 5 km
15 ± 5 km
7 ± 5 km
7 ± 5 km
10 ± 5 km
10 ± 5 km
10 ± 5 km
20 ± 15 km
20 ± 15 km

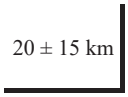

et al., 2002; Manaker et al., 2008) and empirical relationships (e.g. Wells and Coppersmith, 1994). Escuder-Viruete et al., 2023; this work))

Manuscript accepted for publication in Geochemistry, Geophysics, Geosystems

Supporting Information for

Active tectonics, Quaternary stress regime evolution and seismotectonic faults in southern central Hispaniola: implications for the quantitative seismic hazard assessment

J. Escuder-Viruete [1], F.J. Fernández [2], F. Pérez Valera [3], F. McDermott [4]

[1]Instituto Geológico y Minero España - CSIC, C. La Calera 1, 28760 Tres Cantos, Madrid. Spain

[2]Departamento de Geología, Universidad de Oviedo. C. Jesús Arias de Velasco, 33005 Oviedo. Spain

[3]Departamento de Ciencias de la Tierra y del Medio Ambiente, Universidad de Alicante. 03080 Sant Vicent de Raspeig, Alicante. Spain

[4]School of Earth Sciences. University College Dublin, Belfield. Dublin 4. Ireland.

Contents of this file

Additional Supporting Information (Files uploaded separately)

Introduction

This supporting information provides a Figure with the graphic representation of the catalogue of earthquakes and focal mechanisms compiled for southern central Hispaniola (S1), a Table including the U-Th geochronological results of coral samples (S2), a Text describing the methodology of dynamic fault-slip analysis (S3), a Table describing the sites used to obtain stress tensors from the analysis of fault-slip data sets (S4), a Table including the stress tensors obtained by methods of inversion of fault-slip data (S5), and a Table showing the maximum horizontal stresses and tectonic regimes obtained by inversion methods (S6).

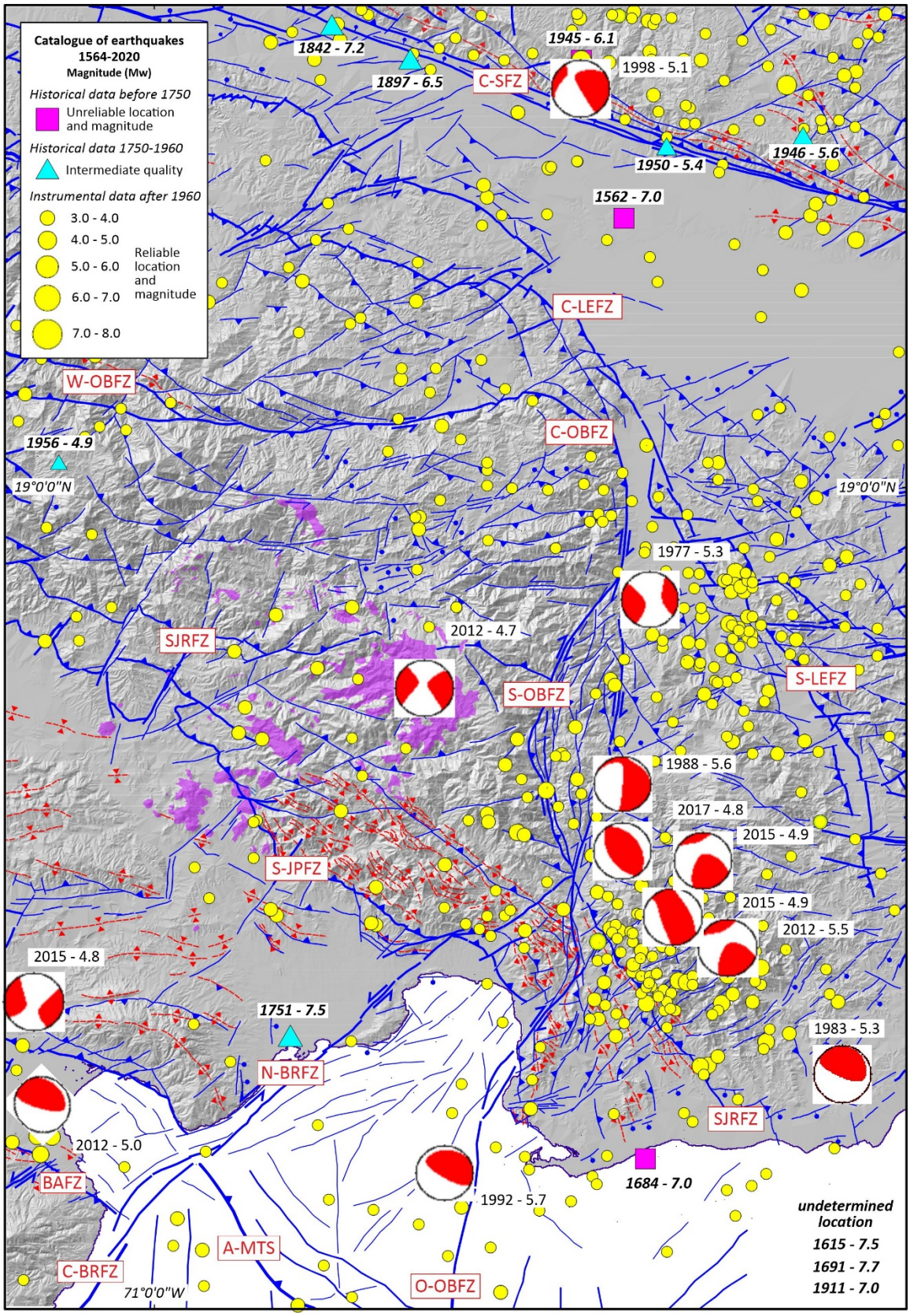
Catalogue of earthquakes
1564-2020
Magnitude (Mw)
Historical data before 1750
Unreliable location and magnitude
Historical data 1750-1960
Intermediate quality
Instrumental data after 1960
3.0 - 4.0
4.0 - 5.0
5.0 - 6.0
6.0 - 7.0
7.0 - 8.0
Reliable location and magnitude
1842 - 7.2
1897 - 6.5
1945 - 6.1
1998 - 5.1
C-SFZ
1946 - 5.6
1950 - 5.4
1562 - 7.0
C-LEFZ
W-OBFZ
C-OBFZ
1956 - 4.9
19°0'0"N
19°0'0"N
1977 - 5.3
SJRFZ
2012 - 4.7
S-OBFZ
S-LEFZ
1988 - 5.6
2017 - 4.8
2015 - 4.9
S-JPFZ
2015 - 4.9
2012 - 5.5
2015 - 4.8
1751 - 7.5
N-BRFZ
1983 - 5.3
SJRFZ
2012 - 5.0
BAFZ
1684 - 7.0
1992 - 5.7
undetermined location
1615 - 7.5
1691 - 7.7
1911 - 7.0
A-MTS
C-BRFZ
71°0'0"W
O-OBFZ

Figure Supporting Information S1.

Catalogue of earthquakes and focal mechanisms compiled for southern central Hispaniola. White symbols are historical and instrumental earthquakes of Mw > 3.0 from 1564 to 2020 A.D. Due to the high uncertainty related to the magnitude and location of historical earthquakes, they are classified into three groups following Terrier-Sedan & Bertil (2021): historical data before 1750 of unreliable magnitude and location; historical data between 1750 and 1960 of intermediate quality; and instrumental data after 1960 generally of high quality. More than 12 epicentres of earthquakes of magnitude at least Mw 6.0 are located in the study area, or the immediate surroundings They include the earthquakes of 1562 (destroyed La Vega and Santiago de los Caballeros), 1615 (destroyed Santo Domingo), 1684 (affected Azua and Santo Domingo), 1691 (destroyed Azua, affected Santo Domingo), 1751 (destroyed Azua) and 1911 (affected San Juan). Well-constrained fault plane solutions from 1976-2021 are taken from the Global Centroid-Moment-Tensor (CMT) Catalog (Ekström et al., 2012). Outcrops of Quaternary volcanic rocks are indicated in purple. Details on the data sources can be found in Escuder-Viruete (2022) and Escuder-Viruete et al. (2023).

Text Supporting Information S3. Methodology of dynamic fault-slip analysis

The reconstruction in time and space of the different tectonic paleostress tensors in the studied area involved the use of different inversion methods. This approach is key when working with fault-slip inversion techniques in order to account for the critical assumptions and limitations of each method (see reviews by Célérier et al., 2012 Sperner & Zweigel, 2010; Twiss & Unruh, 1998). Using multiple methods, hence different algorithms, will allow us to increase accuracy in the results by reducing the effect of systematic errors.

Input data. Fault-slip data were collected at several localities along southern central Hispaniola and used to determine the stresses causing the observed brittle deformations. A fault-slip data is composed of the fault plane orientation (dip azimuth and dip angle), the slip orientation (striae, bearing and plunge), and the sense of slip (normal, reverse, sinistral, dextral). Mesoscopic kinematic indicators used to infer the sense of slip on the fault-plane along the striae direction were the growth of fibrous crystals (slickensides) in steps, R and R´ shears, grooves and half-moon, among others (e.g. Petit, 1987).

Carey and Brunier (1974) have demonstrated that from numerous fault-slip data obtained from outcrops, it is possible to investigate the stresses responsible for the fault movements and for the observed deformation. Each state of stress is expressed as a reduced stress, or paleostress, tensor, which includes the orientations of the three principal stress axes (σ1, σ2 and σ3) and the ratio of principal stress differences [$R = (\sigma2 - \sigma3)/(\sigma1 - \sigma3)$]. Fault crosscutting relationships, the overprinting of several striations in the same fault plane and the absolute age of the faulted rocks have been used as primary criteria to date faults and thus paleostress tensors and tectonic phases.

In natural conditions, fault-slip data sets measured at one location can be polyphasic, that is, include several fault subpopulations consistent with different stress tensors. The separation of the fault subpopulations referring to each tensor was performed prior to the inversion method for stress, calculating the pressure (P or compression axis) and tension (T or tensional axis) axes for each fault-slip data. Appearance of several clusters of P or T axes in stereographic projection was interpreted as indicative of the existence of fault-slip data related to different paleostress tensors, allowing their separation in fault subpopulations.

The different paleostress tensors and stress regimes were attributed to the lithostratigraphic units where the major and minor faults were measured. The available absolute ages of each unit enabled assigning an age to each faulting event. This information, combined with a relative chronology of fault offsets based on field observations, allowed to distinguish the main tectonic events that have characterized the study area from the early Miocene to the Holocene.

Sites of measurements located in the oldest lithostratigraphic units allow recognizing the faults of different tectonic events, where multiple generations of structures are linked to successive tectonic phases. The systematic lacking of structures belonging to a given tectonic phase in a lithostratigraphic unit can indicate the existence of deformation partitioning in space or constrain the oldest age of the deformation.

Software Tectonics FP. The software Tectonics FP 1.7.9 (open version; Ortner et al., 2002; Reiter & Acs, 2000) allows using several inversion methods of fault slip data: the P–T Method (Turner, 1953); the Right Dihedra Method (Angelier & Mechler, 1977); the Direct Inversion Method (Angelier & Goguel, 1979); and the Numerical Dynamic Analysis (Spang, 1972).

The P–T Method (PTM) calculates for each fault plane a compression/maximum shortening axis (P-axis) and an extension/ maximum stretching axis (T-axis). For a set of kinematically related fault planes, the mean vectors of the P- and T-axes represent an approximation to the theoretical strain axes. P- and T-axes define clusters in stereographic projection, based on which kinematically consistent subsets of fault planes can be established from a heterogeneous fault population. According to the Mohr–Coulomb fracture criterion, the PTM adopts a fracture angle (θ) between P and the fault plane. This angle is considered uniform to all fault population, since potentially varying material properties are not taken into account by the method.

The Right Dihedra Method (RDM) uses a grid search technique. The method calculates the compressive dihedral for each given fault plane, by considering all the possible locations of the compression axis on the stereographic projection grid. The eigenvectors of the superposed compressive dihedra will then identify the locus of the stress ellipsoid axes. The RDM calculates the orientations of the three principal stress axes, but not the φ ratio, which is one of the four critical variables of the reduced stress tensor. As this method usually represents the best paleostress tensor, the φ ratio value and the forehead derived stress axes are calculated in a complementary way with other methods.

The classical Direct Inversion Method (DIM) calculates the reduced stress tensor in a single step from the whole data-set by applying a least-square minimization of the angles (misfit angles) between the theoretical and observed slip directions of each fault. The DIM

provides solutions in terms of paleostress tensors, notably the directions of principal paleostress axes ($\sigma1 > \sigma2 > \sigma3$) and the stress ratio (R).

The Numerical Dynamic Analysis (NDA) calculates a strain tensor for each fault-striae set, assuming a fixed angle between the maximum principal strain axis and fault plane. The sum of the resulting strain tensors for every plane, divided by the number of sets, yields the bulk strain tensor. The orientations and relative values of the principal strain axes are obtained from the eigenvalues and eigenvectors of the bulk strain tensor. Therefore, the NDA calculates a reduced strain tensor, composed of the directions of the three principal reciprocal strains ($\lambda1 > \lambda2 > \lambda3$) and the strain ratio (E). The angle θ between λ1 and the maximum resolved shear strain, which is believed to be parallel to the mineral lineation on the shear fault, was calculated by iteration using a best fitting approach. However, it is necessary to verify that any selected θ value does not condition the results of the stress inversion. The values of the angle θ obtained experimentally range 17° and 40° (Jaeger & Cook, 1979).

Procedure of analysis. The first step in the analysis was to check the consistency of the fault-slip data and correct it so that each striation lay within the associated fault plane. Measurements with very large deviations were not included in the calculations

The second step in the analysis consisted of splitting of inhomogeneous fault-slip data sets into kinematically homogeneous subsets basing on mechanical consistency. The definition of subsets was made through field observations, such as the existence of more than one set of striations on the same fault plane, or with the help of graphical procedures, such as tangent-lineation plotting method or P- and T-axes clusters in stereographic projection. Separation of homogeneous subsets from heterogeneous fault-slip data was also performed numerically, by applying an inverse method and obtaining more than one paleostress tensor to groups of faults that integrate data from sites spatially close.

The third step in the analysis was to run the Tectonics FP routine to the defined homogeneous subsets of single outcrops and obtain four solutions, one for each inversion technique considered (PTM, RDM, DIM and NDA). These calculations eliminated fault-slip data that are incompatible with any stress tensor. Statistically stable stress or strain tensors were obtained from 10 to 20 fault-slip data measured in each structural site.

The choice of the best fitting method for a given fault population relied on: (1) the negative expected value (nev) which is the number of fault planes showing opposite senses of slip when the measured values are compared with those theoretically determined; (2) the best fit of principal axes orientations with respect to fault orientation; (3) the accuracy of the slip sense (confidence level assigned during field measurements); and 4) the value of the fluctuation parameter (F). F is calculated as the arithmetic mean of the angles between the theoretical slip directions (according to the "Wallace-Bott hypothesis"; Bott, 1959) and the measured ones. A deviation >20° points to a heterogeneous data set (Ortner et al., 2002). Hence, we will regard a fault-slip datum with the misfit <20° as being compatible with the state of stress evaluated.

Supporting Information S2

U-Th geochronological results of coral samples

Sample	^{238}U (ppm)	^{238}U 2σ error	^{230}Th/^{238}U	^{230}Th/^{238}U 2s error	^{234}U/^{238}U	^{234}U/^{238}U 2s error	δ^{234}U	δ^{234}U (initial)	^{230}Th/^{232}Th	^{230}Th/^{232}Th 2s error	^{234}U/^{238}U (initial)	^{234}U/^{238}U (error)	Age (ka)	Age detr. corr. (ka)	Age d.c. 2σ > error	Age d.c. 2σ < error	^{230}Th (ppm)	^{230}Th sample (ppm)
20JE04A	3,352	0,000	0,709	0,001	1,1234	0,0008	123,41	166,52	732,3	0,90	1,167	0,006	106,20	106,00	0,54	-0,53	3,89E-05	9,92E-03
20JE04D	5,506	0,001	1,179	0,002	1,2738	0,0007	273,77	521,23	2811,0	1,65	1,521	0,013	228,04	227,85	1,88	-1,85	1,06E-04	7,05E-03
21JE39	2,832	0,001	1,031	0,004	1,0795	0,0010	79,53	183,96	42800,1	140,29	1,184	0,030	296,76	296,73	7,46	-6,98	4,78E-05	2,09E-04
21JE64	2,653	0,000	0,792	0,001	1,1224	0,0004	122,35	176,12	5449,9	2,18	1,176	0,004	128,93	128,89	0,40	-0,40	3,44E-05	1,18E-03
21JE124	2,711	0,001	0,008	0,000	1,1570	0,0005	157,04	157,36	189,7	1,93	1,157	0,016	0,73	0,73	0,01	-0,01	3,42E-07	3,36E-04
21JE126A	2,345	0,000	1,072	0,002	1,0944	0,0007	94,37	241,09	35721,6	25,68	1,241	0,017	331,96	331,92	4,51	-4,33	4,11E-05	2,15E-04
21JE126B	2,709	0,001	1,121	0,002	1,0968	0,0007	96,77	372,54	9159,3	3,29	1,373	0,068	477,60	476,99	23,63	-19,64	1,12E+00	2,43E-03
21JE126C	1,254	0,000	0,824	0,001	1,2117	0,0008	211,71	295,89	10615,2	13,28	1,296	0,006	118,48	118,47	0,52	-0,51	1,69E-05	2,97E-04
21JE129	5,573	0,002	0,833	0,003	1,1924	0,0007	192,39	273,64	9942,4	17,22	1,274	0,009	124,67	124,65	0,85	-0,84	7,59E-05	1,43E-03
22JE26B	2,850	0,000	0,770	0,002	1,1193	0,0009	119,32	169,03	4863,5	4,05	1,169	0,007	123,27	123,23	0,70	-0,69	3,59E-05	1,38E-03

^{238}U concentration in coral sample (ppm). 2σ (95% confidence limit) measurement error on ^{238}U concentration in coral sample (ppm)

^{230}Th/^{238}U is measured activity ratio. ^{230}Th/^{238}U 2σ error is measurement error on activity ratio.

^{234}U/^{238}U is measured activity ratio. ^{234}U/^{238}U 2σ error is measurement error on activity ratio.

d^{234}U is measured, present day d^{234}. d^{234}U (initial) is calculated initial d^{234}.

^{230}Th/^{232}Th is measured activity ratio. ^{230}Th/^{232}Th 2σ error is measurement error on activity ratio.

^{234}U/^{238}U (initial) is calculated ratio on the basis of the present-day measured ^{234}U/^{238}U and the calculated age.

^{234}U/^{238}U (error) is uncertainty on calculated initial ^{234}U/^{238}U taking into account uncertainty on measured ratio and calculated age.

Age (ka) is calculated U-Th age in ka

Age 2σ error is age uncertainty in ka on (>) high and (<) low age sides (age errors are not symmetrical because ratios change in a non-linear way with age).

Age detr. Corr. (ka) is calculated U-Th age in ka, corrected for detrital contamination (assuming ^{230}Th/^{232}Th = 0.8 ± 0.4).

Supporting Information S5

Stress tensors obtained by methods of inversion of fault-slip data

Data		RDM										DIM						NDA						
		σ_1			σ_2			σ_3				σ_1		σ_2		σ_3		λ_1		λ_2		λ_3		
Site	Num.	Eigen	Dir	Inm	Eigen	Dir	Inm	Eigen	Dir	Inm	R	Dir	Inm	Dir	Inm	Dir	Inm	Dir	Inm	Dir	Inm	Dir	Inm	E
20JE14	10	0,49	227	0	0,33	137	77	0,18	317	13	0,48	78	4	252	86	348	0	40	1	136	75	310	15	0,58
21JE70A	16	0,4	22	7	0,32	313	59	0,28	118	30	0,33	190	13	295	47	89	40	44	12	292	61	140	26	0,34
21JE70B	8	0,48	130	64	0,35	289	24	0,17	23	8	0,58	41	57	283	17	184	28	98	71	289	19	198	3	0,49
21JE72	14	0,41	237	1	0,32	147	6	0,27	337	83	0,36	62	44	269	43	166	14	79	23	341	17	219	61	0,37
21JE73	10	0,38	197	8	0,37	292	29	0,25	93	60	0,92	224	26	315	2	50	64	267	18	7	28	149	56	0,68
21JE78A	8	0,484	280	7	0,34	189	6	0,18	60	81	0,53	183	1	274	25	90	65	281	2	191	5	35	85	0,51
21JE78B	14	0,5	324	81	0,32	194	5	0,18	103	7	0,44	327	49	199	28	94	27	54	79	195	9	286	7	0,43
21JE79A	12	0,39	202	4	0,37	292	3	0,24	61	85	0,87	249	10	151	36	352	52	223	18	129	12	8	68	0,66
21JE79B	10	0,5	70	77	0,3	173	3	0,2	264	13	0,33	267	67	100	22	8	5	135	87	355	3	265	2	0,38
21JE80A	8	0,5	53	69	0,32	277	16	0,18	183	14	0,44	118	64	309	26	217	5	66	81	272	8	181	4	0,39
21JE80B	12	0,4	213	24	0,36	304	2	0,25	39	66	0,73	287	67	117	23	26	4	210	30	117	5	19	59	0,46
21JE80C	13	0,46	53	5	0,32	157	69	0,22	321	20	0,42	273	21	14	26	149	56	210	30	117	5	19	59	0,46
21JE93A	10	0,45	207	13	0,3	350	74	0,26	115	9	0,21	197	38	33	51	293	8	213	28	341	50	108	27	0,41
21JE94A	8	0,38	70	21	0,33	161	2	0,29	255	69	0,44	105	22	227	52	2	29	50	35	311	13	204	52	0,47
21JE96A	10	0,44	356	12	0,34	86	1	0,22	180	78	0,55	165	1	256	17	71	73	351	13	83	9	206	74	0,37
21JE96B	8	0,47	236	76	0,3	46	13	0,23	136	2	0,29	18	66	173	22	266	9	330	86	239	1	149	4	0,28
21JE97	11	0,41	221	3	0,34	128	46	0,26	314	44	0,53	182	16	7	74	272	1	202	1	111	24	294	56	0,64
21JE98	13	0,43	55	9	0,35	201	79	0,23	324	6	0,60	93	11	303	78	184	6	221	1	125	77	311	13	0,65
21JE99B	8	0,46	326	73	0,35	213	7	0,19	121	16	0,59	176	62	29	24	293	14	332	83	221	3	131	7	0,59
21JE100	10	0,44	226	3	0,32	321	64	0,24	135	26	0,40	261	4	358	58	169	31	208	11	28	79	298	0	0,36
21JE102A	13	0,46	243	1	0,29	153	19	0,25	336	71	0,19	180	2	270	20	84	70	47	5	144	52	312	37	0,37
21JE103	9	0,45	349	45	0,35	162	45	0,2	256	4	0,60	33	56	164	24	265	22	9	63	149	21	246	16	0,56
21JE108B	8	0,52	269	71	0,34	161	6	0,14	69	18	0,53	61	62	298	16	202	22	311	84	162	5	72	3	0,50
21JE112A	9	0,49	222	21	0,33	131	4	0,18	32	69	0,48	11	7	102	5	226	81	210	12	302	9	68	74	0,40
21JE112B	10	0,45	55	62	0,33	204	24	0,22	300	13	0,48	337	64	205	18	109	18	39	71	207	18	298	3	0,51
21JE113	16	0,45	65	85	0,35	251	5	0,2	161	1	0,60	98	19	302	70	191	8	132	78	256	7	348	10	0,59
21JE120A	10	0,49	26	2	0,35	116	1	0,16	226	88	0,58	205	12	295	1	28	78	206	13	116	1	22	77	0,50
21JE120B	10	0,51	147	80	0,33	291	8	0,16	21	6	0,49	25	52	285	8	189	37	155	77	288	9	19	9	0,48
21JE121	10	0,47	124	67	0,32	331	20	0,22	238	9	0,40	135	60	319	30	228	2	169	66	338	23	70	4	0,28
21JE123A	10	0,5	204	1	0,36	294	3	0,14	99	87	0,61	4	7	113	68	271	21	207	7	117	0	24	83	0,64
21JE125A	10	0,49	200	4	0,34	82	83	0,17	291	6	0,53	36	20	179	65	301	14	32	1	128	82	302	8	0,54
21JE125B	10	0,51	279	86	0,31	110	4	0,19	20	1	0,38	2	65	174	25	266	3	59	88	284	1	194	1	0,33
21JE127	10	0,48	20	4	0,31	137	80	0,21	290	9	0,37	34	4	304	2	183	85	28	4	151	82	298	6	0,50

21JE130A	10	0,41	78	28	0,34	183	27	0,25	310	49	0,56	47	6	141	34	309	56	28	4	151	82	298	6	0,50
21JE130B	10	0,42	336	58	0,33	75	5	0,25	168	32	0,47	109	86	265	4	355	2	346	78	254	0	164	12	0,36
21JE137	18	0,45	154	76	0,33	278	8	0,22	10	11	0,48	126	87	340	3	250	2	155	83	279	4	9	6	0,42
22JE12	13	0,4	222	0	0,33	132	45	0,27	312	45	0,46	-	-	-	-	-	-	29	8	120	2	225	81	-
22JE13A	15	0,51	51	2	0,35	321	3	0,14	185	86	0,57	90	12	359	4	248	78	58	12	327	6	212	76	0,51
22JE13B	10	0,48	38	2	0,31	146	83	0,21	308	7	0,37	264	10	167	33	9	55	37	4	148	78	306	11	0,55
22JE15	17	0,5	169	82	0,34	278	3	0,16	8	8	0,53	353	72	155	17	247	5	23	85	276	1	185	5	0,50
22JE17	10	0,51	195	10	0,33	91	54	0,16	292	35	0,49	196	2	286	2	66	87	196	2	286	2	66	87	0,54
22JE26	10	0,45	46	7	0,31	149	60	0,24	312	29	0,33	26	11	291	23	140	64	37	10	148	64	303	23	0,58

Num; fault-slip data number. RDM; Right-Dihedra Method. DIM; Direct Inmersion Method. NDA; Numerical Dynamical Analysis.

σ_1. σ_2 and σ_3; principal stress axes ($\sigma_1>\sigma_2>\sigma_3$). Eigen; eigenvalue. Dir; azimuth. Inm; inmersion angle. R; stress ratio ($R=(\sigma_2-\sigma_3)/(\sigma_1-\sigma_3)$; $0\leq R\leq 1$). E; strain ratio

Supporting Information S6

Maximum horizontal stresses and tectonic regimes obtained by inversion methods

Site	σ_H (máx)		Stress regime			
	Dir	Inm	R	Fault type	Method	Oher consistent methods
21JE72	237	1	0,36	reverse D1	RDM	*DIM, NDA*
21JE73	197	8	0,92	reverse D1	RDM	*DIM, NDA*
21JE78A	280	7	0,53	reverse D1	RDM	*DIM, NDA*
21JE79A	202	4	0,87	reverse D1	RDM	*DIM, NDA*
21JE80B	213	24	0,73	reverse D1	RDM	*DIM, NDA*
21JE94A	70	21	0,44	reverse D1	RDM	*DIM, NDA*
21JE96A	356	12	0,55	reverse D1	RDM	*DIM, NDA*
21JE102A	243	1	0,19	reverse D1	RDM	*DIM, NDA*
21JE112A	222	21	0,48	reverse D1	RDM	*DIM, NDA*
21JE120A	26	2	0,58	reverse D1	RDM	*DIM, NDA*
21JE123A	204	1	0,61	reverse D1	RDM	*DIM, NDA*
21JE130	47	6	0,27	reverse D1	DIM	-
22JE12	222	0	0,46	reverse D1	RDM	*DIM, NDA*
22JE13A	51	2	0,57	reverse D1	RDM	*DIM, NDA*
20JE14	227	0	0,48	strike-slip D2	RDM	*DIM, NDA*
21JE70A	22	7	0,33	strike-slip D2	RDM	*DIM, NDA*
21JE80C	53	5	0,42	strike-slip D2	RDM	*DIM, NDA*
21JE93A	207	13	0,21	strike-slip D2	RDM	*DIM, NDA*
21JE97	221	3	0,53	strike-slip D2	RDM	*DIM, NDA*
21JE98	55	9	0,60	strike-slip D2	RDM	*DIM, NDA*
21JE100	226	3	0,40	strike-slip D2	RDM	*DIM, NDA*
21JE125A	200	4	0,53	strike-slip D2	RDM	*DIM, NDA*
21JE127	20	4	0,37	strike-slip D2	RDM	*DIM, NDA*
22JE13B	38	2	0,37	strike-slip D2	RDM	*DIM, NDA*
22JE17	195	10	0,49	strike-slip D2	RDM	*DIM, NDA*
22JE26	46	7	0,33	strike-slip D2	RDM	-
21JE70B	289	24	0,58	extensional D3	RDM	*DIM, NDA*
21JE78B	194	5	0,44	extensional D3	RDM	*DIM, NDA*
21JE79B	173	3	0,33	extensional D3	RDM	*DIM, NDA*
21JE80A	277	16	0,44	extensional D3	RDM	*DIM, NDA*
21JE96B	46	13	0,29	extensional D3	RDM	*DIM, NDA*
21JE99B	213	7	0,59	extensional D3	RDM	*DIM, NDA*
21JE103	162	45	0,60	extensional D3	RDM	*DIM, NDA*
21JE108B	161	6	0,53	extensional D3	RDM	*DIM, NDA*
21JE112B	204	24	0,48	extensional D3	RDM	*DIM, NDA*
21JE113	251	5	0,60	extensional D3	RDM	*DIM, NDA*
21JE120B	291	8	0,49	extensional D3	RDM	*DIM, NDA*
21JE121	331	20	0,40	extensional D3	RDM	*DIM, NDA*
21JE125B	110	4	0,38	extensional D3	RDM	*DIM, NDA*
21JE130B	75	5	0,47	extensional D3	RDM	*DIM, NDA*
21JE137	278	8	0,48	extensional D3	RDM	*DIM, NDA*
22JE15	278	3	0,53	extensional D3	RDM	*DIM, NDA*

σ_H (max); máximum horizontal stress. Dir; azimuth. Inm; inmersion angle.

R; stress ratio ($R=(\sigma_2-\sigma_3)/(\sigma_1-\sigma_3)$; $0 \leq R \leq 1$).

RDM; Right-Dihedra Method, DIM; Direct Inmersion Method, NDA; Numerical Dynamical Analysis.

Supporting Information S4

Sites used to obtain stress tensors from the analysis of fault-slip data sets

Site	Longitude (X)	Latitude (Y)	Geological Domain	Quadrangle (E. 1:50k)	Stratigraphic Unit	Unit Age	Main Lithology
20JE14	-70,51720	18,56506	San Jose de Ocoa basin	San José de Ocoa	Numero Fm, Fluvial Terrace	Late Eocene, Quaternary	Dark mudstone, gravel and clay
21JE70	-70,45311	18,67916	Cordillera Central	Arroyo Caño	Arroyo Caña Batholith	Late Cretaceous	Tonalite
21JE72	-70,47095	18,65749	Cordillera Central	Sabana Larga	Arroyo Caña Batholith	Late Cretaceous	Gabbro
21JE73	-70,45346	18,62003	Cordillera Central	Sabana Larga	Arroyo Caña Batholith	Late Cretaceous	Leucotonalite
21JE78	-70,68596	18,94094	Cordillera Central	Constanza	Tireo Group, Constanza Fm	Late Cretaceous	Green tuff
21JE79	-70,62475	18,91709	Cordillera Central	Constanza	Tireo Group, Constanza Fm	Late Cretaceous	Green tuff and dolerite
21JE80	-70,63772	18,92659	Cordillera Central	Constanza	Tireo Group, Constanza Fm	Late Cretaceous	Green tuff
21JE93	-70,59447	18,69213	'eralta fold-and-thrust be	Sabana Quéliz	Ocoa Fm	Late Eocene	Conglomerate
21JE94	-70,58965	18,68086	'eralta fold-and-thrust be	Sabana Quéliz	Numero Fm	Middle to Late Eocene	Dark mudstone and sandstone
21JE96	-70,54467	18,65448	'eralta fold-and-thrust be	San José de Ocoa	Ocoa Fm	Late Eocene	Conglomerate
21JE97	-70,53869	18,65274	'eralta fold-and-thrust be	San José de Ocoa	Ocoa Fm	Late Eocene	Conglomerate
21JE98	-70,52779	18,63098	'eralta fold-and-thrust be	San José de Ocoa	Ocoa Fm	Late Eocene	Dark mudstone and sandstone
21JE99	-70,51323	18,64305	'eralta fold-and-thrust be	San José de Ocoa	Tireo Group	Maastrichtian	Limestone
21JE100	-70,50453	18,58901	'eralta fold-and-thrust be	San José de Ocoa	Ocoa Fm	Late Eocene	Dark mudstone and sandstone
21JE102	-70,48251	18,56104	'eralta fold-and-thrust be	Sabana Larga	Tireo Group, Constanza Fm	Late Cretaceous	Green tuff and sandstone
21JE103	-70,47375	18,57525	'eralta fold-and-thrust be	Sabana Larga	Tireo Group, Constanza Fm	Late Cretaceous	Green tuff and sandstone
21JE108	-70,51455	18,49968	'eralta fold-and-thrust be	Azua	Jura Fm, Ocoa Fm	Middle to late Eocene	Red limestone and mundstone
21JE112	-70,71758	18,42512	Azua basin	Azua	Sobrerito Fm	Early Miocene	Limestone
21JE113	-70,70741	18,39128	Azua basin	Azua	Sobrerito Fm	Early Miocene	Limestone
21JE120	-70,73770	18,35106	Azua basin	Azua	Sobrerito Fm	Early Miocene	Limestone
21JE121	-70,72878	18,35725	Azua basin	Azua	Sobrerito Fm	Early Miocene	Limestone
21JE123	-70,56557	18,40412	'eralta fold-and-thrust be	Azua	Arroyo Seco	Late Plioc.-Early Pleistoc.	Conglomerate and clay
21JE125	-70,67905	18,43106	Azua basin	Azua	Sobrerito Fm	Early Miocene	Limestone
21JE126	-70,87761	18,29942	Sierra Martin Garcia	Barrero	Coral reef terrace	Late Pleistocene	Limestone
21JE127	-70,88598	18,28986	Sierra Martin Garcia	Barrero	Upper Alluvial Fan	Late Pleistocene	gravel and silt/clay
21JE129	-71,06235	18,32466	Sierra Martin Garcia	Barahona	Coral reef terrace	Late Pleistocene	Limestone
21JE130	-71,13364	18,34960	Sierra Martin Garcia	Vicente Noble	Angostura Fm	Early Pliocene	Gypsum, mudstone and sandstone
21JE137	-71,05840	18,15422	Sierra Bahoruco	La Ciénaga	Coral reef terrace, alluvial fan	Late Pleistocene	Limestone, gravel and mudstone
22JE12	-70,94551	18,60346	'eralta fold-and-thrust be	Vayas de Viajama	Trinchera Fm	Middle to late Miocene	Sandstone, gravel and silt/clay
22JE13	-70,86600	18,59378	'eralta fold-and-thrust be	Vayas de Viajama	Ventura Fm, Jura Fm	Lower to middle Eocene	Dark mudstone, sandstone and limestone
22JE15	-70,88191	18,29371	Sierra Martin Garcia	Barrero	Upper Alluvial Fan	Late Pleistocene	gravel and silt/clay
22JE17	-70,88424	18,29217	Sierra Martin Garcia	Barrero	Upper Alluvial Fan	Late Pleistocene	gravel and silt/clay
22JE26	-71,05918	18,15463	Sierra Bahoruco	La Ciénaga	Coral reef terrace, alluvial fan	Late Pleistocene	Limestone, gravel and mudstone